Link between structural and electronic properties of moirés of graphene studied by scanning tunneling microscopy

Loïc Huder

Communauté
UNIVERSITÉ Grenoble Alpes

THÈSE

Pour obtenir le grade de

DOCTEUR DE LA COMMUNAUTÉ UNIVERSITÉ GRENOBLE ALPES

Spécialité : **Physique de la matière condensée et du rayonnement**

Arrêté ministériel : 25 mai 2016

Présentée par

Loïc HUDER

Thèse dirigée par **Louis JANSEN**
et codirigée par **Vincent RENARD**

préparée au sein du **LaTEQS, du service PHELIQS, de l'Institut NAnosciences et Cryogénie, du CEA Grenoble**
et de **l'École Doctorale de Physique de Grenoble**

Lien entre structure et propriétés électroniques des moirés de graphène étudié par microscopie à effet tunnel

Link between structural and electronic properties of moirés of graphene studied by scanning tunneling microscopy

Thèse soutenue publiquement le **29 novembre 2017**,
devant le jury composé de :

Laurence MAGAUD
Directrice de Recherches à l'Institut Néel, CNRS, Présidente
Markus MORGENSTERN
Professeur à RWTH Aachen University, Rapporteur
Guillaume SCHULL
Chargé de Recherches à l'Institut de Physique et de Chimie des Matériaux de Strasbourg, Rapporteur
Mikael SYVÄJÄRVI
Senior scientist à Linköping University, Examinateur

À Caroline

REMERCIEMENTS

La recherche scientifique est un travail de longue haleine et de ce fait, toute contribution, aussi petite soit-elle, a de la valeur et est la bienvenue. Dans cette partie, j'aimerais remercier toutes les personnes qui ont apporté leur pierre au travail que je présente dans ce manuscrit.

J'aimerais d'abord remercier les rapporteurs Markus Morgenstern et Guillaume Schull pour avoir eu un regard intéressé et critique sur mon manuscrit ainsi que les autres membres du jury : Laurence Magaud, Mikaël Syväjarvi, Guy Trambly de Laissardière. Leur intérêt pour mon travail, leurs questions ainsi que les discussions qui ont suivi ont contribué à faire de ma soutenance un moment d'échange scientifique que j'ai grandement apprécié.

J'aimerais également remercier en premier lieu François Lefloch qui fut le premier à me rencontrer pour me faire visiter le LaTEQS, me donnant envie d'y faire ma thèse. Je remercie également Marc Sanquer et Jean-Pascal Brison, directeurs du LaTEQS et de l'ex-SPSMS, ces deux structures qui m'ont accueilli et qui furent un cadre dynamique et convivial où j'ai eu un grand plaisir à effectuer mes travaux de thèse.

J'ai eu la chance de bénéficier d'une excellente équipe d'encadrement que je souhaite également remercier. Tout d'abord, Louis, merci d'avoir accepté de diriger ma thèse, de m'avoir permis de m'intégrer à la vie du laboratoire dès mon stage et d'avoir été disponible pour des discussions scientifiques et techniques.

Ensuite je remercie grandement Vincent qui fut un encadrant exemplaire de ma thèse. Je ne pense pas pouvoir exprimer toute l'aide et tout le soutien que tu as pu m'apporter pendant ces trois ans. J'ai toujours admiré ta capacité à garder ta bonne humeur et ton calme olympien en toute circonstance, te permettant de garder un point de vue clair et éclairé. Mes meilleurs souvenirs de thèse comprennent nos nombreuses discussions informelles qui ont été un

réel moteur pour moi. Alors même que tu jonglais avec tes responsabilités d'enseignant, tu as été un référent quotidien qui a su se rendre disponible pour moi pour discuter sur n'importe quel sujet, qu'il soit scientifique ou personnel.

Je suis immensément reconnissant envers Claude qui a pris de son temps et de sa personne pour venir me voir et me remettre sur les rails quand ça n'allait pas. Tu as agi comme un troisième encadrant, participant à mes points de thèse, à mes répétitions d'oraux, à la correction des manuscrits malgré ton agenda chargé. Tu m'as fait partager ton goût de la microscopie à effet tunnel et je ne peux que louer ton dévouement. Encore une fois, les mots me manquent pour exprimer toute ma gratitude. Cette thèse n'aurait pas été la même sans toi.

J'aimerais maintenant remercier mes collaborateurs proches avec qui j'ai eu grand plaisir à travailler. Je pense notamment à Toai, avec qui j'ai pu partager sur la microscopie à effet tunnel, la croissance de graphène et ses résultats et qui fut le pionnier de mon travail de thèse.

Une grande partie de ce travail a aussi capitalisé sur la thèse d'Alexandre A. à qui j'adresse ma reconnaissance. J'ai eu beaucoup de chance que tu fasses ta thèse en même temps que moi car tu t'es rendu toujours disponible pour que nous parlions de nos travaux mais aussi de la thèse en général, ce qui m'a bien aidé. J'ai également toujours admiré ta connaissance de la physique ainsi que l'efficacité de tes présentations qui témoignait du soin que tu leur portais. Tu as donc non seulement influencé le coeur de mon travail mais aussi la façon dont je le présentais pour tenter de reproduire cette efficacité. Pour tout cela, je te remercie !

Ce travail n'aurait pas non plus été possible sans Guy Trambly de Laissardière, notre théoricien préféré. Merci à toi Guy, de t'être rendu disponible pour nous expliquer tes modèles et pour avoir lancer sans rechigner tous ces calculs sur ces innombrables structures que l'on t'envoyait. Ta collaboration fut d'une immense aide et très agréable !

I also would like to thank Felipe a great deal. Our discussions over coffee were always fulfilling and I learned a lot from working with you, notably in the clean room, both from the scientific than from the personal point of view.

J'aimerais aussi remercier tous les thésards et post-docs que j'ai pu rencontrer au sein du laboratoire et avec qui j'ai eu grand plaisir à discuter et partager lors de ces trois années de thèse : Alessandro, Dharmaj, Gaël, Paul, Patrick, Juan Carlos, Florian V. et bien d'autres. Je remercie particulièrement Andrea, qui m'a initié au Python et avec qui j'ai pu faire de nombreuses sorties en montagne avant son départ vers d'autres horizons, ainsi que Romain M., le plus permanent des post-docs (ou l'inverse) qui non seulement m'a fait découvrir le vélo de route dans ces magnifiques montagnes autour de

Grenoble (le fameux tour du Néron !) mais qui m'a toujours ouvert sa porte pour parler de science, de la suite après la thèse ou de la recherche en général avec sa bonne humeur communicative. Je pense également aux piliers de la pause café : Florian B., le roi de l'informatique à qui j'ai de nombreuses fois fait appel, Romain A., mon condisciple lorrain avec ses idées... originales et Anthony, le breton boute-en-train. J'ai beaucoup apprécié passer du temps avec vous et échanger sur de nombreux sujets que ce soit la supraconductivité non conventielle ou bien le nombre de saisons de Power Rangers ! Je n'oublie pas non plus Thomas, mon apprenti au labo mais mon maître en cyclisme (le Chris Froome du labo), avec qui ce fut un plaisir de travailler et d'aller rouler !

Je remercie aussi tout le personnel de la PTA pour leur soutien et leur aide durant mes travaux en salle blanche. Mention particulière à Frédéric G. qui m'a immensément aidé pour les dépôts de métaux et toujours avec le sourire ! J'en profite aussi pour remercier les permanents du labo: Xavier, qui avait toujours une petite blague à sortir de son sac, Max, François, Christophe, Marc, Silvano mais aussi IMAPEC : Daniel, Alexandre, Georg et Jean-Pascal. J'en profite également pour remercier l'équipe du D5 (Gérard, le bellilois Christophe et Karine) ainsi que Florence du SCIB pour notre collaboration. J'ai aussi eu la chance de pouvoir m'appuyer sur l'expertise de nombreuses personnes dans leur domaine respectif : Marielle pour l'administratif, Michel pour la mécanique, Jean-Michel et Iulian pour la cryogénie, Pierre pour l'électronique (et la montagne !) et enfin Frédéric P. pour l'informatique.

Enfin, je remercie mes parents qui a toujours été présents pour moi et qui m'ont toujours supporté dans mes choix, quels qu'ils soient. Je les remercie d'être venus à la soutenance, de même que mes amis Alexandre et Vincent, Lydie et ma soeur Chloé, qui ont tous fait le déplacement pour m'écouter discourir sur un sujet qui leur paraissait plutôt obscur !

Le meilleur pour la fin, j'aimerais remercier grandement Caroline qui partage ma vie depuis maintenant 10 ans. Une thèse, ce sont des hauts mais aussi des bas, et tu m'as accompagné dans tous ces moments. Tous ces instants passés ensemble furent irremplacables et m'ont permis de garder la motivation tout au long de la thèse. J'ai toujours pu compter sur ton soutien et je suis heureux de pouvoir continuer à le faire.

RÉSUMÉ EN FRANÇAIS

Les dernières années ont vu l'avènement des couches cristallines bidimensionnelles, appelées matériaux 2D. L'exemple le plus connu est le graphène, d'autres étant le niture de bore hexagonal isolant et le diséléniure de niobium supraconducteur. Ces matériaux 2D peuvent être empilés de manière contrôlée sous la forme d'hétérostructures de van der Waals pour obtenir les propriétés électroniques desirées. Une des plus simples hétérostructures de van der Waals est l'empilement de deux couches de graphène tournées. Cet empilement donne naissance à un moiré qui peut être vu comme un potentiel superpériodique dépendant de l'angle entre les deux couches. Les propriétés électroniques des couches tournées de graphène sont intimement liées à ce moiré.

Le sujet de cette thèse est l'étude expérimentale du lien entre la structure et les propriétés électroniques des couches tournées de graphène par microscopie et spectroscopie à effet tunnel à basse température.

Alors que l'effet de l'angle entre les couches sur les propriétés électroniques a déjà été étudié en détail, la modification de celles-ci par une déformation des couches n'a été envisagée que récemment. La première partie de ce travail expérimental étudie la modification par la déformation des propriétés électroniques de couches de graphène tournées d'un angle de 1.26°, crûes sur carbure de silicium. La déformation en question est différente dans les deux couches et son effet apparait clairement dans la densité locale d'états électroniques du moiré mesurée par spectroscopie tunnel. La différence de déformations entre les couches (déformation relative) modifie fortement la structure de bandes, transformant les cônes de Dirac en bandes plates. Ce changement radical est induit par de faibles valeurs de déformations relatives mises en évidence par l'analyse des images de microscopie tunnel. Les résultats, confortés par des calculs de liaisons fortes, montrent notamment que

la déformation d'une couche par rapport à l'autre est beaucoup plus efficace pour modifier les propriétés électroniques qu'une déformation appliquée aux deux couches.

Alors que cette déformation relative était spontanément présente, la deuxième partie de cette thèse s'intéresse à l'effet d'une déformation appliquée directement aux couches de graphène. Cette déformation vient d'une interaction induite par l'approche de la pointe STM vers la surface de graphène. La modification active de la densité d'états est gouvernée par le choix des conditions tunnels qui fixent la distance entre la pointe et la couche de graphène. Ces effets dépendent de la position de la pointe dans le moiré avec l'apparition d'instabilités périodiques lorsque la distance entre la pointe et l'échantillon est très faible.

La troisième partie de cette thèse concerne l'étude d'un autre type de modification des propriétés électroniques consistant en l'induction de supraconductivité dans les couches de graphène. Cette modification est effectuée par une croissance du graphène en une seule étape sur du carbure de tantalum supraconducteur. Les résulats montrent la formation d'une couche de carbure de tantale de grande qualité sur laquelle les couches de graphène forment des moirés. La mesure à basse température de la densité d'états de ces moirés met en évidence la présence d'un effet de proximité supraconducteur induit par le carbure de tantale à travers les couches de graphène.

SUMMARY

Recent years have seen the emergence of two-dimensional crystalline layers, called 2D materials. Examples include the well-known graphene, insulating hexagonal boron nitride and superconducting niobium diselenide. The stacking of these 2D materials can be controlled to achieve desirable electronic properties under the form of van der Waals heterostructures. One of the simplest van der Waals heterostructures is the misaligned stacking of two graphene layers. Twisted graphene layers show a moiré pattern which can be viewed as a superperiodic potential that depends on the twist angle. The electronic properties of the twisted graphene layers are strongly linked to this moiré pattern.

The subject of the present thesis is the experimental study of the link between the structural and the electronic properties of twisted graphene layers by means of low-temperature Scanning Tunneling Microscopy and Spectroscopy (STM/STS).

While the effect of the twist angle has already been studied in great details, the modulation of the electronic properties by the deformation of the layers has been explored only recently. In the first part of this experimental work, a strain-driven modification of the electronic properties is probed in graphene layers with a twist angle of 1.26°, grown on silicon carbide. The determined strain is found to be different in the two layers leading to a clear signature in the local electronic density of states of the moiré probed by Scanning Tunneling Spectroscopy. This difference of strain between the layers (relative strain) modifies strongly the electronic band structure, transforming the Dirac cones in flat bands. This radical change is triggered by low relative strain magnitudes evidenced by the analysis of the Scanning Tunneling Microscopy images. The results, backed by tight-binding calculations, show notably that straining one layer with respect to the other is much more

effective in changing the electronic properties compared to applying strain in both layers.

While this relative strain is natively present, the second part of the work explores the effect of an applied strain in the layers. This is realized by approaching the STM tip to the graphene surface to trigger an interaction between the two. The resulting active modification of the density of states is governed by the choice of the tunneling conditions that set the distance between the tip and the graphene layer. These effects also depend on the position on the moiré, leading to periodic instabilities at very low tip-sample distances.

In the third part of the work, another type of modification of the electronic properties is studied when superconductivity was induced in the graphene layers. This is done by growing graphene on superconducting tantalum carbide in a single-step annealing. The results show the formation of a high-quality tantalum carbide layer on which graphene layers form moiré patterns. The low-temperature density of states of these moirés show evidence of a superconducting proximity effect coming from the tantalum carbide across the graphene layers.

SYNOPSIS

Lien entre structure et propriétés électroniques des moirés de graphène étudié par microscopie à effet tunnel

La superposition de deux différents motifs périodiques forme un moiré. En physique de la matière condensée, le moiré apparaît dans les images par microscopie à effet tunnel de réseaux atomiques superposés présentant un angle entre eux et/ou une différence de paramètre de maille. Le moiré dépend fortement de ces differences structurelles et agit comme un potentiel superpériodique sur les électrons. Les systèmes de moirés présentent donc un lien fort entre leur structure et leurs propriétés électroniques.

Dans cette thèse, j'ai étudié ce lien par microscopie à effet tunnel à basse température dans les couches tournées de graphène, c'est-à-dire l'empilement de deux couches de graphène présentant un angle entre les deux. L'analyse détaillée des images STM montre que le moiré résulte non seulement d'un angle ($\theta = 1.26°$) mais aussi d'une déformation entre les couches. Cette déformation relative, bien que faible, a un effet distinct sur la densité mesurée d'états électroniques bien reproduit par les calculs de liaisons fortes. Ce lien a été également utilisé pour induire des changements dans la densité locale d'états électroniques du moiré en déformant le graphène avec la pointe STM. Dans un dernier temps, la croissance de graphène sur carbure de tantale a été étudiée révélant la formation de moirés de graphène dans lesquels la supraconductivité fut induite par effet de proximité à travers les couches de graphène.

Link between structural and electronic properties of moirés of graphene studied by scanning tunneling microscopy

The superimposition of two mismatched periodic patterns leads to the apparition of a moiré pattern. In condensed-matter physics, the moiré pattern is known to occur in Scanning Tunneling Microscopy (STM) images of two superimposed atomic layers with a twist angle and/or a lattice parameter difference between the two lattices. The moiré pattern depends highly on these mismatches and in addition acts as a superperiodic potential on the electrons. This leads to a strong link between the structure and the electronic properties of moiré systems.

In this thesis, I studied this link in twisted graphene layers, *i.e.* the misorientated stacking of two graphene layers, using STM at low temperatures. Detailed analyses of STM images show that not only rotation ($\theta = 1.26°$) but also strain between the layers are involved in the formation of the moiré pattern. Even rather small relative strain has a distinct signature on the measured electronic density of states that is well reproduced by theoretical calculations. This link was also exploited by inducing deformations in the graphene layer with the STM tip to trigger changes in the local electronic density of states of the moiré system. Finally, the growth of graphene on high-quality tantalum carbide was studied revealing the formation of moirés of graphene in which superconductivity was induced by proximity effect across the graphene layers.

INTRODUCTION

In 2004 was reported the isolation of graphene, a one-atom-thick layer of carbon [67]. The layered structure of graphite allowed to reduce it to its thinnest form by mechanical exfoliation. This drew a lot of interest from the scientific community as it was the first time that a two-dimensional material was made available by table-top techniques. The particular properties of graphene also made it very interesting for both fundamental studies and applications.

It was then discovered that a whole family of layered materials could be exfoliated like graphite. This led to the isolation of numerous one-atom thick layers such as $MoSe_2$, $NbSe_2$, hexagonal boron nitride or phosphorene, now known as 2D materials [68]. These 2D materials are a rich family in which insulating, semi-conducting, conducting or superconducting 2D compounds can be found. To combine these properties, it was proposed to simply stack these materials, taking advantage of the weak out-of-plane van der Waals bonding to avoid any structural damage [34, 69]. By designing such so-called van der Waals heterostructures, devices with unique physical properties can be built from atomically thin materials.

Notably, one of the simplest van der Waals heterostructures can be realized by the misorientated stacking of two graphene layers. The mismatch between the atomic lattices of the two layers leads to the appearance of a superperiodic feature called a moiré pattern in analogy with optical moiré patterns. This moiré pattern can be viewed as an interference of the atomic periods and acts as an additional periodic potential on the electrons. Due to this, moirés of graphene show a very strong link between structural parameters and the electronic band structure [13, 54, 55, 90, 91]. This system is particularly suitable to Scanning Tunneling Microscopy and Spectroscopy (STM-STS) [15, 44, 50, 101, 105, 106] as it allows both to resolve the struc-

ture of the moiré and to measure locally the electronic density of states.

The effect of strain in twisted graphene layers (and more generally in van der Waals heterostructures) on their electronic properties has very rarely been investigated. This is surprising given the remarkable demonstrated modulation of electronic properties of monolayers by strain [5]. The aim of this thesis is to study the link between applied strain and electronic properties in twisted graphene layers using STM/STS at low temperature.

Chapter 1 begins with the introduction of the properties of pristine graphene. The changes induced by the stacking of two graphene layers is discussed in detail with the introduction of the commensurability formalism of moirés and of the rich physics that depend strongly on the angle between the layers. A discussion on the experimental available techniques to obtain twisted graphene layers concludes the chapter. Chapter 2 is devoted to the experimental methods used to obtain the presented experimental data. It includes a description of the principle of STM/STS and of the low-temperature STM/STS system. It also gives the details of the realization of the samples and of the experimental data analysis. The focus of Chapter 3 is the effect of strain on the density of states in twisted graphene layers. We first review the existing literature and design a simple geometrical model to highlight the possibility to apply strain differently between the layers (relative strain). Such relative strain is evidenced experimentally by the structural analysis of STM images of a moiré pattern. This relative strain has a strong signature in the density of states measured by STS as supported by tight-binding calculations. Chapter 4 is the continuation of the study as strain was applied directly by the STM tip to the probed moiré pattern. The experimental study shows that this tip-induced interaction follows the moiré period and depends on the tunneling conditions, particularly the bias, that determine the tip-sample distance. STS measurements reveal also an active variation of the density of states leading to instabilities at very low tip-sample distances. Another route to modulate the electronic properties of graphene was taken in Chapter 5 that presents the study of graphene layers grown on a superconductor: tantalum carbide. The growth uses an original process to yield simultaneously tantalum carbide covered with graphene layers which are investigated by transport measurements. The graphene layers grown on tantalum carbide are then studied by STM/STS revealing superconducting moirés of graphene.

CONTENTS

CHAPTER 1

INTRODUCTION TO GRAPHENE AND TWISTED GRAPHENE LAYERS

1.1 Graphene (Monolayer)

1.1.1 Crystallography of graphene

Graphene is a two-dimensional layer of carbon atoms arranged in a honeycomb lattice. The honeycomb lattice is not a Bravais lattice as it cannot be generated from a single atom and two translation vectors. The Bravais lattice of graphene is in fact a triangular lattice with a repeating pattern of two inequivalent atoms, usually called A and B, as shown in Fig. 1.1. The lattice vectors of this triangular lattice are given by

$$\mathbf{a_1} = a\hat{\mathbf{x}} \tag{1.1}$$

$$\mathbf{a_2} = -\frac{a}{2}\hat{\mathbf{x}} + \frac{a\sqrt{3}}{2}\hat{\mathbf{y}} \tag{1.2}$$

where $a = 2.46$ Å is the lattice parameter of graphene.

One can find the lattice vectors $\mathbf{G_1}$ and $\mathbf{G_2}$ of the reciprocal lattice by using $\mathbf{a_i}.\mathbf{G_j} = 2\pi\delta_{ij}$ where δ_{ij} is the Kronecker delta:

$$\mathbf{G_1} = \frac{2\pi}{a}\hat{\mathbf{x}} + \frac{2\pi}{a\sqrt{3}}\hat{\mathbf{y}} \tag{1.3}$$

$$\mathbf{G_2} = \frac{4\pi}{a\sqrt{3}}\hat{\mathbf{y}} \tag{1.4}$$

which also generate a triangular lattice as shown Fig. 1.2. The Brillouin zone (in bold), defined as the Wigner-Seitz cell of the reciprocal lattice, is then

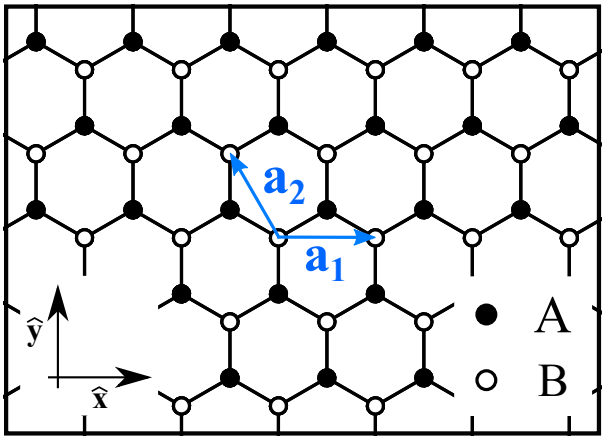

Figure 1.1: Atomic structure of graphene showing the lattice vectors $\mathbf{a_1}$ and $\mathbf{a_2}$ in blue. The two sublattices A and B are depicted respectively with filled and open circles.

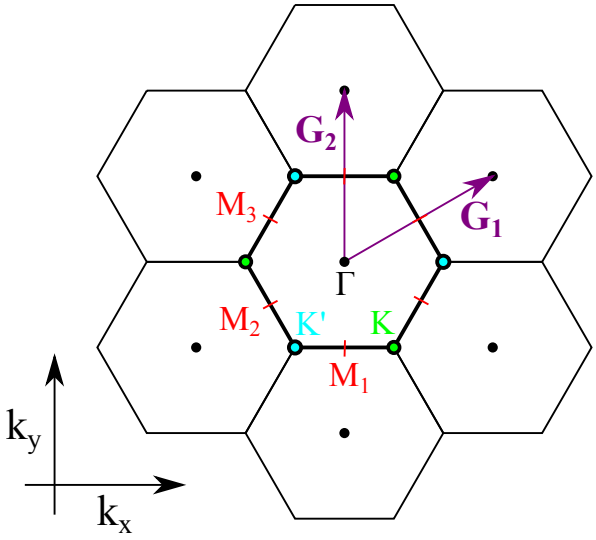

Figure 1.2: Reciprocal lattice of graphene with its lattice vectors $(\mathbf{G_1}, \mathbf{G_2})$ (in purple). The first Brillouin zone is shown in bold with its high-symmetry points: Γ at the center in black, M_i midpoints in red and at the corners the K (green) and K' (cyan) points.

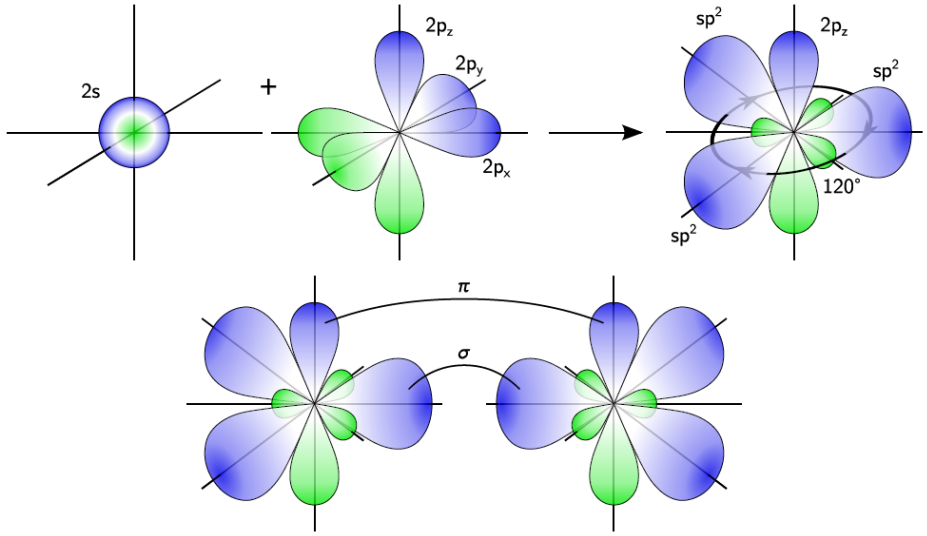

Figure 1.3: Top : Hybridization of the $2s$, $2p_x$ and $2p_y$ orbitals to get the sp^2 orbitals while the $2p_z$ stays unchanged. **Bottom :** σ bond formed by the overlap of the sp^2 orbitals and delocalized π bond formed by the overlap of the $2p_z$ orbitals. From Ref. 7

hexagonal with high-symmetry points named Γ (center), M_i (midpoints of the borders) and K and K' inequivalent corners of the Brillouin zone. Only these two corners are inequivalent as the others can be linked to the K and K' points through a linear combination of the G_i vectors. For the same reason, the M_i points are also inequivalent.

1.1.2 Band structure of graphene

The band structure of graphene was first derived in 1947 by Wallace [98] by a tight-binding model. As the name suggests, the calculations are made supposing that the electrons are 'tightly-bound' to the atoms. In more formal terms, the atomic orbitals of the isolated atoms are supposed to be a suitable basis for the electronic wavefunctions when the atoms are arranged in a crystal. Therefore, the use of the model imposes to firstly determine the atomic orbitals.

In the honeycomb lattice of graphene, each carbon atom is covalently bound to three neighbors by σ bounds. These σ bonds are overlaps of the hybridized orbitals of the carbon atoms. These orbitals are called sp^2 as the two $2p_x$ and $2p_y$ orbitals hybridize with the $2s$ orbital to form the three bonding sp^2 orbitals (Fig. 1.3). The remaining out-of-plane $2p_z$ atomic orbitals

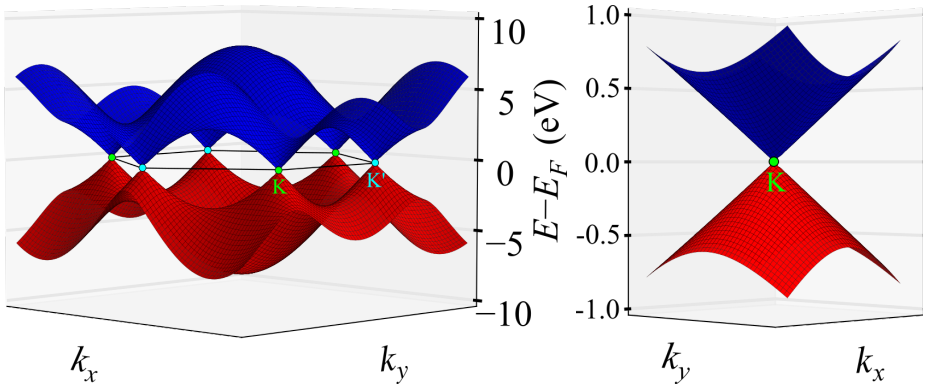

Figure 1.4: Left: Band structure of graphene given by Eq. (1.7). The valence band (in red) and the conduction band (in blue) touch at K (green) and K' (cyan) points situated on the border of the Brillouin zone (in black). **Right :** Zoom at the K point showing the conical structure of the band structure.

form a delocalized π bond that is responsible for the electronic properties in graphene. As a consequence, the tight-binding model is quite simple as it needs to take only these $2p_z$ orbitals into account. When considering only nearest-neighbor coupling, the only relevant hopping term is $t_0 = 2.7$ eV which connects the $2p_z$ orbitals of an atom belonging to the sublattice A and of an atom belonging to the sublattice B. Indeed, one can easily see from Fig. 1.1 that the nearest neighbors of A atoms are B atoms and the other way around. The tight-binding derivation leads to the following dispersion relation [98]:

$$E(\mathbf{k})^2 = t_0^2(1 + 4\cos^2(\frac{k_y a}{2}) + 4\cos(\frac{k_y a}{2})\cos(\frac{k_x\sqrt{3}a}{2})) \tag{1.5}$$

$$= t_0^2(3 + 2\cos(k_y a) + 4\cos(\frac{k_y a}{2})\cos(\frac{k_x\sqrt{3}a}{2})) \tag{1.6}$$

which gives two solutions symmetric with respect to $E = 0$:

$$E(\mathbf{k}) = \pm\, t_0\sqrt{3 + 2\cos(k_y a) + 4\cos(\frac{k_y a}{2})\cos(\frac{k_x\sqrt{3}a}{2})}\,. \tag{1.7}$$

These solutions are plotted Fig. 1.4 in red for the negative energies (the valence band) and in blue for the positive energies (the conduction band). We can see on the figure that the two bands touch at the K (green) and K' (cyan) points on the border of the Brillouin zone (in black) at $E = 0$. It is particularly interesting as a calculation of the filling of the bands shows that

$E = 0$ is in fact the Fermi level of undoped graphene. Therefore, many of the particular electronic properties of graphene are explained by the band structure near these touching points. To have a clearer view of this, we can approximate the dispersion relation near these specific points situated at $\mathbf{K}$ and $\mathbf{K}' = -\mathbf{K}$. If we set $\mathbf{k} = \mathbf{K} + \delta\mathbf{k}$ for a small variation $\delta\mathbf{k}$ around $\mathbf{K}$, a second-order Taylor expansion in $\delta\mathbf{k}$ of Eq. (1.6) yields

$$E(\mathbf{K} + \delta\mathbf{k}) = \pm\frac{at_0\sqrt{3}}{2}|\delta\mathbf{k}| = \pm\hbar v_F|\delta\mathbf{k}| \tag{1.8}$$

where we defined the Fermi velocity of graphene v_F as $\frac{at_0\sqrt{3}}{2\hbar}$. The numerical estimation of this velocity yields $v_F = 1.1 \times 10^6$ m/s. The dispersion relation near the K and K' points is therefore linear as testified by the conical shape of the bands shown Fig. 1.4. This linear dependence is at odds with the parabolic bands encountered in textbook solid-state physics and has strong implications on the low-energy electronic excitations in graphene.

1.1.3 Massless Dirac fermions in graphene

Equation (1.8) is very similar to the relativistic relation that links the energy E and the momentum $\mathbf{p}$ of a particle of rest mass m

$$E^2 = |\mathbf{p}|^2c^2 + m^2c^4 \tag{1.9}$$

where c is the speed of light. Indeed, setting m to 0 and c to v_F yields Eq. (1.8) squared. In fact, the similarity between particle physics and electrons in graphene can be traced back to the Hamiltonian. A derivation of the low-energy Hamiltonian using second-quantization[1] gives a form very similar to the Dirac-Weyl equation for massless fermions. As a consequence, low-energy electronic excitations in graphene behave like massless Dirac fermions. By metonymy, the K and K' points are called Dirac points and the band structure near them Dirac cones.

In addition, while the Dirac equation is an extension of the Schrödinger equation for a relativistic particle, Weyl showed that the wavefunction of such a particle can be described by a two-component spinor. In the case of a massless particule, the two spinor components are independent and the wavefunction has therefore two additional well-defined eigenvalues called the chirality. Due to this, another quantum number enters in the description of the wavefunction of electronic excitations of graphene and is usually called pseudo-spin or isospin. This pseudo-spin adds another degree of freedom linked to the valleys (K and K' points).

[1] See Ref. 7 or 17 for the full treatment

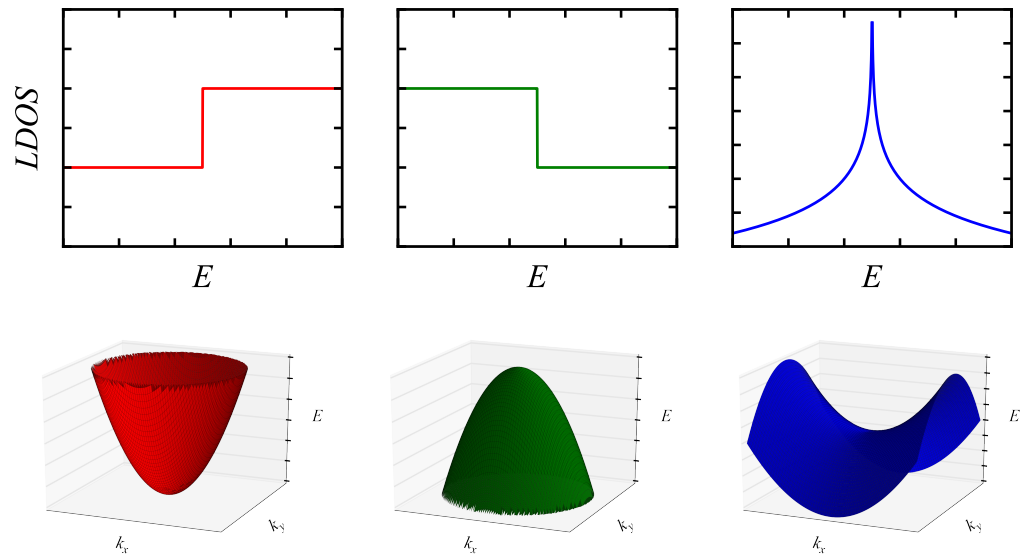

Figure 1.5: Critical points of the band structure and corresponding singularities shapes in 2D systems. Left: Minimum. **Center:** Maximum. **Right:** Saddle point.

1.1.4 Van Hove singularities

Van Hove singularities arise in the density of states at critical points where $\nabla_{\mathbf{k}} E \longrightarrow 0$. [97]. For a 2D system such as graphene, the critical points consist in minima, maxima and saddle points leading to different shaped singularities as shown in Fig. 1.5. The saddle points are particular as they are local minima along a direction and local maxima in the orthogonal direction. Such points leads to logarithmic divergences in the density of states which are the most interesting type of singularities. As a consequence, in the manuscript, the term 'van Hove singularity' will be used only to refer to this particular divergence. Theoretical studies have predicted that electronic instabilities should arise at these singularities triggering the appearance of phases with strong electron-electron interactions such as magnetism or superconductivity [37][2].

Figure 1.4 shows that the graphene band structure display saddle points at the M points of the Brillouin zone and therefore van Hove singularities in the density of states. Unfortunately, these van Hove singularities are located at high energies ($\sim \pm 3$ eV), far from the Fermi level. The study of the phenomena linked to van Hove singularities requires then very heavy doping

[2] Van Hove singularities are notably a considered explanation for the presence of superconductivity in high-T_c compounds such as cuprates.

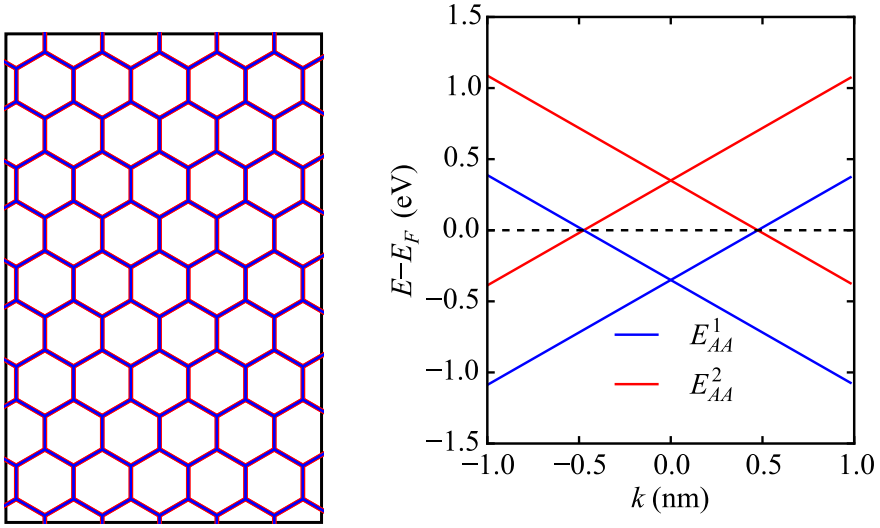

Figure 1.6: Left: AA stacking of two graphene layers (top layer in blue, bottom layer in red) **Right:** Low-energy band structure of the AA stacked bilayer for $t_{AA} = 0.35$ eV. The Dirac cones are preserved and shifted in energy.

making it very challenging.

Twisted graphene layers, consisting in the misorientated stacking of two graphene layers, offer a way to circumvent this problem. It was indeed reported in 2009 [50] that the density of states of twisted graphene layers shows van Hove singularities at low-energy. In addition, the energy of these singularities is tunable with the twist angle θ between the layers, varying between a few meV to almost 1 eV above the Dirac point. This opened a new avenue of research on graphene bilayers, a system that is now presented.

1.2 Graphene bilayers

Before describing the properties of twisted graphene layers, we start with the particular case of graphene bilayers with no twist angle: aligned layers.

1.2.1 $\theta = 0°$: aligned layers

When the two layers are aligned ($\theta = 0°$), two kinds of stacking can occur.

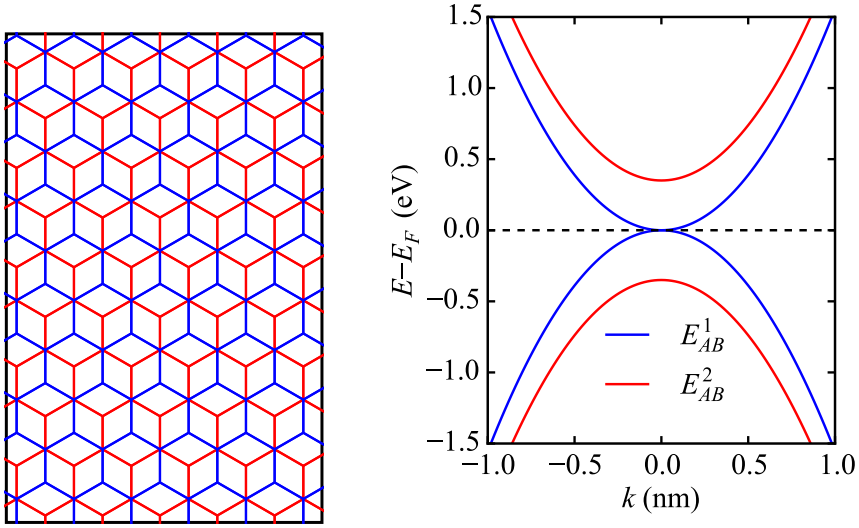

Figure 1.7: Left: AB stacking of two graphene layers (top layer in blue, bottom layer in red) **Right:** Low-energy band structure of the AB stacked bilayer for $t_{AB} = 0.35$ eV. The dispersion is no longer linear but parabolic.

1.2.1.a AA stacking

The situation where the atoms of the top layer are all above atoms of the bottom layer is called AA stacking (left part of Fig. 1.6). For such a stacking, most of the considerations of single-layer graphene still hold. A tight-binding calculation [80] shows that the Dirac cones of both layers are indeed conserved but that they are shifted in energy by the interlayer coupling t_{AA}:

$$E^1_{AA}(\mathbf{K} + \delta\mathbf{k}) = -t_{AA} \pm \hbar v_F |\delta\mathbf{k}| \tag{1.10}$$

$$E^2_{AA}(\mathbf{K} + \delta\mathbf{k}) = t_{AA} \pm \hbar v_F |\delta\mathbf{k}| \,. \tag{1.11}$$

Note that we have two electronic bands (right part of Fig. 1.6) as we added a supplementary free electron by the introduction of another layer.

1.2.1.b AB stacking

The AB stacking is a shift of this AA stacking so that only the A atoms of the top layer are above the B atoms of the bottom layer, hence the name (left part of Fig. 1.7). Such stacking is also named Bernal stacking or graphitic stacking as it is the naturally occuring stacking in graphite crystals discovered by J.D. Bernal in 1924 [10]. Contrary to the AA stacking, the AB stacking breaks the inequivalence between the A and B sublattices present in single layer graphene. A tight-binding calculation shows that the dispersion is no

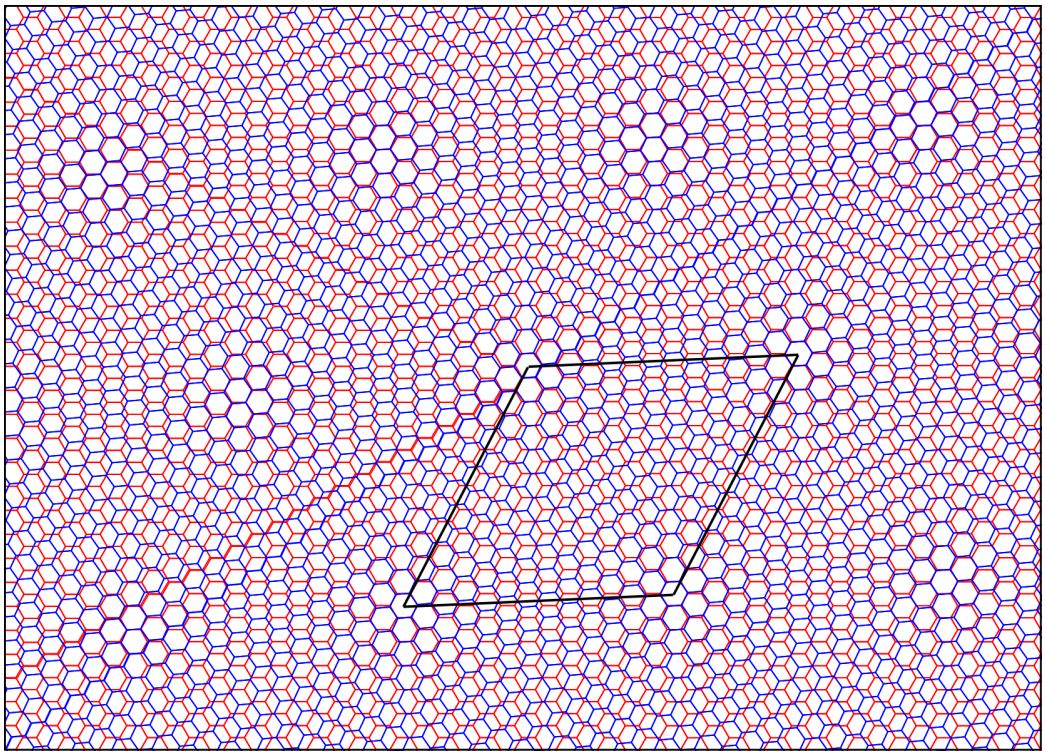

Figure 1.8: Graphene layers with a twist angle $\theta = 5.09°$ between them. The black rhombus represents the cell of the superperiodic moiré pattern which consists in an alternation of local AA stacked regions and AB stacked regions.

longer linear but parabolic (right part of Fig. 1.7) near the K and K' points:

$$E^1_{AB}(\mathbf{K}+\delta\mathbf{k}) = \pm\frac{\hbar^2 v_F^2}{t_{AB}}|\delta\mathbf{k}|^2 \tag{1.12}$$

$$E^2_{AB}(\mathbf{K}+\delta\mathbf{k}) = \pm(t_0 + \frac{\hbar^2 v_F^2}{t_{AB}}|\delta\mathbf{k}|^2)\,. \tag{1.13}$$

1.2.2 $\theta \neq 0°$: twisted graphene layers and moiré pattern

The application of the twist angle $\theta \neq 0°$ is more complex than what was presented in Section 1.2.1. Indeed, in the AA and AB stacked cases, the system was still translationally invariant by the lattice vectors of graphene. Fig. 1.8 shows that it is no longer the case for twisted graphene layers as the mismatched lattices interfere to give a superperiodic pattern called a moiré. The properties of the twisted graphene layers pattern are strongly linked to the moiré pattern that must therefore be properly described. We will hence

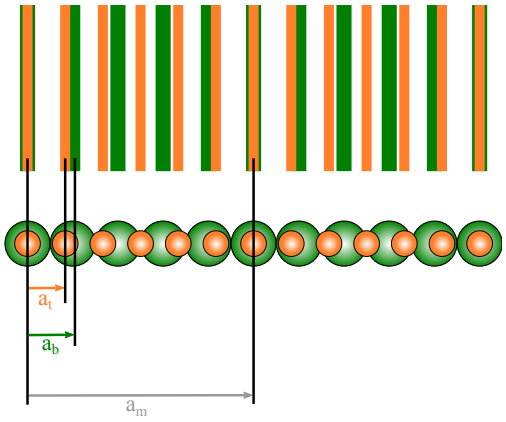

Figure 1.9: Mismatched 1D lattices : top layer in orange, bottom layer in green. The bottom part is a ball model of the atomic lattices whereas the top part shows the same lattices but with lines to make the 1D moiré pattern visually appear. The beating matches the moiré periodicity (see text)

now introduce the commensurability formalism to describe moiré patterns in the general case.

1.2.2.a Commensurability formalism

As seen on Fig. 1.8, a moiré pattern is formed of alternating areas when the two interfering lattices are in phase (AA regions for twisted graphene layers) and in antiphase (AB regions for twisted graphene layers) with a continuous transition in between. For the sake of simplicity, we start with a one-dimensional example.

Moirés and beatings in 1D Fig. 1.9 shows two mismatched 1D atomic lattices (top layer in orange of periodicity a_t and bottom layer of periodicity a_b) with its equivalent in the form of lines to show visually the 1D moiré pattern (of periodicity a_m). 'Bright' regions appear when the lines overlap which is when the two lattices are in phase. The commensurability formalism consists in finding coincidence relations between the moiré and the atomic lattices. In this simple case, to go from one overlap of the lines to the next one, we need to span 5 green lines and 6 orange lines. The coincidence or commensurability relations are then given by

$$a_m = 6a_t \tag{1.14}$$

$$a_m = 5a_b \tag{1.15}$$

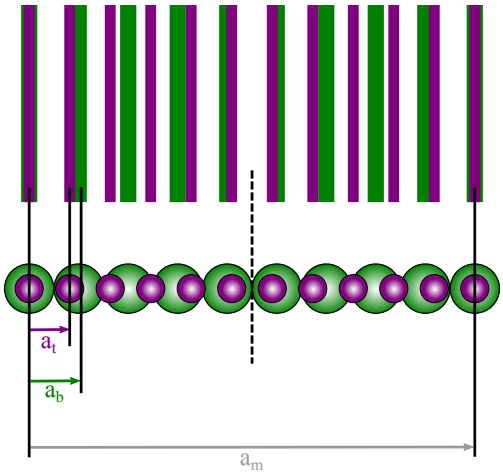

Figure 1.10: Mismatched 1D lattices : top layer in purple, bottom layer in green. The bottom part is a ball model of the atomic lattices whereas the top part shows the same lattices but with lines to make the 1D moiré pattern visually appear. The beating underlined by the dashed line does not match the moiré periodicity which is two times larger (see text)

or in terms of spatial frequencies $k = 2\pi/a$:

$$k_t = 6k_m \tag{1.16}$$

$$k_b = 5k_m\,. \tag{1.17}$$

Given the atomic lattices, the moiré pattern is therefore fully defined by the integers $(6, 5)$. A similar but not equivalent case is presented in Fig. 1.10. In this case, the coincidence relations are given by

$$a_m = 11a_t \tag{1.18}$$

$$a_m = 9a_b \tag{1.19}$$

When considering the line model, it looks like that there is a bright region at the dashed line location where the lattices seem in phase. However, this bright region is not equivalent to the ones at the edges as shown by the difference of local stacking in the ball model. This means that the alternation of bright regions, appearing similar to the eye and in the STM images shown later, called the beating, does not match the real periodicity (the moiré periodicity) a_m shown in gray. While it is possible to spot visually the difference between the 'bright' regions in the simple presented case, it becomes very difficult when dealing with larger moiré periods and even more when dealing with STM images.

More generally, the relation between the spatial frequencies

$$k_t = ik_m \tag{1.20}$$
$$k_b = mk_m \tag{1.21}$$

can be used to give the beating frequency k_{beat}, coming from the interference between the wavevectors k_t and k_b:

$$k_{beat} = |k_t - k_b| = |(i-m)k_m| \,. \tag{1.22}$$

It shows that the beating, the visually seen alternation, coincides with the moiré periodicity only if $i-m = \pm 1$ which was the case of Fig. 1.9 but not of Fig. 1.10. While the beating is the alternation of similar but not equivalent atomic arrangements, the moiré period is the true periodicity of the system. This distinction is primordial to determine the exact structure of the moiré and the lattices forming it.

Moirés in 2D Artaud *et al.*[6] developed a two-dimensional extension of this formalism with the relation between the moiré lattice vectors ($\mathbf{a_{m_1}}$,$\mathbf{a_{m_2}}$), the lattice vectors of the top layer ($\mathbf{a_{t_1}}$,$\mathbf{a_{t_2}}$) and of the bottom layer ($\mathbf{a_{b_1}}$,$\mathbf{a_{b_2}}$) given by

$$\mathbf{a_{m_1}} = i\mathbf{a_{t_1}} + j\mathbf{a_{t_2}} = m\mathbf{a_{b_1}} + n\mathbf{a_{b_2}} \tag{1.23}$$
$$\mathbf{a_{m_2}} = k\mathbf{a_{t_1}} + l\mathbf{a_{t_2}} = q\mathbf{a_{b_1}} + r\mathbf{a_{b_2}} \tag{1.24}$$

where (i, j, k, l, m, n, q, r) are integers. Such relations can be written in matrix formalism:

$$\begin{pmatrix} \mathbf{a_{m_1}} \\ \mathbf{a_{m_2}} \end{pmatrix} = \begin{pmatrix} i & j \\ k & m \end{pmatrix} \begin{pmatrix} \mathbf{a_{t_1}} \\ \mathbf{a_{t_2}} \end{pmatrix} = \begin{pmatrix} m & n \\ q & r \end{pmatrix} \begin{pmatrix} \mathbf{a_{b_1}} \\ \mathbf{a_{b_2}} \end{pmatrix} . \tag{1.25}$$

For practical purposes, in the following, we are going to study commensurability in the Fourier space. It is therefore useful to translate these relations in the reciprocal space:

$$\begin{pmatrix} \mathbf{k_{t_1}} \\ \mathbf{k_{t_2}} \end{pmatrix} = \begin{pmatrix} i & k \\ j & m \end{pmatrix} \begin{pmatrix} \mathbf{k_{m_1}} \\ \mathbf{k_{m_2}} \end{pmatrix} \tag{1.26}$$
$$\begin{pmatrix} \mathbf{k_{b_1}} \\ \mathbf{k_{b_2}} \end{pmatrix} = \begin{pmatrix} m & q \\ n & r \end{pmatrix} \begin{pmatrix} \mathbf{k_{m_1}} \\ \mathbf{k_{m_2}} \end{pmatrix} \tag{1.27}$$

where ($\mathbf{k_{t_1}}, \mathbf{k_{t_2}}$),($\mathbf{k_{b_1}}, \mathbf{k_{b_2}}$) and ($\mathbf{k_{m_1}}, \mathbf{k_{m_2}}$) are the reciprocal lattice vectors of respectively the top layer, the bottom layer and the moiré.

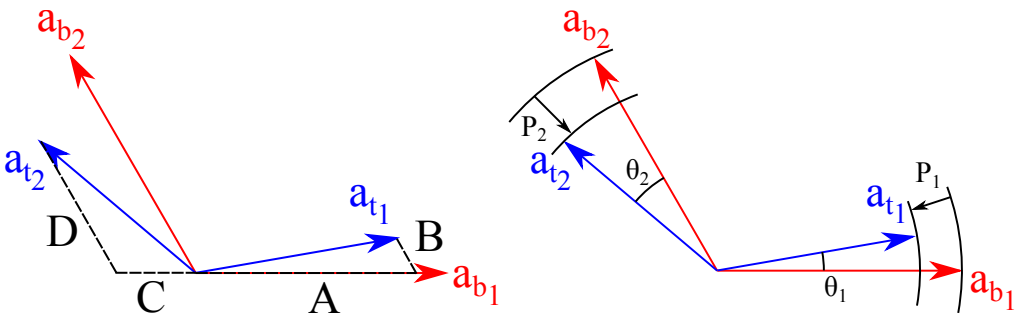

Figure 1.11: Left : Relations between $(\mathbf{a_{b_1}}, \mathbf{a_{b_2}})$ and $(\mathbf{a_{t_1}}, \mathbf{a_{t_2}})$ written using Park-Madden coefficients **Right :** Relations written using extended Wood's notation

More importantly, the commensurability analysis allows to derive the structural relations between the layers. These relations can be written in a general form using the Park-Madden matrix:

$$\begin{pmatrix} \mathbf{a_{t_1}} \\ \mathbf{a_{t_2}} \end{pmatrix} = \begin{pmatrix} A & B \\ C & D \end{pmatrix} \begin{pmatrix} \mathbf{a_{b_1}} \\ \mathbf{a_{b_2}} \end{pmatrix} \tag{1.28}$$

where A, B, C and D must be rational numbers ($\in \mathbb{Q}$) to achieve commensurability [74]. The coefficients of the Park-Madden matrix are in fact the coordinates of the vectors $(\mathbf{a_{t_1}}, \mathbf{a_{t_2}})$ in the basis of $(\mathbf{a_{b_1}}, \mathbf{a_{b_2}})$ as shown in the left part of Fig. 1.11. The Park-Madden matrix can be linked to the integers (i, j, k, l, m, n, q, r):

$$\begin{pmatrix} A & B \\ C & D \end{pmatrix} = \frac{1}{il - jk} \begin{pmatrix} lm - jq & ln - jr \\ -km + iq & -kn + ir \end{pmatrix} . \tag{1.29}$$

It can be more straightforward to express separately the relation between $\mathbf{a_{t_1}}$ and $\mathbf{a_{b_1}}$ and the relation between $\mathbf{a_{t_2}}$ and $\mathbf{a_{b_2}}$. This can be done in the most general case with the extended Wood's notation $(P_1 R\theta_1 \times P_2 R\theta_2)$ where $P_1 = \dfrac{|\mathbf{a_{t_1}}|}{|\mathbf{a_{b_1}}|}$, θ_1 is the angle between $\mathbf{a_{t_1}}$ and $\mathbf{a_{b_1}}$, $P_2 = \dfrac{|\mathbf{a_{t_2}}|}{|\mathbf{a_{b_2}}|}$ and θ_2 is the angle between $\mathbf{a_{t_2}}$ and $\mathbf{a_{b_2}}$. The vector $\mathbf{a_{t_1}}$ is therefore linked to $\mathbf{a_{b_1}}$ by a scaling of ratio P_1 and a rotation of angle θ_1 which can be more easily pictured (right part of Fig. 1.11). In this formalism, the matrix linking ($\mathbf{a_{t_1}}$,$\mathbf{a_{t_2}}$) and ($\mathbf{a_{b_1}}$,$\mathbf{a_{b_2}}$) is given by

$$\begin{pmatrix} \mathbf{a_{t_1}} \\ \mathbf{a_{t_2}} \end{pmatrix} = \begin{pmatrix} P_1(\cos\theta_1 + \dfrac{\sin\theta_1}{\sqrt{3}}) & \dfrac{2P_1}{\sqrt{3}}\sin\theta_1 \\ -\dfrac{2P_2}{\sqrt{3}}\sin\theta_2 & P_2(\cos\theta_2 - \dfrac{\sin\theta_2}{\sqrt{3}}) \end{pmatrix} \begin{pmatrix} \mathbf{a_{b_1}} \\ \mathbf{a_{b_2}} \end{pmatrix} \tag{1.30}$$

when considering a hexagonal support lattice. The parameters P_1, P_2, θ_1 and θ_2 can be found from the commensurability by identifying this matrix with the Park-Madden matrix defined in (1.28):

$$P_1 = \sqrt{A^2 + B^2 - AB} \tag{1.31}$$

$$P_2 = \sqrt{C^2 + D^2 - CD} \tag{1.32}$$

$$\theta_1 = \arctan \frac{B\sqrt{3}}{2A - B} \tag{1.33}$$

$$\theta_2 = \arctan \frac{C\sqrt{3}}{2C - D}\,. \tag{1.34}$$

The strains levels between the layers $\varepsilon_{biaxial}$ and $\varepsilon_{uniaxial}$ are then given by

$$\varepsilon_{biaxial} = \sqrt{X - \sqrt{W}} - 1 \tag{1.35}$$

$$\varepsilon_{uniaxial} = \sqrt{X + \sqrt{W}} - \sqrt{X - \sqrt{W}} \tag{1.36}$$

where $X = \dfrac{2(P_1^2 + P_2^2) + A}{3}$, $Y = \sqrt{\dfrac{4P_1^2P_2^2 - A^2}{3}}$ and $W = X^2 - Y^2$. The commensurability gives then a robust framework to study moiré patterns as every structural parameter (strain, shear and rotation between the two layers) will fall directly from the set of integers (i, j, k, l, m, n, q, r).

Moreover, the distinction between beatings and moiré can be discussed within this formalism, similarly to the 1D case. An example of two similar moirés formed by the misorientated stacking of two unstrained graphene layers is presented Fig. 1.12. The top moiré comes from a twist angle 4.41° and was generated by a set of commensurability indices chosen so that $i - m = 1$. In this case, the beating coincides with the moiré as Eq. (1.22) yields $k_{beat} = k_m$. The distance between two bright spots is the real periodicity of the system as evidenced by the same exact atomic arrangement of neighboring AA regions (AA1 and AA2). On the other hand, the bottom moiré comes from a close twist angle 4.47° but was generated by a set of commensurability indices chosen so that $i - m = 2$. This time, Eq. (1.22) yields $k_{beat} = 2k_m$ meaning that the moiré periodicity is in fact twice the distance between two bright spots. To have the exact same atomic arrangement, it is therefore necessary to span two beatings. The closer inspection shows indeed that the two atomic arrangements are not exactly the same between neighboring AA regions (AA1 and AA2).

Commensurable and incommensurable moirés The commensurability has different definitions depending on the authors. In this manuscript,

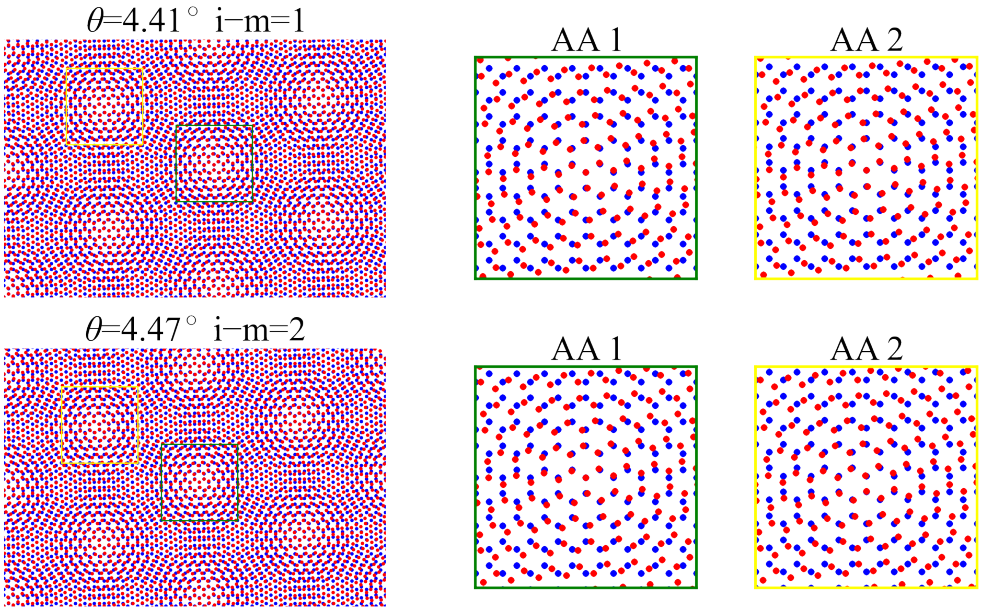

Figure 1.12: Top: Moiré generated from two misorientated ($\theta = 4.41°$) unstrained graphene layers with a set of commensurability indices so that $i - m = 1$. The beating coincides with the true moiré periodicity so that neighboring AA regions show the same exact atomic arrangement. **Bottom:** Moiré generated from two misorientated ($\theta = 4.47°$) unstrained graphene layers with a set of commensurability indices so that $i - m = 2$. The moiré periodicity is two times the beating so that neighboring AA regions show different atomic arrangements.

a moiré pattern that verify the relations (1.23) and (1.24) is called **commensurate** with the atomic periodicities forming it[3]. We can picture it as the possibility to find sites where the lattices overlap exactly. It means that the two-layers system acquires a new periodicity that is the moiré period. Such 1D commensurate moirés were shown on Fig. 1.9 and Fig. 1.10. On the contrary, in the **incommensurate** case, starting from a site where the lattices of the two layers overlap, it is impossible to find exactly again the same overlap in the whole system. An incommensurate system is therefore not periodic. A 1D example is the system where $a_t = \sqrt{2}a_b$.

1.2.2.b Commensurability analysis of twisted graphene layers

The presented approach presents a robust framework to study moiré patterns that relies on the determination of the indices (i, j, k, l, m, n, q, r). This section explains how to practically find these indices for experimental imaged moiré patterns. The starting point is the following set of equations of the reciprocal space:

$$\begin{pmatrix} \mathbf{k_{t_1}} \\ \mathbf{k_{t_2}} \end{pmatrix} = \begin{pmatrix} i & k \\ j & m \end{pmatrix} \begin{pmatrix} \mathbf{k_{m_1}} \\ \mathbf{k_{m_2}} \end{pmatrix} \tag{1.37}$$

$$\begin{pmatrix} \mathbf{k_{b_1}} \\ \mathbf{k_{b_2}} \end{pmatrix} = \begin{pmatrix} m & q \\ n & r \end{pmatrix} \begin{pmatrix} \mathbf{k_{m_1}} \\ \mathbf{k_{m_2}} \end{pmatrix} . \tag{1.38}$$

These equations show that the commensurability indices are simply the coordinates of $(\mathbf{k_{t_1}}, \mathbf{k_{t_2}})$ and $(\mathbf{k_{b_1}}, \mathbf{k_{b_2}})$ in the basis of $(\mathbf{k_{m_1}}, \mathbf{k_{m_2}})$. A decomposition of the Fourier transform in the basis of $(\mathbf{k_{m_1}}, \mathbf{k_{m_2}})$ will then allow to find these integers as will be presented in the following example.

Example In this example, we will show how to derive the commensurability indices of the moiré pattern presented Fig. 1.13. The Fourier transform of this image shows the spots of the graphene layers and of the beating corresponding to the alternation in brightness as explained in the previous section. The Fourier transform is then decomposed in the mesh generated by the beating vectors, in gray on Fig. 1.14.

The commensurability hypothesis (Eqs. 1.38) imposes for the graphene reciprocal vectors to have integer coordinates in the basis of the moiré reciprocal vectors. If the moiré reciprocal vectors $(\mathbf{k_{m_1}}, \mathbf{k_{m_2}})$ do not coincide with the beating reciprocal vectors $(\mathbf{k_{beat_1}}, \mathbf{k_{beat_2}})$, the graphene reciprocal vectors do not have integer coordinates in the basis of decomposing beating

[3] In that sense, we adopt the Euclid's definition of commensurability which was 'the ratio of two distances gives a rational number', distances being in our case lattice parameters.

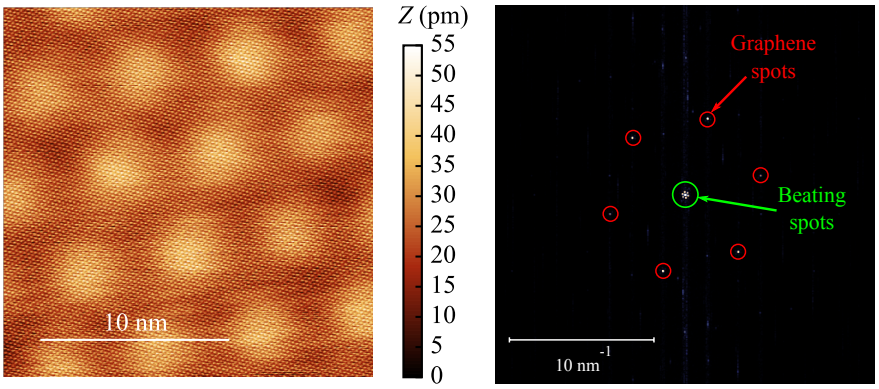

Figure 1.13: Left: STM image of a moiré formed by two twisted graphene layers ($V_b = 1$ V, $I_t = 500$ pA) **Right:** Fourier transform of the STM image showing the graphene spots encircled in red and the beating spots encircled in green

mesh. This is what allows to uncover situations where the beating and the moiré do not coincide.

For the case considered here, the graphene reciprocal vectors have integer coordinates in the basis of the beating reciprocal vectors as the graphene spots fall on nodes of the basis. The beating coincides with the moiré periodicity allowing us to read the commensurability indices directly. The reciprocal vectors of the top layer are easy to find as they are the most intense in the Fourier transform. The bottom layer is not directly observed by STM which means that we should not see the bottom layer spots in the Fourier transform. They can however be deduced from the beating and top layer vectors as $k_{beat} = k_t - k_b$. Therefore, one of the beating overtones near the top layer spot corresponds to the bottom layer spot. We chose it to be the closer in length to the top layer vector since both vectors are Fourier transforms of graphene lattices. We then find the coordinates of the graphene and substrate vectors in the mesh, respectively in cyan and red on Fig. 1.14 with the commensurability indices:

$$\begin{array}{cccc} i = 15 & j = -14 & k = 14 & l = 29 \\ m = 14 & n = -15 & q = 15 & r = 29\,. \end{array} \tag{1.39}$$

From these indices, the Park-Madden matrix is found and through it the extended Woods' notation of the twisted graphene layers system:

$$(P_1 R\theta_1 \times P_2 R\theta_2) = (1R2.28^\circ \times 1R2.28^\circ)\,. \tag{1.40}$$

This shows that the lattice vectors of the top layer have the same modulus than the ones of the bottom layers but are rotated by $\theta = 2.28^\circ$. The moiré

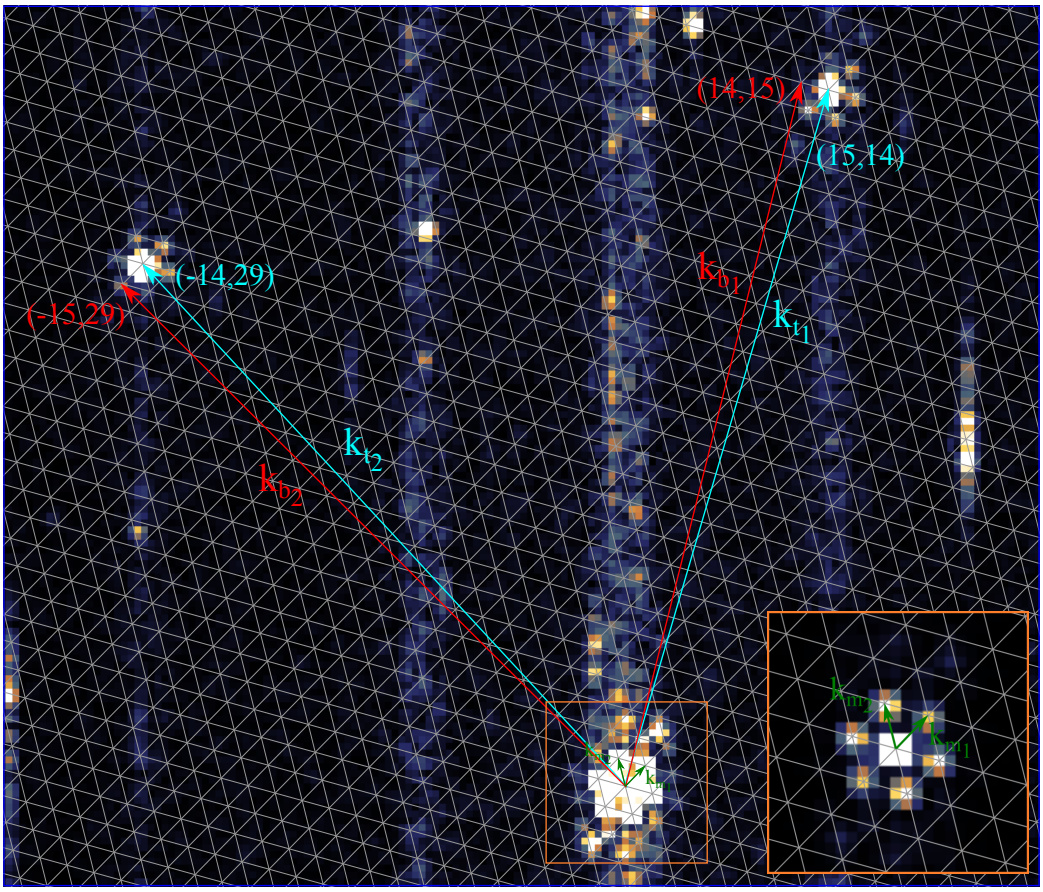

Figure 1.14: Decomposition of the Fourier transform of the STM image in Fig. 1.13 in the basis of the beating vectors, that coincide with the moiré vectors in this case. Inset: Center of the Fourier transform showing the beating/moiré vectors

arises from the mismatch due to the rotation without any difference in the lattice constants of the layers.

Indices for unstrained graphene layers In fact, in the case of unstrained twisted graphene layers, the symmetries of the system imposes relations between the commensurability indices:

$$\begin{array}{ll} k = -j & l = i - j \\ m = -j & n = -i \\ q = i & r = i - j\,. \end{array} \tag{1.41}$$

This means that the two indexes (i, j) fully describe the structure of unstrained twisted graphene layers with a given angle θ. Consequently, we have a direct relation between the angle θ and the integers (i, j) for the commensurate moiré patterns[4]:

$$\cos\theta = \frac{4ij - i^2 - j^2}{2(i^2 + j^2 - ij)}\,. \tag{1.42}$$

In the presented example, the two indices are $i = 15$ and $j = -14$ which leads to $\theta = 2.28°$. This formalism describing bilayers described by two indices forms the basis for the theoretical studies of the twisted graphene layers as it allows to derive easily periodic moiré structures of almost any desired twist angle θ [16]. It was therefore widely used for theoretical investigations of the electronic properties of twisted graphene layers [54, 55, 60, 90, 91] that are discussed in the following section.

1.2.3 Electronic properties of twisted graphene layers

The band structure of twisted graphene layers can be derived from a tight-binding model with hoppings between the layers to take into account the interlayer coupling. Two characteristic interaction regimes can be described: the large angle regime ($\theta > 2°$) where the layers are mostly decoupled with the interlayer interaction acting as a perturbation and the small angle regime ($\theta < 2°$) where the strong interaction between the layers leads to the appearance of new phenomena.

1.2.3.a Large angles ($\theta > 5°$)

The graphene layers are mostly decoupled for large angles θ between them. In reciprocal space, the bilayer can therefore be described by the two

[4]Note that this formula depends on the convention used for the graphene lattice vectors. The given formula is given for an angle of 120° between the direct lattice vectors of unstrained graphene.

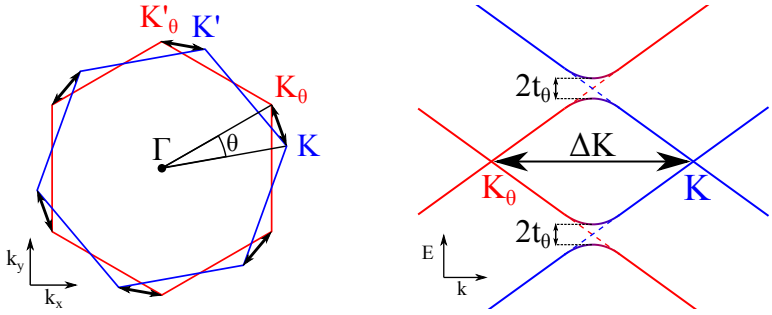

Figure 1.15: Left: Brillouin zones of the rotated layers (top layer in blue, bottom layer in red). The ΔK are shown in black double arrows. **Right:** Anti-crossing Dirac cones of the two layers

band structures of the layers with their respective Brillouin zones rotated by θ as shown in Fig. 1.15. The Dirac cones of the layers are separated by the wavevector

$$\Delta K = 2|\mathbf{K}| \sin\left(\frac{\theta}{2}\right) . \tag{1.43}$$

The interlayer coupling only manifests itself at the two energies (symmetric with respect to the Dirac point) where the Dirac cones cross each other as shown in Fig. 1.15. It induces an anti-crossing of magnitude $2t_\theta = 0.216$ eV, the interlayer hopping term. This hopping term is independent from θ for large angles [91]. Each anti-crossing leads to the formation of a saddle point and of a local extremum in the band structure. The anti crossing energy level closer to the Dirac energy is the saddle point with a maximum of the band structure in the ΔK direction and a minimum in the orthogonal direction. Therefore, the density of states of twisted graphene layers show two van Hove singularities at positive and negative energy with respect to the Dirac point.

These moiré van Hove singularities were first reported by Li *et al.* [50]. Their results displayed in Fig. 1.16 show the differential conductance, proportional to the local density of states, measured by Scanning Tunneling Spectroscopy in regions without (G) and with a moiré pattern (M1,M2) imaged by Scanning Tunneling Microscopy. The density of states in moiré regions shows sharp van Hove singularities centered around the Dirac point which are absent from the G area.

An interesting property of these van Hove singularities is that their energy is tunable with the angle θ. One can easily see from Fig. 1.15 that the energy of the crossing depends on the wavevector ΔK and therefore on θ. As the energy dispersion is given by $E(k) = \hbar v_F k$, the crossing energy between the

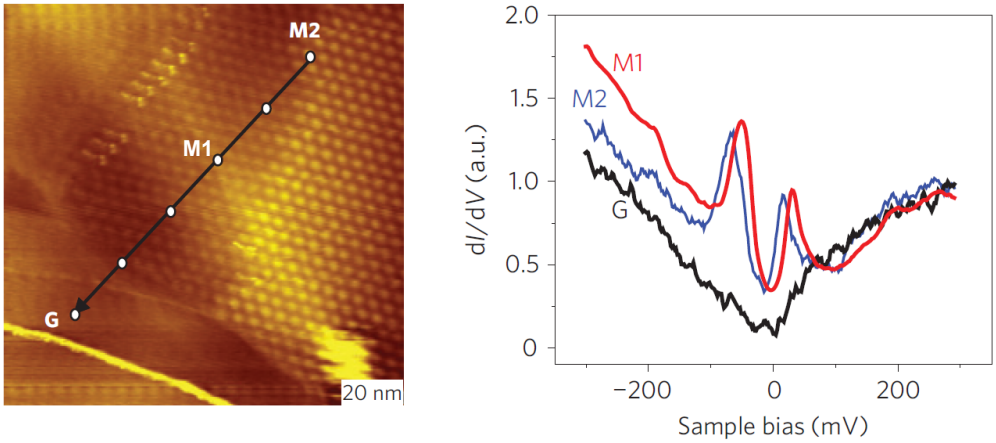

Figure 1.16: Left: Scanning Tunneling Microscopy image showing the regions without (G) and with moiré pattern (M1,M2). **Right:** STS measurements in the regions G, M1 and M2. Van Hove singularities appear in the regions M1 and M2 that shows the moiré pattern. Adapted from Ref. 50

cones is simply given by $E(\frac{\Delta K}{2}) = \hbar v_F \frac{\Delta K}{2}$. The anticrossing of the cones then induces a shift in energy of t_θ so that the energy of the saddle point is given by

$$E_{saddle} = \hbar v_F \frac{\Delta K}{2} - t_\theta \,. \tag{1.44}$$

The splitting of the vHs from this simple geometric approach is then

$$\Delta E_{vHs} = 2E_{saddle} = \hbar v_F \Delta K - 2t_\theta \tag{1.45}$$

which is exactly what was derived from a continuum model in Ref. 55.

This angle dependence has been experimentally investigated by several groups [50, 101, 106]. We present here the work by Brihuega *et al.*[15] that studied several moiré patterns of different twist angles shown Fig. 1.17. The authors were then able to compare the experimental energies of the van Hove singularities to the energies calculated by tight-binding and given by Eq. (1.45). Figure 1.18 shows that the agreement between the experiment, tight-binding and continuum equation is quite good despite a slight underestimation of the splitting by the theoretical results.

1.2.3.b Small angles ($2° < \theta < 5°$): Fermi velocity renormalization

At small angles, the Dirac cones are so close that the layers cannot be considered decoupled anymore. Notably the continuum equation cannot be

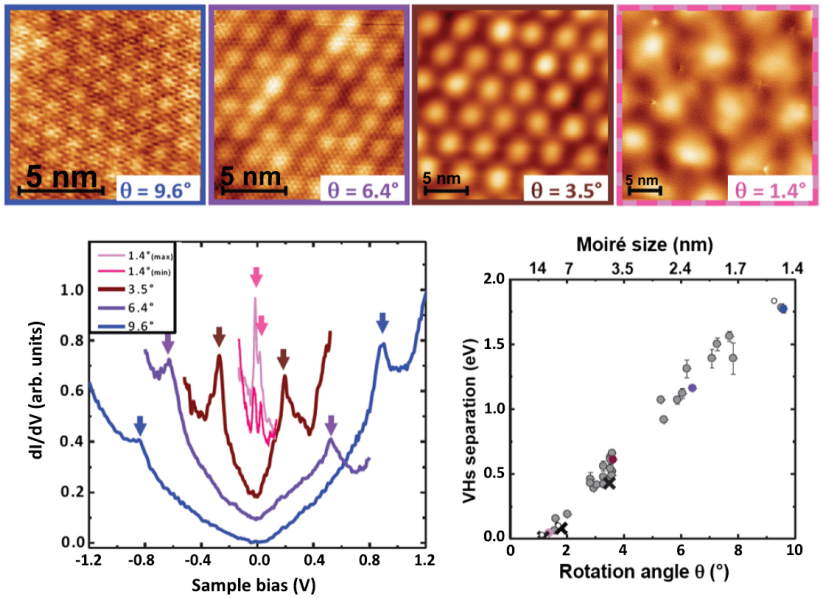

Figure 1.17: Top: Scanning Tunneling Microscopy of twisted graphene layers of different twist angles θ. **Bottom left:** Scanning Tunneling Spectroscopy spectra showing the van Hove singularities for the different moiré patterns (arrows). **Bottom right:** Energy of the probed van Hove singularities with respect to the twist angle between the layers. After Ref. 15

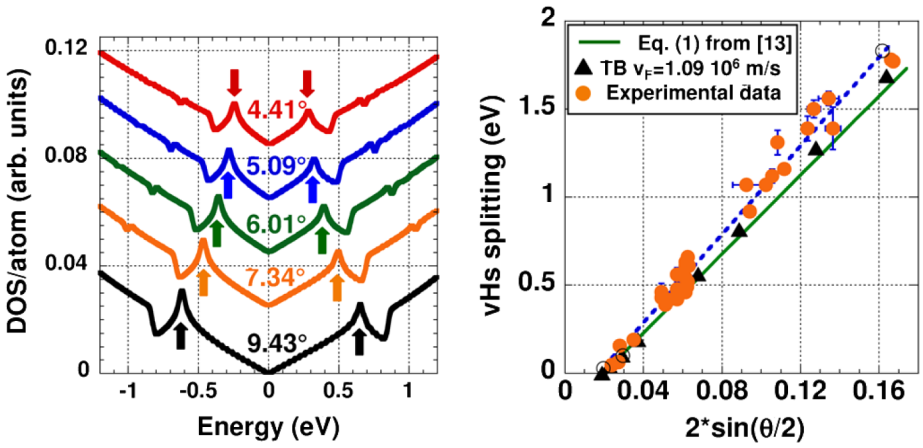

Figure 1.18: Left: Tight-binding calculation of the density of states of moiré patterns with different θ. **Right:** Splitting of the van Hove singularities for the experimental data (orange dots), the tight-binding calculations (black triangles) and the continuum equation (solid line). After Ref. 15.

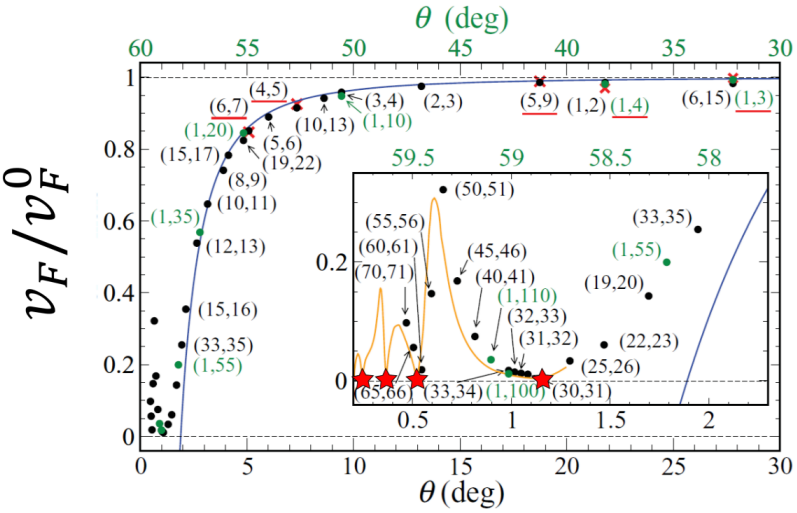

Figure 1.19: Ratio between the Fermi velocity of the twisted graphene layers (v_F) and the one of monolayer graphene (v_F^0). The dots show results of tight-binding calculations, the blue line the continuum model from Ref. 54 and the orange line the continuum model from Ref. 13. The red stars correspond to the magic angles where $v_F = 0$. Adapted from Ref. 91

used anymore for such angles. New phenomena appear owing to the enhanced interlayer coupling.

In twisted graphene layers of large twist angle, the Fermi velocity in the layers equals that of monolayer graphene: $v_F^0 = 1.1 \times 10^6$ m/s. Numerous theoretical studies [13, 54, 90, 91] have shown that this is no longer the case for small twist angles as the Fermi velocity is reduced when the angle decreases as shown on Fig. 1.19. For $\theta > 5°$, tight-binding calculations on twisted graphene layers[5] agree with the large-angles continuum model of Ref. 54 (blue line in Fig. 1.19) which predicts a monotonous decrease of the Fermi velocity. This model however breaks down for $\theta < 2°$ where the tight-binding calculations and the small-angles continuum model of Ref. 13 predict a non-trivial dependence of the Fermi velocity with θ. There is a certain set of angles, called magic angles (red stars in Fig. 1.19), for which the Fermi velocity is equal to 0. It means that for this series of angles, given approximately by $\theta_n = \dfrac{1.05°}{n}$ [13], the conduction and valence bands of graphene are flat leading to the complete localization of the electrons at low energy. Such behavior has yet to be observed experimentally.

[5]Defined by their two indices (i, j) as discussed previously

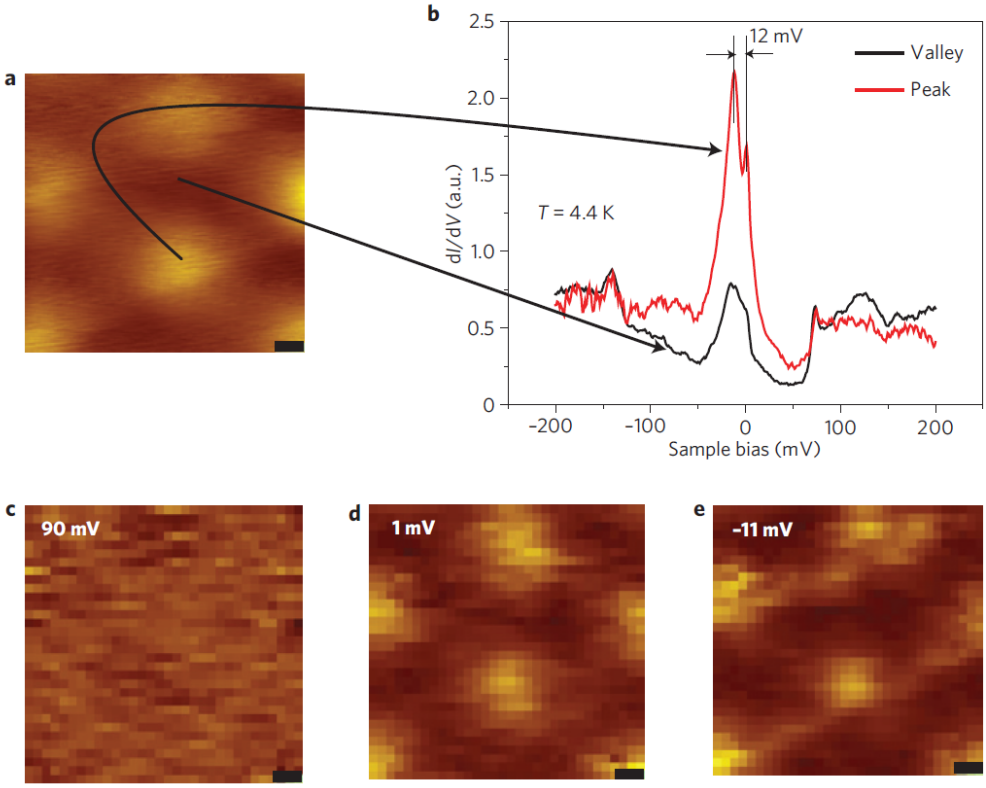

Figure 1.20: Top left: STM image of a moiré pattern with $\theta = 1.16°$. **Top right:** STS spectra recorded in the AA region (peak) and AB region (valley) showing localization of the vHs in the AA regions. **Bottom:** dI/dV maps at different indicated bias showing localization in the AA region at low energies. All scale bars are 2 nm. From Ref. 50

1.2.3.c Very small angles ($\theta < 2°$): localization of low-energy electronic states

While the complete localization of electrons can only be achieved for certain magic angles, a weaker form of this localization exists for the low-energy electronic states in structures with a small twist angle. Li *et al.*[50] already reported that for $\theta = 1.16°$ the van Hove singularities were more intense in AA regions (peak) than in AB regions (valley) of the moiré as shown Fig. 1.20. The dI/dV maps at low energies show that the electronic states are indeed localized in AA regions for these energies. This result is confirmed by theoretical investigations by tight-binding calculations [90]. Figure 1.21 shows that the electronic states at $E = 0$ (red dots) are concentrated in AA regions for the small angle structure (right) but not for the large angle struc-

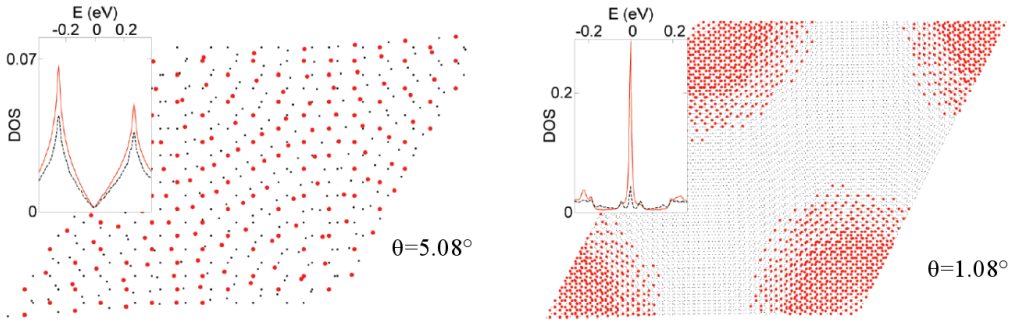

Figure 1.21: Repartition of one eigenstate at K with Dirac energy, E=0, for $\theta = 5.08°$ (left) and $\theta = 1.08°$ (right). Black small dots are the positions of all atoms, red large dots are atoms on which 80% of the electronic state is localized. Insert: Tight-binding density of states (states per atom): The solid red line is the local density of states on atoms located at the center of a AA zone, the dashed black line is the total density of states. Adapted from Ref. 90

ture (left). The absence of this localization effect for large angles has also been observed experimentally [50]. Twisted graphene layers offer therefore a way to achieve localization of the electrons in graphene tunable with the twist angle θ.

Higher order moiré bands The reduction of the twist angle θ decreases the energy of the van Hove singularities but also of the features involving higher order moiré bands. Figure 1.22 from Ref. 101 shows indeed that additional dips appear in the local density of states following the same angle dependence as the van Hove singularities. The first dip is easily explained as it arises from the already discussed anti-crossing due to interlayer coupling. This translates as a decrease of the density of states at the energies immediately above the saddle point which is what is observed.
The second dip is however more difficult to interpret. Several groups [19, 70, 105] interpret them as superlattice Dirac points that are predicted to form when a periodic potential is applied to a graphene layer [72]. Such superlattice points were observed by Landau levels spectroscopy for graphene on hexagonal boron nitride (hBN) [77]. A concurrent interpretation by Wong *et al.* [101] and Kim *et al.* [43] is the partial opening of a gap (or 'mini-gap') induced by the periodic potential of the moiré. This would be very similar to the origin of the first dip but for higher order moiré bands and will give therefore the same signature in the LDOS.

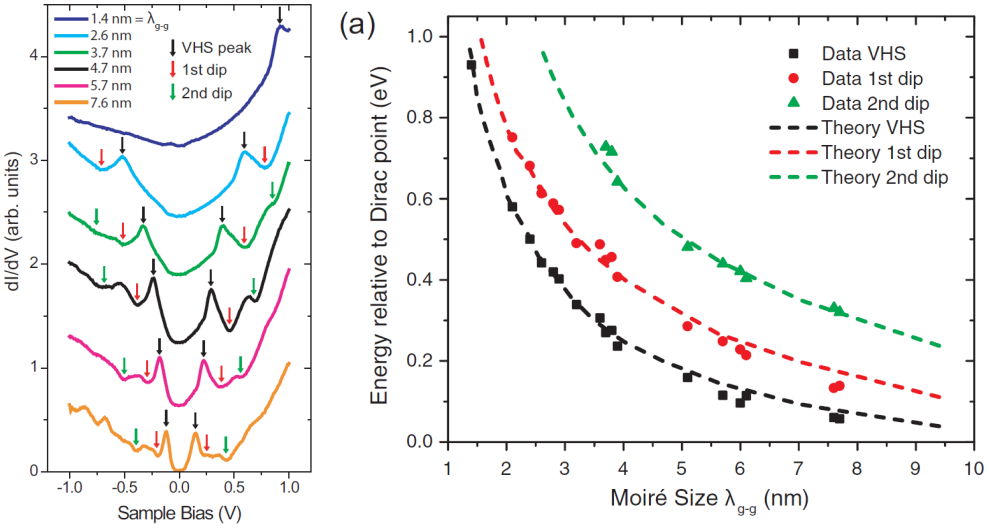

Figure 1.22: Left: STS spectra for different moiré patterns that show van Hove singularities and additional features (dips). **Right:** Dependence of the observed features with respect to the moiré parameter λ_{g-g}. From Ref. 101.

1.3 Experimental techniques to form moirés of graphene

To be able to study the phenomena described in the previous section, the first step is to get experimental realizations of moirés of graphene that are energetically less favorable than untwisted graphene layers. We review here several experimental techniques that can be used to obtain moirés of graphene.

1.3.1 Graphene on graphite

The first observations of moirés of graphene were done in the early STM studies of graphite samples as shown in Fig. 1.23. At that time, it was seen as an 'anomalous superperiodicity' [47] and several explanations were proposed such as multiple-tip effects [3] or networks of dislocations [33]. It is now admitted that the observed superperiodicities are moiré patterns due to graphene flakes that are misaligned with the graphite substrate [79, 102]. While such stacking faults are routinely found, it is also possible to trigger them by tearing and folding the topmost flake of a graphite sample. This can be done by a scanning probe [32] or when cleaving the sample [11]. The angle between the layers is therefore determined by the angle of the fold.

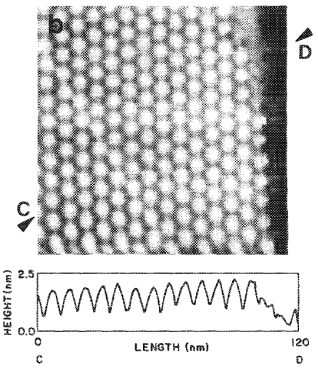

Figure 1.23: 100×100 nm^2 STM image of a graphite sample showing a moiré pattern. The bottom part is the tip height along the line from C to D. Ref. 47.

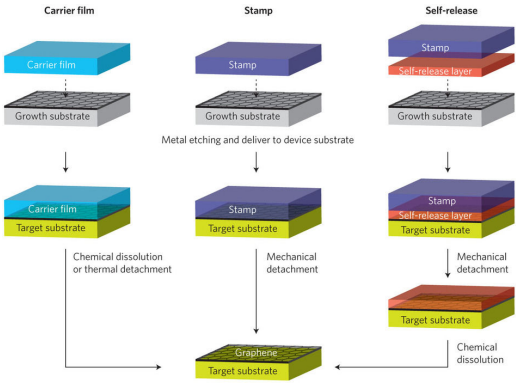

Figure 1.24: Techniques to transfer graphene from the growth substrate to the target substrate. From Ref. 18.

Later on, various studies [27, 51, 93] used the graphene on graphite system to easily get a decoupled graphene layer as the angle between the twisted layers is often large.

1.3.2 Transferring graphene on graphene

Graphene layers can be obtained by numerous fashions but not always on desired substrates. To solve this, techniques to transfer graphene layers from one substrate to another have been developed [24, 52]. Figure 1.24 shows different techniques to transfer graphene from the growth substrate to the target substrate. They consist mostly of the same process: the graphene layer is first transferred to a resist layer ('stamp' or 'carrier substrate') either by etching the growth substrate away or using a resist with stronger adherence. The layer can then can be transferred on another substrate by dissolving the resist or triggering the release of the layer by annealing. If the angle between the layer on the final substrate is controlled, it is possible to create moirés

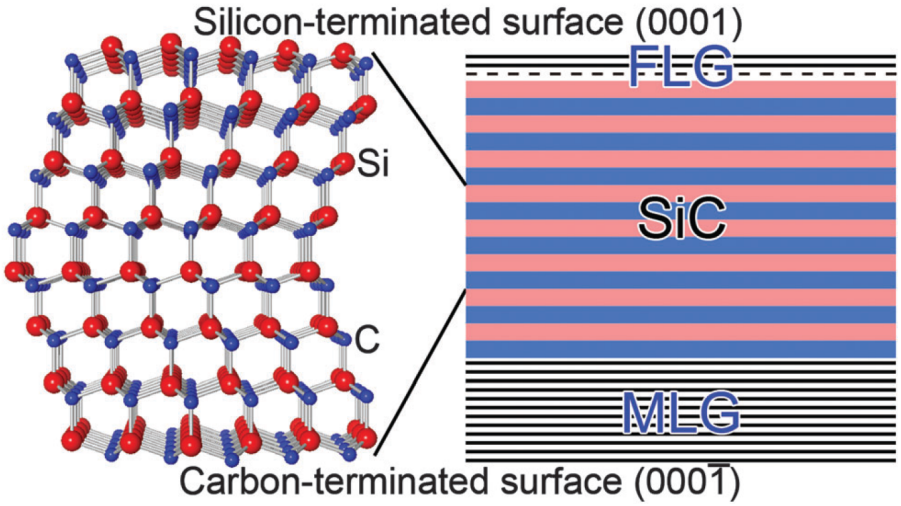

Figure 1.25: Crystal structure of 6H-SiC with silicon atoms in red and carbon atoms in blue showing the two inequivalent faces, Si and C faces. The right part shows a schematic of the SiC after the growth of few layers of graphene (FLG) on the Si-face and multilayer graphene (MLG) on the C-face. From Ref. 66.

of graphene of any desired angle by using a graphitic target substrate such as graphite or graphene on SiC. For example, the twisted graphene layers studied in Ref. 9 were realized by transferring a graphene layer grown by CVD on graphene on SiC.

The main drawback of this method is that it can deteriorate the transferred layer. The graphene layer is indeed exposed to solvents and resist during the transfer process that can leave residues. Such residues are hard to remove even with additional cleaning steps such as annealing.

1.3.3 Graphene on silicon carbide

Silicon carbide has long been known to dissociate by heating to form graphitic films [8, 95]. The dissociation leads to the sublimation of silicon and the remaining carbon atoms rearrange in graphene layers. As silicon carbide is a material that has inequivalent faces, the growth occurs differently on the two polar faces. Silicon carbide also displays many polytypes with 4H and 6H being the most used for graphene growth. The unit cell of the 6H (Fig. 1.25) shows a face terminated by silicon atoms (Si-face or SiC(0001) surface) and a face terminated by carbon atoms (C-face or SiC(000$\bar{1}$) surface). These inequivalent faces are also present in the 4H polytype and have

different implications on the graphene growth. Such differences were extensively studied in the review by Norimatsu and Kusunoki [46] and will be only briefly reviewed here.

On the silicon-terminated face (Si-face), the first carbon layer that is grown is strongly bound to the substrate satisfying most of the many dangling bonds remaining after the dissociation. As a consequence, it does not have the electronic band structure of graphene and is instead called the buffer layer. It indeed acts as an intermediate between the silicon carbide and the layers grown afterwards. The graphene layers grown on the top of this buffer layer are indeed preserved of any substrate-interaction except for n-type doping due to the surplus of electrons of the dangling bonds. The layers stack as in graphite with a AB or Bernal stacking meaning that the trademark linear dispersion of graphene is only obtained when a single graphene layer is grown on the top of the buffer layer. As a consequence, the electronic mobility of untreated films grown on SiC reaches only 1000 $cm^2V^{-1}s^{-1}$ [22] when 2×10^6 $cm^2V^{-1}s^{-1}$ has been achieved for suspended graphene layers [59].

On the carbon-terminated face (C-face), there is no such buffer layer as the growth occurs in a different fashion. The C-face is highly reactive so that nucleation happens at many different places. The growth is then much faster than on the Si-face and many more graphene layers are grown. While this could be viewed as a drawback, the fast growth implies that the layers stack with rotational disorder (also called turbostratic) instead of Bernal stacking. The appearance of out-of-plane ripples, that can be easily observed by Atomic Force Microscopy, stabilizes this unfavorable stacking. Twisted graphene layers with various twist angles are therefore easily formed but in an uncontrolled fashion. The electronic mobility of the graphene grown in this way is above 10 000 $cm^2V^{-1}s^{-1}$ [22].

1.3.4 Conclusion

Our aim is to realize STM studies of twisted graphene layers that require a clean surface. While the transferring of graphene layers seems the ideal technique to realize moirés of controlled twist angle, the residues left by the process are highly detrimental to STM studies. Out of the two remaining techniques, the growth of graphene on the carbon-face of silicon carbide seems the most promising one to routinely get twisted graphene layers with a large variety of twist angles. Moreover, the very high temperature needed for the growth allows to have clean surfaces due to efficient desorption. For these reasons, we chose this last technique for the realization of the samples in the presented work.

CHAPTER 2

EXPERIMENTAL METHODS

The Scanning Tunneling Microscope (STM) was developed in the nineteen eighties by G. Binnig and H. Rohrer [12]. It was a revolution in surface science as it gave access to the local properties of surfaces at sub-nanometer scales. It can indeed be used to image the sample surface as will be discussed in Section 1 or to measure the local electronic density of states of the sample as will be discussed in Section 2 of the present chapter. The third and fourth sections are devoted to the presentation of the experimental setups used to perform the low-temperature Scanning Tunneling Microscopy and Spectroscopy studies. The fifth section explains the process of growth of graphene on silicon carbide while the final section gives details on the softwares and methods used for the data analyses.

2.1 Scanning Tunneling Microscopy

2.1.1 Principle

A STM relies on quantum tunneling of electrons though an insulating gap (air or vacuum) between a metallic tip and the sample surface as shown in Fig. 2.1. If the rate of tunneling is sufficient, it is possible to detect a tunneling current I_t. To trigger enough tunneling events to measure a net tunneling current, an energy mismatch between the tip and the sample is introduced by applying a voltage bias V_b to the sample. At positive V_b, the electrons tunnel from the tip to unoccupied sample states while a negative V_b leads to tunneling of electrons from the occupied sample states to the tip. The tunneling occurs through the overlap of the electronic wave functions of

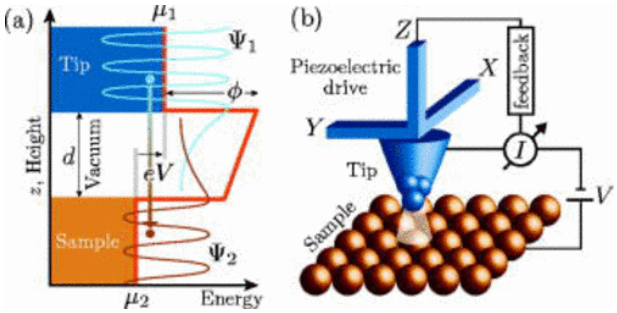

Figure 2.1: Principle of Scanning Tunneling Microscopy. Left: Energy diagram showing the overlap between the wavefunction of the tip ψ_1 and of the sample ψ_2 that leads to tunneling through the tunnel barrier of length d. **Right:** Schematics of a STM. By application of a bias V, a tunneling current I is detected by the tip. The position of the tip is controlled by piezoelectric motors. From Ref. 30.

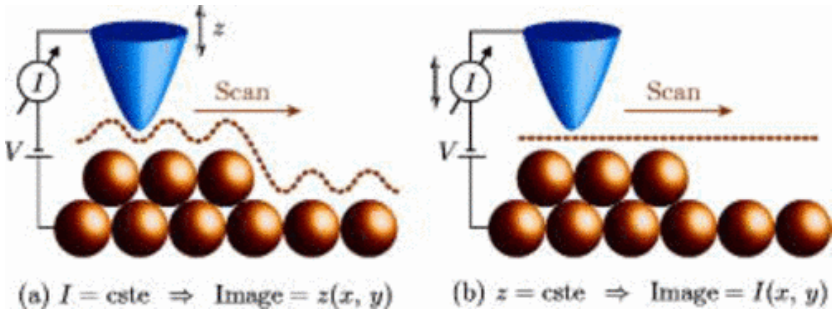

Figure 2.2: Left: Illustration of the constant-current imaging mode: the tip height follows the surface to keep a constant tunneling current. **Right:** Illustration of the constant-height imaging mode. Variations of the current are measured during a constant-height scan. From Ref. 30.

the sample and the STM tip. This requires a very small tip-sample distance (∼1 nm) controlled by piezoelectric motors as shown in the right part of Fig. 2.1.

2.1.2 Imaging mode

To realize a STM image, the tip scans the desired area in the x and y directions at a given V_b and I_t. There are two scanning modes: constant-height or constant-current as shown in Fig. 2.2. In constant-height mode, the tip height is kept constant and variations of the tunneling current I_t are recorded. As can be inferred, this technique requires very flat surfaces to

avoid collisions of the tip with protrusions or loss of the tunneling current. In consequence, the most widespread imaging mode is the constant-current mode. In this mode, the tip height is recorded and adjusted though a feedback loop to keep the tunneling current I_t constant during the scanning. All the STM images presented in this work were recorded in constant-current mode and therefore show the variations of the tip height Z.

2.1.3 *I(Z)* measurements

The tunnel character of the barrier can be probed by *I(Z)* measurements. The dependence of the tunneling current I_t with the tip-sample distance d is given by

$$I_t \propto e^{-2\kappa d} \tag{2.1}$$

with

$$\kappa = \sqrt{\frac{2m\phi}{\hbar^2}} \tag{2.2}$$

where m is the free electron mass, $\hbar$ the reduced Planck's constant and ϕ the work function of the tunneling system (or barrier height) that we simply define as the average of the work function of the surface ϕ_s and of the tip ϕ_t:

$$\phi = \frac{\phi_t + \phi_s}{2}\,. \tag{2.3}$$

Work functions are usually of the order of 5 eV leading to $\kappa \sim 1$ Å^{-1}. This shows that very small variations of the tip height leads to detectable changes of I_t, explaining the extremely high vertical resolution of the STM.

The *I(Z)* measurement consists in recording the tunneling current I_t while the tip is retracted from the surface. According to Eq. (2.1), the current decreases exponentially with respect to the tip-sample distance d and therefore with respect to the altitude Z of the tip. The slope of the linear decrease of the logarithm of the current is given by 2κ allowing to extract the value of the barrier height ϕ. The STM apparatus allows also to do *I(Z)* measurements on several points to probe any spatial variation of the barrier height.

2.2 Scanning Tunneling Spectroscopy

2.2.1 Principle

The large strength from the STM technique is the ability to get spatially-resolved informations on the local electronic density of states using Scanning Tunneling Spectroscopy (STS). To evidence this, one has to recall that the

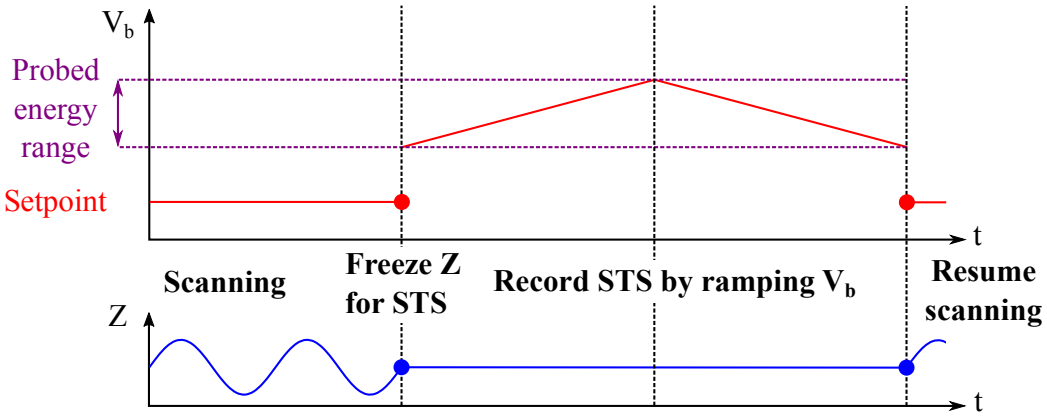

Figure 2.3: Bias V_b and tip height Z versus time during a STS measurement. The value V_b (red dot) sets the tip height Z before the STS (blue dot). The STS scans the probed energy range (in purple) by ramping V_b. This probed energy range is decoupled from the setpoint value.

tunneling current I_t is in fact the integration over energy of all the electronic tunneling events between the tip and the sample. The tunneling current is therefore linked to the electronic states of the tip and the sample:

$$I_t(V_b) \propto |M|^2 \int_{-\infty}^{\infty} N_s(E + eV_b) N_t(E) [f(E + eV_b) - f(E)] dE \tag{2.4}$$

where M is the tunneling probability assumed to be energy-independent, f the Fermi-Dirac distribution, N_s the density of states of the sample and N_t the density of states of the tip. Assuming a negligible effect of temperature ($k_B T << eV$), the Fermi-Dirac distributions become step functions so that the equation becomes

$$I_t(V_b) \propto |M|^2 \int_{E_F}^{E_F + eV_b} N_s(E + eV_b) N_t(E) dE \tag{2.5}$$

where E_F is the Fermi energy. Another common assumption made when using metallic tips is that the density of states of the tip is independent of energy in the energy range considered. The only energy-dependent term is therefore the density of states of the sample:

$$I_t(V_b) \propto \int_{E_F}^{E_F + eV_b} N_s(E + eV_b) dE \,. \tag{2.6}$$

The differentiation of the tunneling current with respect to the bias gives now

$$\frac{dI_t}{dV_b}(V_b) \propto N_s(E_F + eV_b) \,. \tag{2.7}$$

This equation is the basis of spectroscopy experiments as it shows that derivating the tunneling current with respect to the bias yields a quantity that is proportional to the density of states at the energy $E_F + eV_b$, directly tuned by the applied bias. Experimentally, this is done by applying a small AC modulation δV_b to the applied bias and detecting the resulting current modulation δI_t using phase-sensitive detection by a lock-in amplifier. Applying this technique to a given bias window yields the STS spectrum $dI_t/dV_b(V_b)$.

The procedure to record such a spectrum is shown in Fig. 2.3. A given setpoint (V_b,I_t) is chosen and sets the tip height. The feedback loop is switched off so that the tip altitude remains constant while the tunneling current I_t and its variations δI_t are recorded for each V_b in the chosen bias window. The resulting data is the $dI_t/dV_b(V_b)$ curve (usually shorted to dI/dV) proportional to the local density of states of the sample at $E_F + V_b$. We stress here that the choice of setpoint V_b is totally decoupled from the probed energy window. While the setpoint V_b is usually chosen as the first probed bias, the measurement can be performed with the setpoint V_b inside or outside the energy window as shown in the example in Fig. 2.3.

2.2.2 Spatially-resolved spectroscopies

The spatial resolution of STM can be combined with the spectroscopic measurements to get spatially-resolved measurements of the local density of states of the sample. A common measurement protocol using this is the Current-Imaging Tunneling Spectroscopy (CITS). In a CITS, the tip scans the surface at the setpoint (V_b,I_t) recording the topography while STS spectra are recorded in each point of the image. By picking STS spectra at particular locations, one can assess the difference between the density of states at these regions. Another representation mode of the CITS is the map of the differential conductance dI/dV at a given energy. These maps show the spatial variations of the density of states of the sample at this particular energy.

CITS are time-consuming measurements that can take several days to complete. Therefore, several techniques are used to reduce the necessary recording time. The first one consists in recording STM images with a higher resolution than the CITS by regularly spacing the points at which STS spectra are performed. This allows to get a sufficient spatial resolution for the STS without lowering the quality of the recorded STM images. The second technique consists in recording the topography and the STS spectra along a line and not on a full grid. Such line spectroscopies were used in Chapter 4 to probe the effect of the setpoint (V_b,I_t).

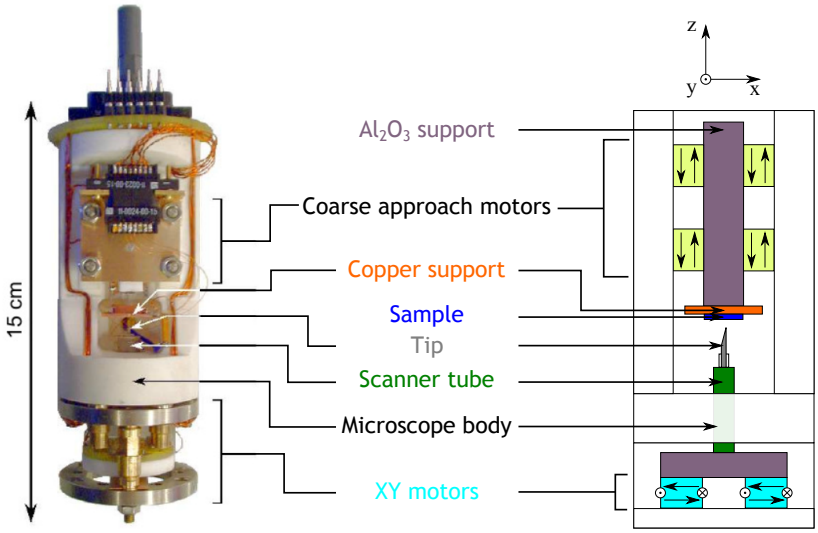

Figure 2.4: Photograph and colored schematics of the microscope head with the essential components pointed out. The moving Al_2O_3 supports are in purple and the fixed microscope body in white.

2.3 Experimental presentation of the microscope

2.3.1 STM head

A photograph and a colored schematic of our home-built Scanning Tunneling Microscope are presented in Fig. 2.4. The most essential part is the piezoelectric tube (in green in the scheme) on which the tip (in gray) is glued with silver paste. The electrodes of the tube are designed to allow scanning in the X,Y and Z directions. The tube can make images of a size of 30×30 μm at room temperature and 3×3 μm at low temperatures (50mK-4.2K) due to a loss of efficiency of the piezoelectric effect. To image places at greater distances, the scanner tube and the tip can be moved by using the XY motors (in cyan). These motors are piezoelectric legs that move the Al_2O_3 support, on which the tube is fixed, in the X and Y directions with respect to the microscope body (in white).

The sample (in blue) is glued by silver paste to a copper support (in orange) that is connected to the bias. A thermometer and a heater are also fixed to this copper support to control and monitor the sample temperature. The copper plate is fixed to another Al_2O_3 support that can move in the Z direction thanks to the same kind of piezoelectric legs (in yellow) to bring the sample in tunneling range.

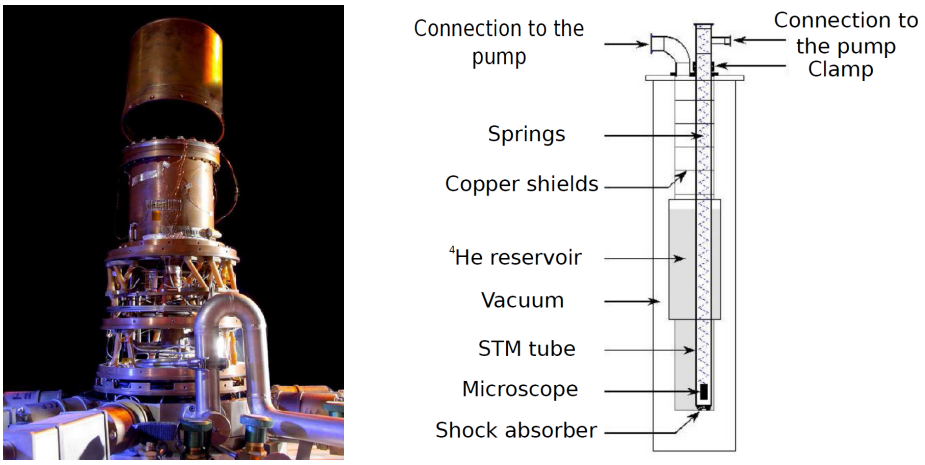

Figure 2.5: Left: Photograph of the Sionludi. **Right:** Scheme of the STM 4K, microscope included.

2.3.2 STM tip

The STM tips used in this work are commercial STM tips bought from Bruker [2]. They are mechanically cut in a wire with a diameter of 0.25 mm made of an alloy of platinum/iridium (Pt/Ir). These tips present several advantages. They are designed to have a very sharp tip apex adapted to STM measurements. The metallic alloy composing them is highly resistive to corrosion, preventing any oxide formation on the tip, and also quite stiff, reducing the risk of tip oscillations triggered by the feedback loop or external mechanical noise.

2.4 Cryogenic apparatuses

All the STM data shown in this work were recorded at low temperatures (< 10 K). To do this, the STM head can be embedded in two different cryogenic setups using liquid helium (He). Their working principle and loading procedures are presented here.

2.4.1 Inverted dilution fridge or Sionludi

The inverted dilution fridge uses standard wet dilution processes to reach an operating temperature of 50mK: a mixture of ^{3}He and ^{4}He circulates in a closed loop and is cooled by successive stages (100K, 10K, 4.2K, 1K and finally 50mK). The main difference with a standard dilution fridge lies in the fact that the cryostat is not plunged inside a liquid He dewar. Instead, the

4K cooling is provided by the circulation of liquid ^{4}He in the vacuum of the cryostat. This allows it to lay on a table with the coldest part on the top of the fridge, hence the name.

The loading procedure is as follows: the STM is first fixed to the highest stage (which is the coldest when the dilution is operating). Then, copper shields and a stainless steel cover are screwed respectively to prevent radiative losses and to enclose hermetically the cryostat. This space is then pumped to 10^{-6} mbar. After this pumping, the mixture is injected in a 'rapid' circulation path. This triggers a pre-cooling to 4.2K thanks to liquid ^{4}He coming from a He dewar situated below. Then, the injection of the mixture though the 'slow' circulation path triggers the expansion and condensation of the mixture allowing the STM to reach the base temperature of 50 mK.

The damping of external vibrations is done by a bellows on which the STM head is hanged. The whole Sionludi setup also lies on an air-cushioned table.

The data presented in Chapters 3 and 4 were recorded at 50mK by the STM operating in the Sionludi with the help of a Nanonis SPM controller manufactured by SPECS^{TM}.

2.4.2 ^{4}He cryostat or STM 4K

While the inverted dilution fridge allows to reach very low temperatures, it requires a lot of time to load the STM and reach the temperature of 50mK (a few days at best). The STM 4K, on the other hand, is a regular ^{4}He cryostat that allows to reach low temperatures (down to 1.4 K) within a single day. A schematic of the full setup is shown Fig. 2.5.

The STM head is loaded inside a tube embedded in the empty cryostat. The inside of the tube is pumped to 10^{-6} mbar at room temperature. Then, liquid ^{4}He is transferred into the cryostat to start the cooling. The pumping of the inside of the tube is stopped, the vacuum being maintained by the cryopumping on the cold walls of the tube. To lower the STM temperature, gaseous ^{4}He is introduced inside the tube to act as exchange gas between the cold ^{4}He bath and the STM. After usually one hour, the STM has reached the temperature of the ^{4}He bath: 4.2 K. Subsequently, it is possible to lower this temperature to around 1.4 K by pumping the ^{4}He bath.

The STM head inside the tube is hanged by a one meter-long spring to decouple it from external vibrations.

All the data presented in Chapter 5 were recorded by the STM 4K with the help of a Matrix SPM controller manufactured by Omicron NanoTechnology. The temperatures of the measurements range from 1.4 K to 10 K by heating of the STM.

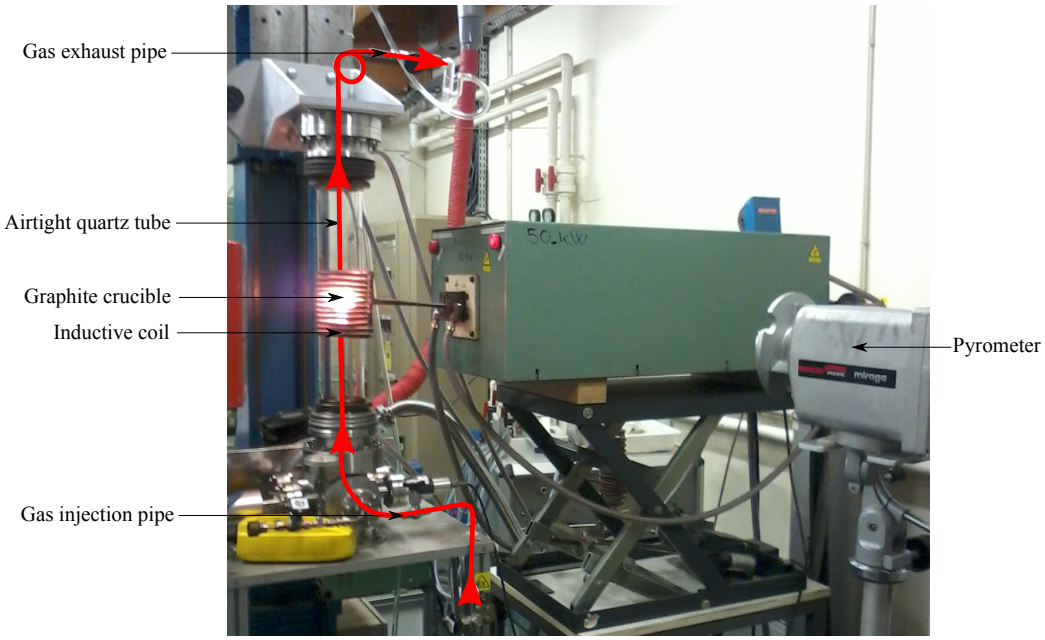

Figure 2.6: Induction furnace in function used for the graphene growth. The crucible is inside the transparent quartz tube and inductively heated by the field generated by the metallic coil. The gas circuit is shown in red.

2.5 Growth of graphene on silicon carbide

Silicon carbide wafers were purchased from Cree and cut by a diamond saw to have substrates of small dimensions. These substrates were then cleaned by acetone and isopropanol and dried under argon before growth. The graphene growth on the C-face was realized by annealing in a graphite crucible with an induction furnace shown in Fig. 2.6. A gas circuit allows to control the atmosphere inside the airtight quartz tube. The annealing of silicon carbide in the furnace can be realized under vacuum, argon (Ar) or a mixture of 90% argon and 10% hydrogen (Ar/H_2).

The recipe used to grow graphene samples is shown in Fig. 2.7 and is composed of four steps:

- The temperature is first raised to 900°C and stays at this value during 18 min under vacuum to clean the sample by removing adsorbates
- Then the temperature is set to 1600°C during 30 min under an atmosphere of Ar/H_2. This step etches the silicon carbide substrate to remove polishing scratches and get flat terraces that are around 5 μm wide.

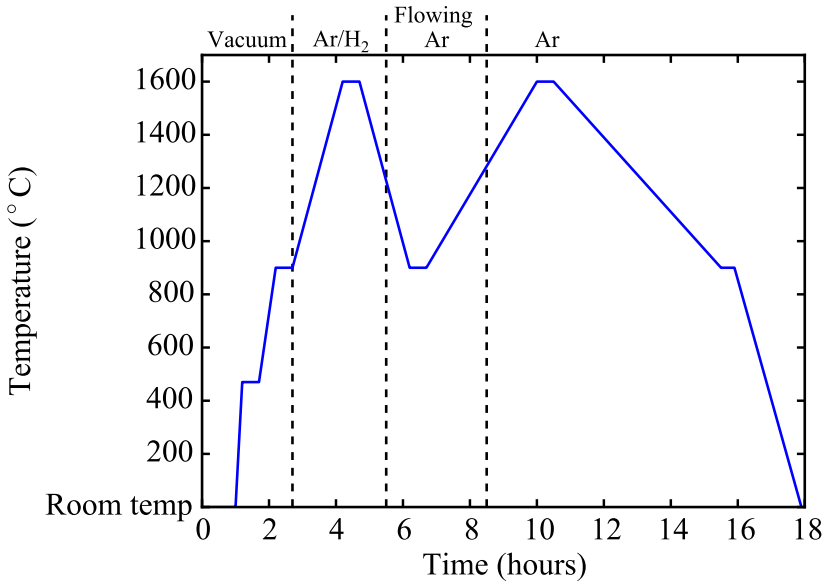

Figure 2.7: Temperature profile and gases used for the growth of the samples presented in Chap. 3 and 4.

- The temperature is lowered to 900°C with argon flowing though the tube to flush any remaining hydrogen. The plateau step lasts 30 min
- To finally grow the graphene, the flow of argon is stopped and the sample is kept under about 1 atm of argon. Then, the temperature is raised to 1600°C to start the graphitization. The temperature plateau duration can be tuned but is usually between 20 and 30 min. Then, the temperature is slowly decreased to room temperature.

The presented process follows the work of Ref. 45 and was used to grow the samples presented in Chapters 3 and 4. Another growth process under vacuum was used for the samples in Chapter 5 and will be presented there.

2.6 Data analysis softwares

2.6.1 Gwyddion

The STM images presented in this work are analysed with Gwyddion [64]. The post-treatment of the images consists in a mean plane subtraction and an eventual line matching to smooth images. A Fourier transform filtering was sometimes applied to remove noise at a particular frequency (50 Hz for

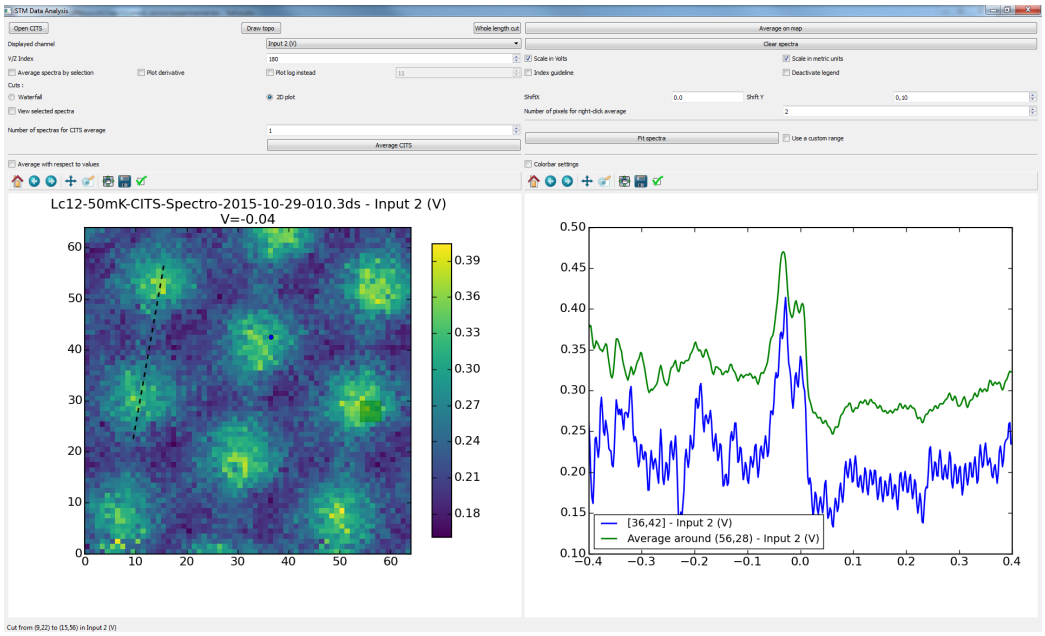

Figure 2.8: Graphical User Interface of *STM Data Analysis* with a CITS loaded. The left part is the dI/dV map and the right part shows the picked spectra.

example). After these steps, the minimal tip height was substracted from the data to get the relative tip height Z.

Gwyddion was also employed to get the Fourier transforms used for commensurability analyses. The method computes the modulus of the Fourier coefficients with Hann windowing to attenuate edge effects.

2.6.2 *STM Data Analysis*

To analyse the CITS, line spectroscopies and I(z) maps shown in the thesis, I have developed a data analysis software named *STM Data Analysis*. This software is written in Python ($\sim$ 1300 lines of code) using various libraries: PyQt for the Graphical User Interface, NumPy/SciPy for the scientific data manipulations and matplotlib for the data plotting [40]. More generally, the majority of the presented figures were generated by Python programs using the same libraries.

The use of different STM controllers led to the recording of data files that have different formats. As a consequence, the reading and analysis of these variously-formatted data required the use of different data analysis softwares. This state of things prompted the development of the *STM Data Analysis*

software. The aim was to to centralize in a single software the reading of STS data from different sources and the features that are helpful to analyze STS data such as picking spectra in a CITS, averaging spectra, switching from dI/dV spectra to I(V) spectra, etc. For an efficient visualization of the data, the Qt library allows to do these tasks dynamically thanks to a Graphical User Interface shown in Fig 2.8.

2.6.3 Commensurability analyses

The mesh decomposition part of the commensurability analyses presented in this work were done thanks to the vector graphics software Inkscape [1]. The extraction of the structural parameters (lattice parameters, strains, angles) from the commensurability indices is done by a program written by Alexandre Artaud that implements the calculations of the Supplementary Information of Ref. 6.

CHAPTER 3

EFFECT OF RELATIVE STRAIN ON MOIRÉ VAN HOVE SINGULARITIES

3.1 Introduction

The interplay (both for large and small angles) of strain with the moiré van Hove singularities has been the subject of very few studies. In this section, we firstly present a geometric approach to the effect of strain on the moiré van Hove singularities and confront it with the existing theoretical studies. We notably introduce the situation where a difference of strain is present in the layers. Never considered in the literature, such a situation was evidenced in our STM study of twisted graphene layers with a twist angle of $\theta = 1.26°$ in the second part.

3.2 Theoretical considerations

3.2.1 Geometric approach of uniaxial strain

As discussed in Chapter 1, the wavevector ΔK that separate the Dirac points of the two twisted layers is the parameter that dictates the energy of the van Hove singularities. The application of strain to the twisted graphene layers will displace their Dirac cones and thus change ΔK. If the strain is not isotropic, the three-fold degeneracy of ΔK is lifted meaning that several values are possible. The presented geometric approach estimates the changes in energy of the van Hove singularities by supposing that these energies are only impacted by the change in ΔK by strain.

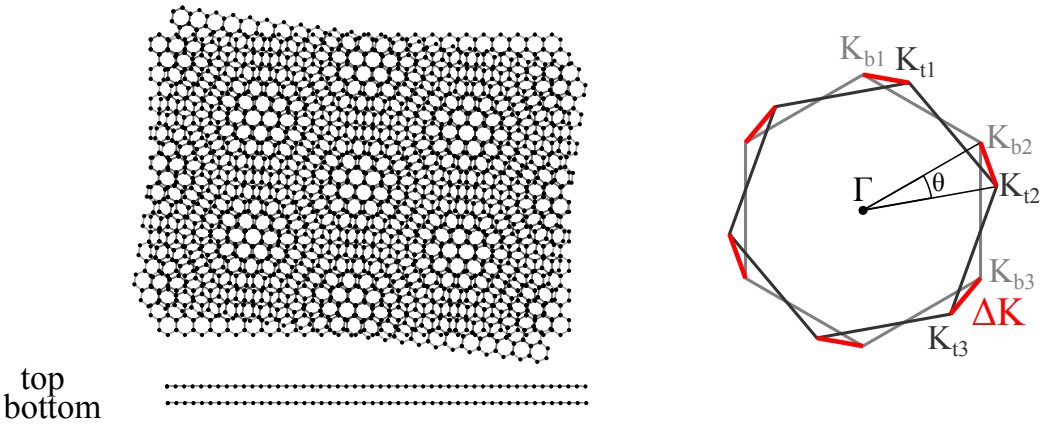

Figure 3.1: Left: Moiré pattern formed by two unstrained twisted graphene layers. **Right:** Brillouin zones of the layers (top layer in dark grey, bottom layer in light grey) with single-valued ΔK in red

3.2.1.a Principle

Taking a simple system of unstrained stacked graphene layers with a twist angle θ between them, their lattice vectors are ($\mathbf{a_{b_1}}$,$\mathbf{a_{b_2}}$) for the bottom layer and ($\mathbf{a_{t_1}}$,$\mathbf{a_{t_2}}$) for the top layer. From these, the reciprocal vectors of both layers ($\mathbf{G_{b_1}}$,$\mathbf{G_{b_2}}$) and ($\mathbf{G_{t_1}}$,$\mathbf{G_{t_2}}$) can de deduced. Consequently, we get the position of the K points for both layers $\mathbf{K_{t_1}}$ and $\mathbf{K_{b_1}}$:

$$\mathbf{K_{t_1}} = \frac{\mathbf{G_{t_1}}}{3} + \frac{\mathbf{G_{t_2}}}{3} \tag{3.1}$$

$$\mathbf{K_{b_1}} = \frac{\mathbf{G_{b_1}}}{3} + \frac{\mathbf{G_{b_2}}}{3} \tag{3.2}$$

and of the K' points $\mathbf{K_{t_2}}$ and $\mathbf{K_{b_2}}$:

$$\mathbf{K_{t_2}} = \frac{\mathbf{G_{t_1}}}{3} - \frac{\mathbf{G_{t_2}}}{3} \tag{3.3}$$

$$\mathbf{K_{b_2}} = \frac{\mathbf{G_{b_1}}}{3} - \frac{\mathbf{G_{b_2}}}{3}\,. \tag{3.4}$$

The vectors $\mathbf{K_{t_3}}$ and $\mathbf{K_{b_3}}$ are given by

$$\mathbf{K_{t_3}} = \mathbf{K_{t_1}} - \mathbf{K_{t_2}} \tag{3.5}$$

$$\mathbf{K_{b_3}} = \mathbf{K_{b_1}} - \mathbf{K_{b_2}}\,. \tag{3.6}$$

ΔK then simply falls as $\Delta K = |\mathbf{K_{t_1}} - \mathbf{K_{b_1}}|$ that is equal to $|\mathbf{K_{t_2}} - \mathbf{K_{b_2}}|$ and $|\mathbf{K_{t_3}} - \mathbf{K_{b_3}}|$ for unstrained layers. This is the situation depicted in Fig. 3.1.

To evaluate the effect of application of a uniaxial strain of magnitude σ along an angle ϕ_s on the ΔK, we model it by the matrix

$$M_{str} = I_2 + \sigma \begin{pmatrix} \cos^2\phi_s - \gamma \sin^2\phi_s & (1+\gamma)\cos\phi_s \sin\phi_s \\ (1+\gamma)\cos\phi_s \sin\phi_s & \sin^2\phi_s - \gamma\cos^2\phi_s \end{pmatrix} \tag{3.7}$$

where γ is the Poisson ratio set to 0.165 [14]. This matrix is the result of an uniaxial strain of magnitude σ along ϕ_s transposed in the basis of the layers. The angle ϕ_s is given with respect to the first crystallographic direction of the bottom layer $\mathbf{a_{b_1}}$. We can then express the strained lattice vectors of the bottom layer noted $(\overline{\mathbf{a_{b_1}}}, \overline{\mathbf{a_{b_2}}})$ by

$$\overline{\mathbf{a_{b_1}}} = M_{str}\mathbf{a_{b_1}} \tag{3.8}$$
$$\overline{\mathbf{a_{b_2}}} = M_{str}\mathbf{a_{b_2}} \tag{3.9}$$

and the same for the top layer by

$$\overline{\mathbf{a_{t_1}}} = M_{str}\mathbf{a_{t_1}} \tag{3.10}$$
$$\overline{\mathbf{a_{t_2}}} = M_{str}\mathbf{a_{t_2}}. \tag{3.11}$$

Note that, as the uniaxial strain breaks the symmetry of the lattice, we have in general $|\overline{\mathbf{a_{b_1}}}| \neq |\overline{\mathbf{a_{b_2}}}|$. In any case, the reciprocal vectors of the strained lattice can be derived and in consequence the positions of the K_t and K_b points. So we can express the strained case value $\overline{\Delta K}_i$ for the three directions $i = 1, 2, 3$ and in the two following cases.

3.2.1.b Strain in the two layers (Absolute strain)

The effect of the application of strain in both layers is shown in Fig. 3.2. Despite the important deformation of 10%, the moiré pattern does not change drastically. In fact, applying the same strain in both layers leaves the commensurate indices of the moiré unchanged. Consequently, the Park-Madden matrix linking the atomic positions of the the top and bottom layers stays the same. Nevertheless, $\overline{\Delta K}$ (strained case) will be different from ΔK (unstrained case) because the two layers are differently orientated with respect to the direction of the uniaxial applied strain. Uniaxial strain also breaks the lattice symmetry so that we have three possible values of $\overline{\Delta K}$

$$\overline{\Delta K_i}^A = |\overline{\mathbf{K_{t_i}}} - \overline{\mathbf{K_{b_i}}}| \text{ for } i = 1, 2, 3 \tag{3.12}$$

which are shown in different shades of blue in Fig. 3.2 and can be evaluated analytically.

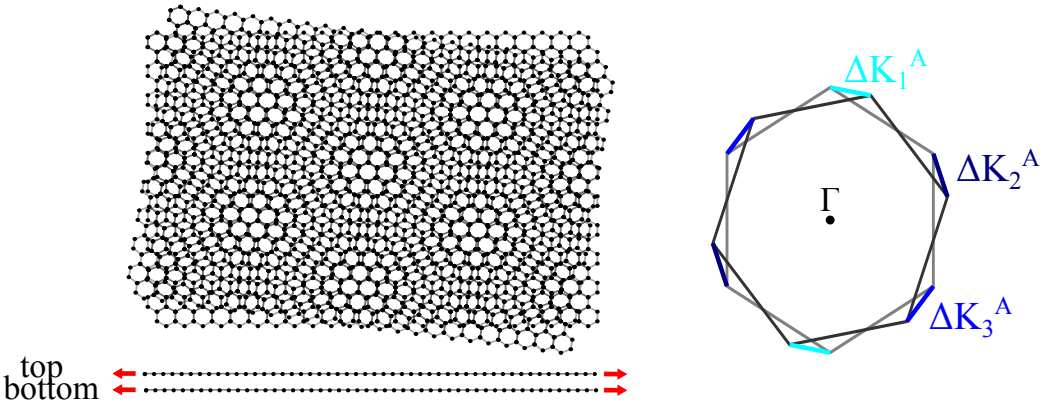

Figure 3.2: Left: Moiré pattern formed by two strained twisted graphene layers. The deformation is applied along the horizontal direction and has a magnitude of 10%. **Right:** Brillouin zones of the layers (top layer in dark grey, bottom layer in light grey) with three values of ΔK in different shades of blue.

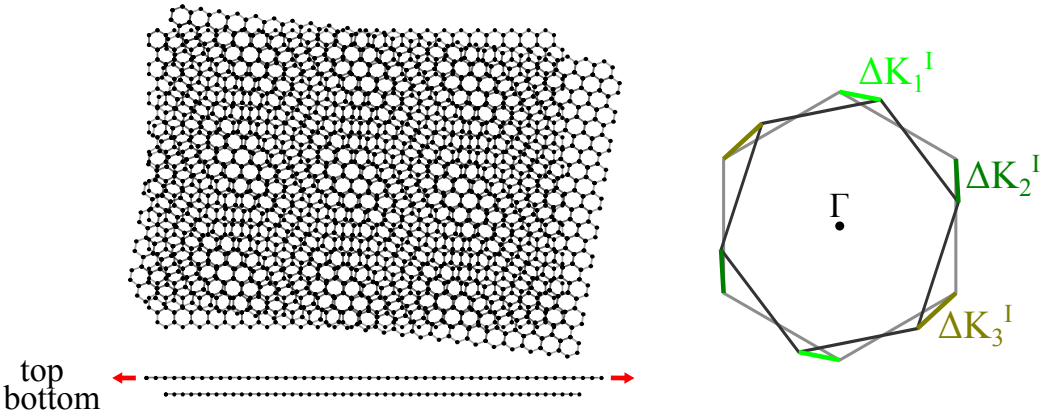

Figure 3.3: Left: Moiré pattern formed by twisted graphene layers with only one strained layer. The deformation is applied along the horizontal direction and has a magnitude of 10%. **Right:** Brillouin zones of the layers (top layer in dark grey, bottom layer in light grey) with three values of ΔK in different shades of green.

3.2.1.c Strain in only one layer (Relative strain)

Figure 3.3 shows that applying the 10% deformation in only one layer has a visible deformation effect on the moiré. This is because the relative atomic positions between the layers change far more than in the absolute strain case. Also, in the case of relative strain, the commensurability indices are changed meaning that the moiré periodicity changes as well. The analytic formula for $\overline{\Delta K}^I$ can be derived similarly to the previous case

$$\overline{\Delta K_i}^I = |\overline{\mathbf{K_{t_i}}} - \mathbf{K_{b_i}}| \text{ for } i = 1, 2, 3. \tag{3.13}$$

These $\overline{\Delta K_i}^I$ are shown in different shades of green in Fig. 3.3 and appear more strongly modulated by strain compared to the absolute strain case.

3.2.1.d Energy of the van Hove singularities

We recall that in the unstrained case we can evaluate the energy of the singularities with respect to the energy of the Dirac point by

$$E_{vHs} - E_D = \frac{\Delta E_{vHs}}{2} = \hbar v_F \frac{\Delta K}{2} - t_\theta \tag{3.14}$$

using the continuum formula of Eq. 1.45. In the following, we make the assumption that the change in energies of the singularities induced by strain is only due to the change of ΔK. We then evaluate for the three cases $i = 1, 2, 3$ the energy of the singularities by

$$\overline{E_{vHs_i}} - E_D = \frac{\Delta E_{vHs}}{2} = \hbar v_F \frac{\overline{\Delta K_i}}{2} - t_\theta \,. \tag{3.15}$$

3.2.1.e Results

For a given structure (meaning a given twist angle θ), we first compare the effects of absolute and relative strain at constant strain magnitude σ.

For the unstrained bilayer defined by the indices (3,4) ($\theta = 9.43°$), there is only one singularity at positive energy (the other singularity being at opposite energy), given by the continuum formula in Eq. (3.14): $E_{vHs} - E_D = 905$ meV with $t_\theta = 0.108$ eV. However, Fig. 3.4 shows that it is no longer the case for the strained cases. As the uniaxial strain has different effects depending on the direction considered, three values of $\overline{\Delta K}$ are possible with saddle points and thus van Hove singularities at different energies. We then have three singularities instead of only one. Only at particular values of ϕ_s, a crossing of energy of two van Hove singularities occurs which leaves only

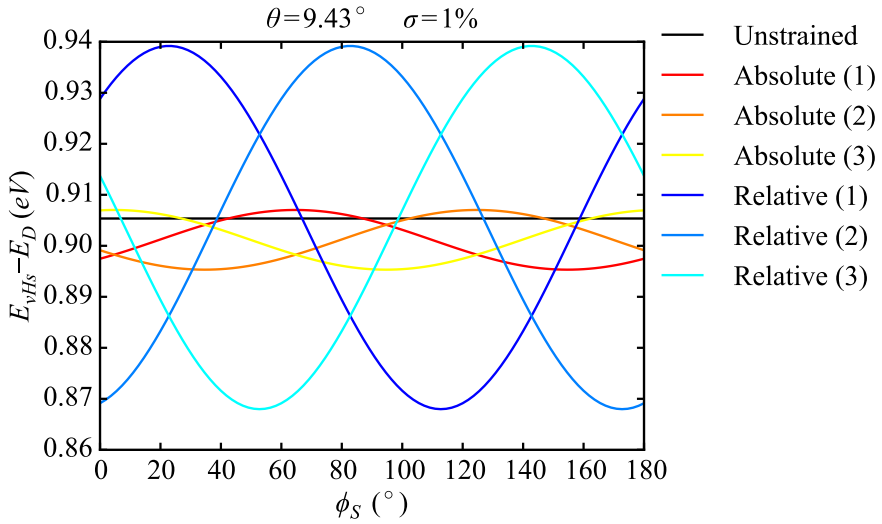

Figure 3.4: Energy of the van Hove singularities as a function of the strain angle ϕ_s for the three directions with $\theta = 9.43°$ and $\sigma = 1\%$ in the case of strain in the two layers (absolute) and in only one layer (relative). The black line is the constant energy of the van Hove singularity for the unstrained case.

two distinct singularities. The case where only one layer is strained (blue curves) gives stronger variations of energy with respect to the strain angle ϕ_s than the case where both layers are strained (red, orange and yellow curves). As inferred previously, straining only one layer changes more effectively the relative atomic positions of layers than straining them both which explains this observation. We also note that, as the directions are equivalent through a rotation of 60°, the variation of energy follows the same symmetry.

In order to see the influence of the twist angle θ, we did the same evaluation for $\theta = 3°$ that is shown Fig. 3.5 with van Hove singularities closer to the Dirac point. It is clear that the absolute strain is even less effective in changing the energies of the singularities than in the case $\theta = 9.43°$ because the crystallographic orientations of the layers become closer as the angle θ diminishes. This means that straining both layers becomes less effective in changing the relative atomic positions compared to individually straining one layer.

For $\theta = 1.26°$ (shown Fig. 3.6), the effect of absolute strain is almost null compared to the effect of relative strain. For certain values of ϕ_s, this relative strain even brings the van Hove singularities to the Dirac point ($E_{vHs} - E_D = 0$). This last consideration has to be taken with care as the continuum formula was applied outside of its validity domain. The small twist angles

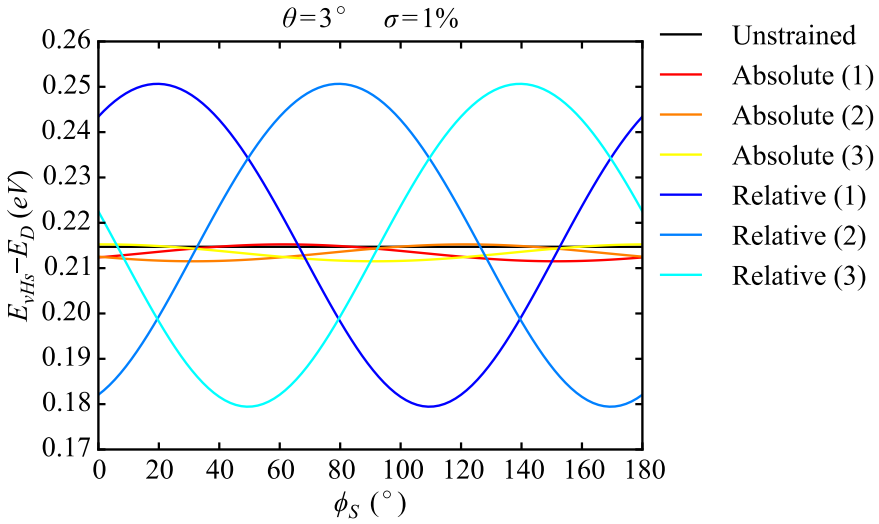

Figure 3.5: Energy of the van Hove singularities as a function of the strain angle ϕ_s for the three directions with $\theta = 3°$ and $\sigma = 1\%$ in the case of strain in the two layers (Absolute) and in only one layer (Relative). The black line is the constant energy of the van Hove singularity for the unstrained case.

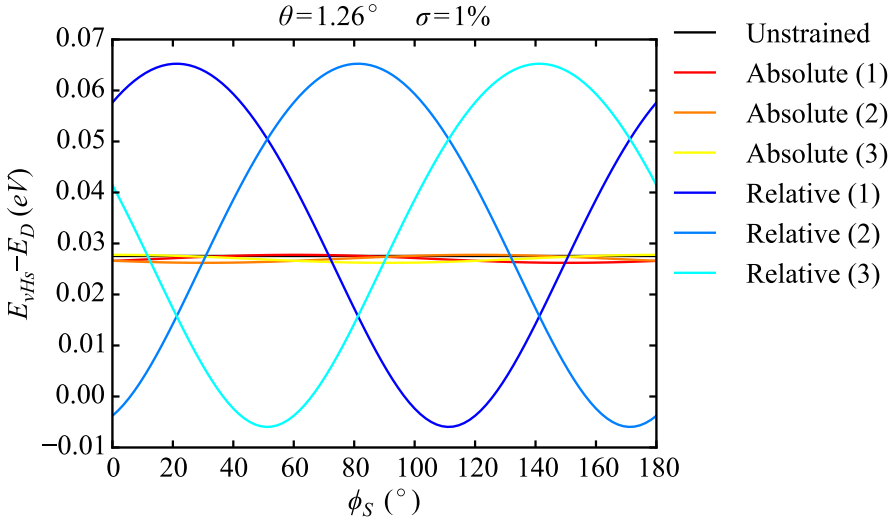

Figure 3.6: Energy of the van Hove singularities as a function of the strain angle ϕ_s for the three directions with $\theta = 1.26°$ and $\sigma = 1\%$ in the case of strain in the two layers (Absolute) and in only one layer (Relative). The black line is the constant energy of the van Hove singularity for the unstrained case.

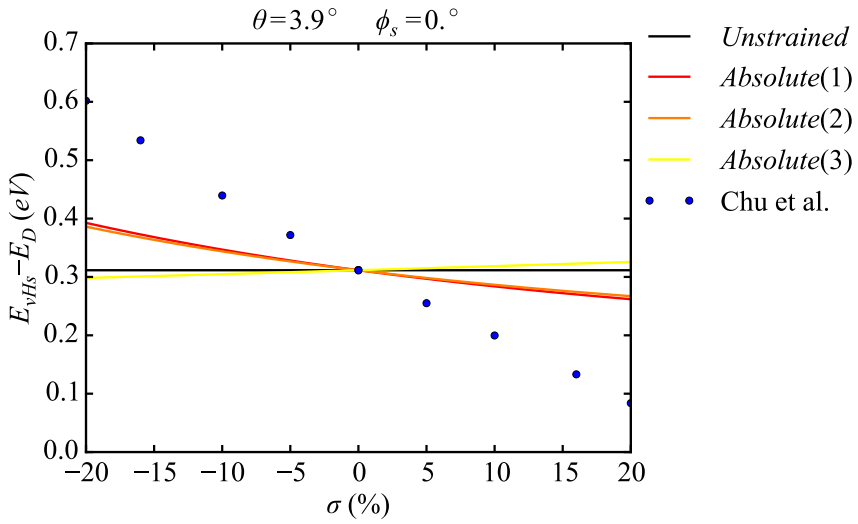

Figure 3.7: Energy of the van Hove singularities as a function of strain amplitude σ for the three directions estimated for $\theta = 3.9°$ and $\phi_s = 0°$ in the case of strain in the two layers (Absolute). The black line is the constant energy of the van Hove singularity for the unstrained case. The blue points are results of the tight-binding calculations of Chu *et al.*[19]

regime is indeed more complex than what can be deduced from this simple geometric approach.

3.2.2 Tight-binding calculations

Tight-binding calculations offers a more accurate method to estimate strain effects and can tackle both small and large angle structures. However, the calculations need to be made on a periodic cell which leaves relative strain difficult to study as it changes the periodicity of the moiré cell. The studies in the literature were therefore made by applying absolute strain to the layers which preserved the periodicity of the moiré cell and will be reviewed now.

3.2.2.a Energy modulation of the van Hove singularities by strain

Chu *et al.* [19] studied the strain applied to the zigzag direction of the first layer ($\phi_s = 0$). They therefore used the following strain matrix

$$M_{Chu} = M_{str}(\phi_s = 0) = I_2 + \sigma \begin{pmatrix} 1 & 0 \\ 0 & -\gamma \end{pmatrix} \tag{3.16}$$

applied to a system of unstrained graphene layers with a twist angle θ. The band structure of the subsequent structure was calculated by tight-binding.

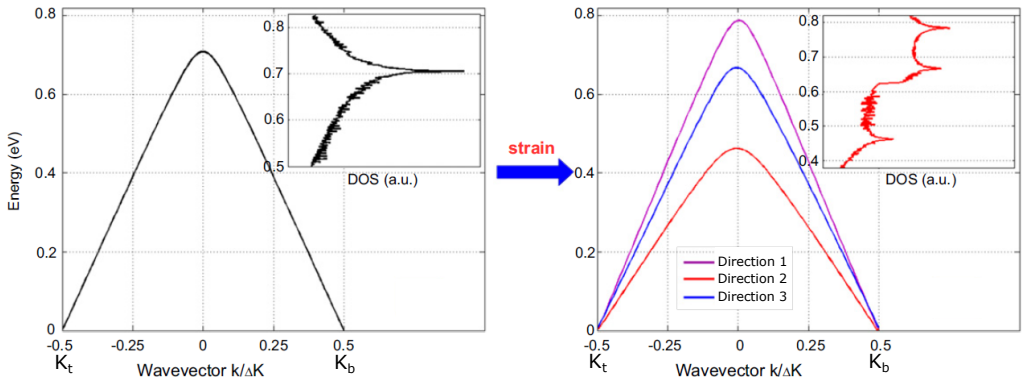

Figure 3.8: Band structure at positive energies (density of states in inset) for $\theta = 9.43°$, calculated by tight-binding without strain (left) and with strain ($\sigma = 6\%$ and $\phi_{ND} = 20°$) (right). The uniaxial strain lifts the degeneracy of the saddle points with respect to direction giving rise to three van Hove singularities. Adapted from [65]

The authors specifically assumed 'that the lattice deformation [...] does not lift the degeneracy of the Dirac points' at odds with the geometrical approach above. The strained system shows therefore only one van Hove singularity for each polarity whose energy changes with strain as derived from their tight-binding calculations. Fig. 3.7 condenses their results for $\theta = 3.9°$ showing that the energy of the van Hove singularities is reduced when applying tensile strain ($\sigma > 0$) while it augments when applying compressive strain ($\sigma < 0$). This trend is well reproduced by the geometric approach along the direction 1 and 2 (red and orange lines in Fig. 3.7) even if the magnitudes do not match. The difference between the tight-binding calculations and the geometric approach grows with the strain magnitude as this latter approach is only valid for small strains.

3.2.2.b Lift of degeneracy of the van Hove singularities by strain

Similarly to Chu *et al.*, Nguyen and Dollfus [65] also performed tight-binding calculations on twisted graphene layers deformed by the application of a strain matrix to both layers. As they did not consider a single direction but all values of ϕ_s, the strain matrix used was kept in its general form

$$M_{ND} = I_2 + \sigma \begin{pmatrix} \cos^2\phi_{ND} - \gamma \sin^2\phi_{ND} & (1+\gamma)\cos\phi_{ND}\sin\phi_{ND} \\ (1+\gamma)\cos\phi_{ND}\sin\phi_{ND} & \sin^2\phi_{ND} - \gamma\cos^2\phi_{ND} \end{pmatrix} \quad (3.17)$$

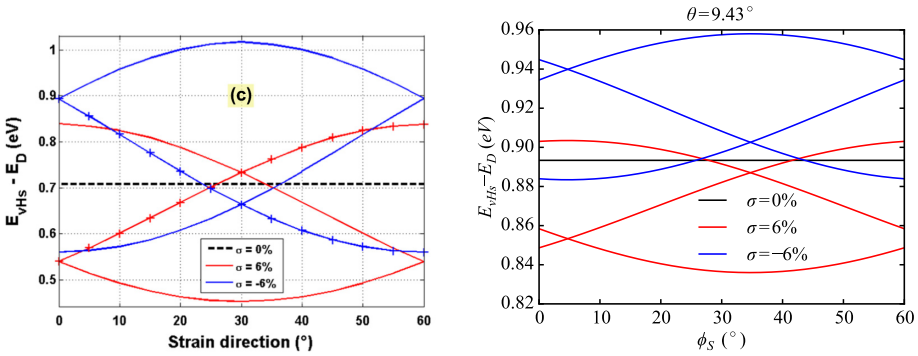

Figure 3.9: Energy of the van Hove singularities calculated by tight-binding (left) in [65] and estimated from the geometric approach (right) for $\theta = 9.43°$. The strain angle shift of $\theta/2$ between the two data sets comes from a different definition of ϕ_s (see text).

where ϕ_{ND} is linked to ϕ_s though $\phi_{ND} = \phi_s + \frac{\theta}{2}$ due to a different definition of the strain angle. Another difference with Chu *et al.* is that they implicitly did not make the hypothesis that the Dirac points stay degenerate. Their results are consequently in agreement with the geometric approach as the lift of degeneracy make six van Hove singularities (three for each polarity of the energy with respect to the Dirac point) appear in the strained case. The band structure and the density of states are compared for the unstrained and strained case in Fig. 3.8 showing indeed that the saddle points occur at different energies for each direction giving rise to three van Hove singularities. The effect of the strain angle ϕ_{ND} on the energy of these three van Hove singularities was also studied. Figure 3.9 shows the energy of the van Hove singularities as a function of the strain angle ϕ_{ND} for the same twist angle ($\theta = 9.43°$) and for the strain magnitudes $\sigma = 0, 6$ and -6%. The energy of the van Hove singularities is modulated with respect to ϕ_{ND} with a crossing of two singularities for $\phi_{ND} = 30°$. The comparison with the geometric approach for the same parameters (right of Fig. 3.9) is again favorable in terms of the trends but not in magnitude. This underestimation of energies shows that the strain effect on van Hove singularities is not only governed by the change in ΔK but by additional phenomena, not taken into account by design in the geometric approach. These effects are probably linked to non-trivial modifications of the electronic band structures such as strain-driven variations of Fermi velocity [23].

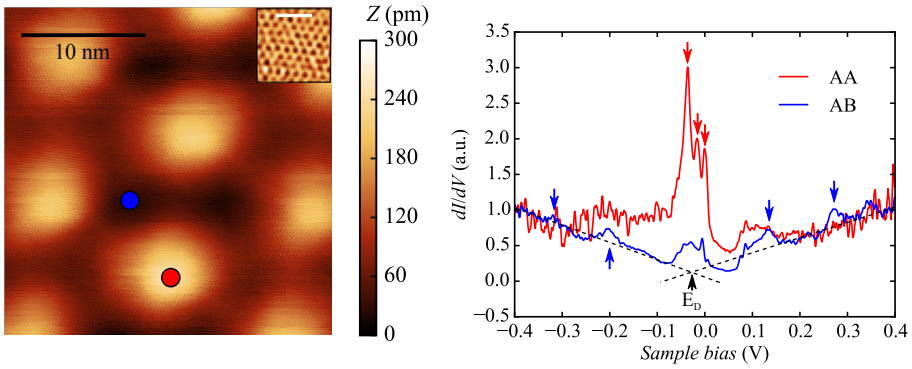

Figure 3.10: Left: 26.4×26.4 nm^2 STM topograph of twisted graphene layers showing the moiré pattern ($V_b = -400$ mV, $I_t = 50$ pA). The twist angle between the graphene layers was estimated to be θ=1.26°. Inset : Zoom on the image showing the honeycomb lattice of the carbon atoms in the top layer. The scale bar is 1 nm. **Right:** dI/dV(V) spectra recorded by STS at the spots marked with colored dots in Fig. 3.10a (red and blue dots for AA and AB regions respectively) showing multiple peaks in AA regions (red arrows) and well resolved peaks at higher energy in AB regions (blue arrows) ($V_b = -400$ mV, $I_t = 300$ pA). The energy of the Dirac point $E_D = -25$ mV (black arrow) was deduced from the V-shape of the density of states at high energies.

3.3 Relative strain in twisted graphene layers ($\theta = 1.26°$)

The previous section showed that the energy and the number of van Hove singularities are modulated by absolute strain but also more effectively by relative strain. The following section gives the first experimental observation of a strain-driven modulation of the van Hove singularities which is traced back to the electronic band structure.

3.3.1 STM/STS results

Figure 3.10a shows a constant-current STM image of a moiré composed of twisted graphene layers grown on SiC. The angle between the layers can be estimated from the moiré periodicity D_m using

$$\theta = \arcsin\left(\frac{a_{gr}}{2D_m}\right) \tag{3.18}$$

with a_{gr} the lattice parameter of graphene [76]. The angle between the layers is very small as this gives here $\theta = 1.26° \pm 0.08$. Figure 3.10b shows typical STS measurements performed in AA and AB regions. The most striking feature is the presence of a group of resonances located near zero energy and strongly localized in AA regions. The V shape of the density of states at high energy (dashed line) allows to conclude that this group of states is in fact centered around $E = -25$ meV which corresponds to the typical doping of graphene grown on the carbon-face of SiC. [85] Additional peaks are seen at higher energies and are found to be more pronounced in AB regions.

We interpret the three observed peaks as the effect of uniaxial relative strain in the layers on the moiré van Hove singularities. To evalulate this strain, we performed a commensurability analysis of the twisted graphene layers as described in Chapter 1.

3.3.2 Commensurability analysis

The Fourier transform of the STM topograph of the moiré pattern with atomic resolution is shown Fig. 3.11. As discussed in Chapter 1, the STM image is sensitive to the beating that is the alternation of bright regions. The spots at the center of the Fourier transform (top right of Fig. 3.11) correspond therefore to the beating reciprocal vectors ($\mathbf{k_{beat_1}}, \mathbf{k_{beat_2}}$) that are used to decompose the Fourier transform (black mesh in Fig. 3.11). In the presented case, the graphene reciprocal vectors cannot be decomposed in integer coordinates in the mesh of the beating reciprocal vectors. This indicates that the beating does not match the true periodicity of the moiré, a situation unveiled in Section 1.2.2. In direct space, the moiré period is then larger than the distance between two bright spots (beating) so that the moiré reciprocal vectors are smaller than the beating reciprocal vectors. To find the moiré periodicity, a closer inspection of the graphene spots in the bottom right of Fig 3.11 is needed. The graphene spots are at one third of the mesh of the beating reciprocal vectors which means that the moiré reciprocal vectors are three times smaller than the beating reciprocal vectors. Therefore, in direct space, the moiré system spans three inequivalent beatings in each direction. By defining $\mathbf{k_{m_1}} = \frac{1}{3}\mathbf{k_{beat_1}} = \frac{1}{3}(\mathbf{k_{t_1}} - \mathbf{k_{b_1}})$ and

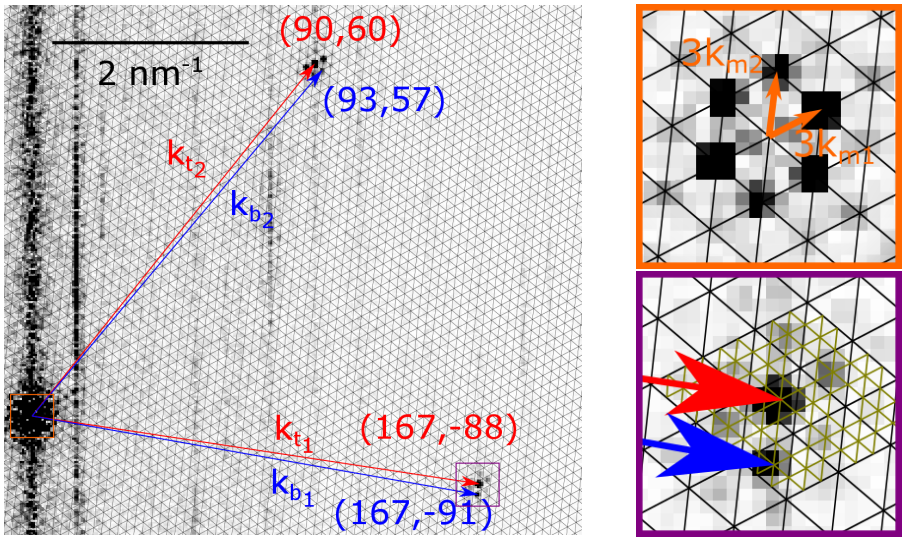

Figure 3.11: Left: Fourier transform of the STM topograph of the moiré pattern with atomic resolution. The black mesh decomposes the FT in the basis of the beating reciprocal vectors (see text). The numbers are the coordinates of the graphene reciprocal vectors in the basis of the moiré reciprocal vectors. **Top right:** Center of the Fourier transform (orange square) with enhanced contrast to see the decomposing vectors of the mesh which are the beating reciprocal vectors $(\mathbf{k_{beat_1}}, \mathbf{k_{beat_2}}) = (3\mathbf{k_{m_1}}, 3\mathbf{k_{m_2}})$. **Bottom right:** Zoom on the graphene spots situated in the bottom right regions (purple square). The spots do not fall on the black beating mesh but instead on the green moiré mesh that is three times smaller.

$\mathbf{k_{m_2}} = \frac{1}{3}\mathbf{k_{beat_2}} = \frac{1}{3}(\mathbf{k_{t_2}} - \mathbf{k_{b_2}})$, the commensurate structure is defined by

$$\mathbf{k_{t_1}} = 167\mathbf{k_{m_1}} - 88\mathbf{k_{m_1}} \tag{3.19}$$
$$\mathbf{k_{t_2}} = 90\mathbf{k_{m_1}} + 60\mathbf{k_{m_2}} \tag{3.20}$$
$$\mathbf{k_{b_1}} = 167\mathbf{k_{m_1}} - 91\mathbf{k_{m_2}} \tag{3.21}$$
$$\mathbf{k_{b_2}} = 93\mathbf{k_{m_1}} + 57\mathbf{k_{m_2}}\,. \tag{3.22}$$

At this stage, the commensurability relations can be written using the Park-Madden matrix introduced in Eq. 1.29:

$$\begin{pmatrix}\mathbf{a_{t_1}}\\ \mathbf{a_{t_2}}\end{pmatrix} = \frac{1}{17940}\begin{pmatrix}18210 & 450\\ -510 & 17703\end{pmatrix}\begin{pmatrix}\mathbf{a_{b_1}}\\ \mathbf{a_{b_2}}\end{pmatrix}\,. \tag{3.23}$$

We are then able to find the parameters of the extended Wood's relation using Eq. 1.34

$$(P_1 R\theta_1 \times P_2 R\theta_2) = (1.00274R1.241 \times 1.00104R1.381)\,. \tag{3.24}$$

Firstly, the layers are only very slightly rotated so that the system falls in the small angle regime described in Section 1.2.3.b. Secondly, we can extract the relative strains between the layers from this relation using Eqs. (1.35) and (1.36): a small uniaxial relative strain $\varepsilon_{uni}^{rel} = 0.35\%(\pm 0.03\%)$ and an even smaller biaxial relative strain $\varepsilon_{bi}^{rel} = -0.06\%(\pm 0.005\%)$.

To model the effect of these strains on the electronic properties, we need to take them into account in tight-binding calculations. A handy way to do this is to generate directly the periodic computation cell of the atomic positions of the two layers from the commensurability relations.

3.3.3 Tight-binding calculations with relative strain

The generating lattice vectors of the top and of the bottom layers are linked though Eq. (3.23). One set of lattice vectors allows to generate the other and consequently the whole moiré structure. In the presented case, we used unstrained lattice vectors for the bottom layer to generate the full structure. We show later that starting from a strained bottom layer does not change the electronic properties as long as the commensurability relations, and therefore the relative strain between the layers, are the same. The atomic positions for the top and bottom layer are shown in respectively red and blue in Fig. 3.12. The vectors $(\mathbf{a_{m_1}}, \mathbf{a_{m_2}})$ of the moiré are also found from the commensurability relations. These vectors form a periodic cell that is suitable for tight-binding calculations that comprises $3 \times 3 = 9$ inequivalent beatings.

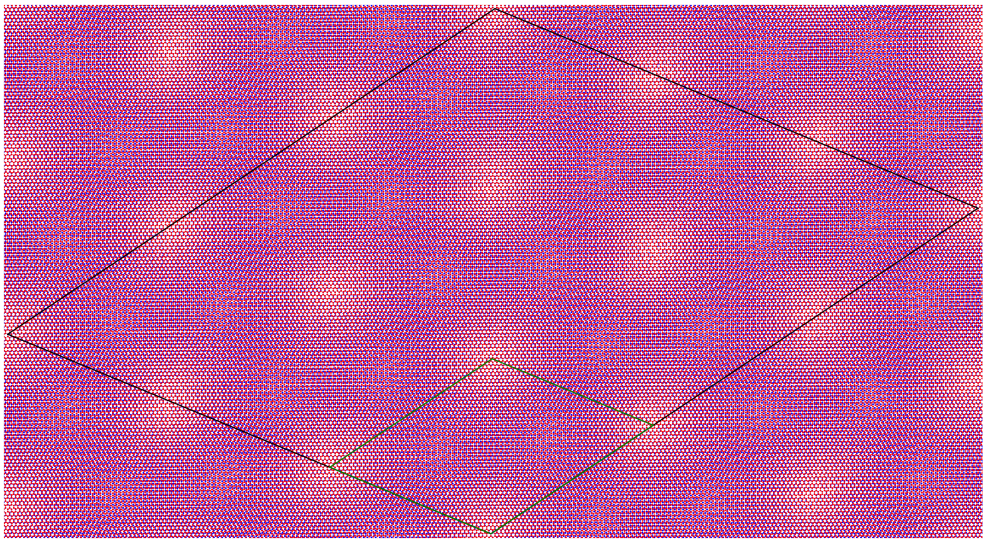

Figure 3.12: Generated atomic positions (structure 1) for the tight-binding calculations of the local density of states (red points: top layer, blue points: bottom layer). The green rhombus represents the beating cell and the black rhombus the moiré cell which describes the true periodicity of the system.

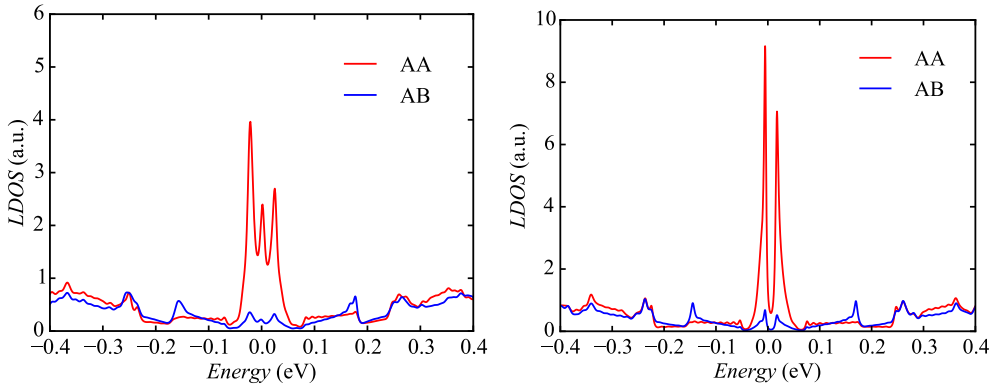

Figure 3.13: Left: Local density of states in AA regions (red) and in AB regions (blue) calculated by tight-binding on the commensurate structure with relative uniaxial and biaxial strain. The peaks match well in number and position with the STS experiment shown in Fig 3.10 **Right:** Calculated local density of states on unstrained twisted graphene layers of twist angle $\theta = 1.25°$ that shows two van Hove singularities localized in AA regions (red) and higher energy peaks in AB regions (blue).

The generated periodic cell contains 71844 atoms: 35880 for the top layer and 35964 for the bottom layer and is called structure 1.

The local density of states calculated using the cell presented above are shown in the left part of Fig. 3.13 for the AA and AB regions. The calculation reproduces the three resonances seen in the STS measurements of Fig. 3.10. In addition, the central peaks in the local density of states are much more pronounced in AA regions than in AB regions which has to be related to the localization of electrons in AA regions by the moiré potential [13, 55, 82, 90, 92]. The high energy resonances marked by arrows and their predominance in AB regions is also captured. These peaks flank dips that indicate a partial band gap opening in higher energy moiré bands [13, 44, 101]. The localization of these peaks in AB regions for small angles has not been reported and deserves further theoretical work.

For comparison, the right part of Fig. 3.13 shows the calculated density of states for the bilayer (26,27) of same rotation angle ($\theta = 1.25°$) but exempt of relative strain. In this case, the only two resonances are van Hove singularities that arise from saddle points in the band structure [13, 15, 50, 54, 55, 82, 90–92, 97, 101]. To have more insight on the phenomena giving rise to the multiple resonances observed experimentally, we performed tight-binding calculations of the complete band structure $E(\mathbf{k})$.

3.3.4 Modification of the electronic band structure by strain

3.3.4.a Generation of the tight-binding cell

The structure used previously to compute the local density of states (structure 1) is composed of 71844 atoms which makes full band structure calculations difficult to perform with reasonable calculation times. A solution would be to restrict the computation to a smaller cell comprising only one beating and therefore less atoms. For this approach to be valid, it is necessary to demonstrate that the structural inequivalence of the beatings has no effect on the electronic properties of the moiré system.

From the experimental side, the local density of states measurements performed in neighboring (and therefore inequivalent) AA regions (left of Fig. 3.14) do not show any remarkable deviation from one another. This is in agreement with tight-binding calculations which show very little differences of the local density of states computed on inequivalent AA regions (right of Fig. 3.14). The absence of any meaningful difference in the local density of states was also predicted by the continuum model of Ref. 55 where the authors concluded that a cell of multiple beatings is a quasi-periodic rep-

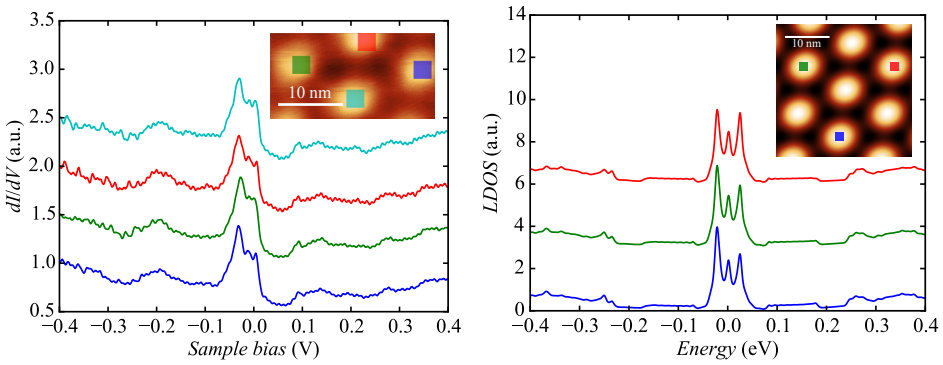

Figure 3.14: Left: Averaged STS spectra taken at different AA regions showing the reproducibility of the multiple van Hove singularities and the absence of significant differences between successive AA regions. Inset : (27.2×14) nm^2 STM topograph ($V_b = -400$ mV,$I_t = 50$ pA) with colored rectangles taken for the area of averaging for the corresponding colored spectra. **Right:** Tight-binding calculation of the local density of states at different AA regions of the moiré cell containing 9 beatings. Only very slight variations of the amplitude of the van Hove singularities are seen. Inset : moiré pattern generated from the commensurability with colored rectangles indicating the location at which the local density of states were calculated.

etition of a single beating cell. It also indicates that it is possible to restrict the study of the electronic properties to one beating even in the case of a cell of multiple beatings.

As a consequence, a second structure (structure 2) was generated containing only one beating and 7988 atoms that is shown in the left part of Fig. 3.15. This structure was generated by modifying the commensurability indices of the structure 1 to get an approximate single beating cell $(i - m = 1)$. The indices generating this cell were then tuned by hand to get the closest strain levels. The extended Woods' notation reads in this case $(1.00324R1.24 \times 1.0013R1.392)$ while the relative strain is $\varepsilon_{uni}^{rel} = 0.38\%$ and $\varepsilon_{bi}^{rel} = 0.04\%$. The calculated local density of states of the two structures are extremely similar as shown in the right part of Fig. 3.15. The following band structure calculations were therefore performed using the structure 2.

3.3.4.b Electronic band structure calculations

Figure 3.16 shows electronic bands $E(k)$ computed by tight-binding in order to reveal the influence of strain in twisted graphene layers. The figure is organized in columns. In each column the top panel shows the density

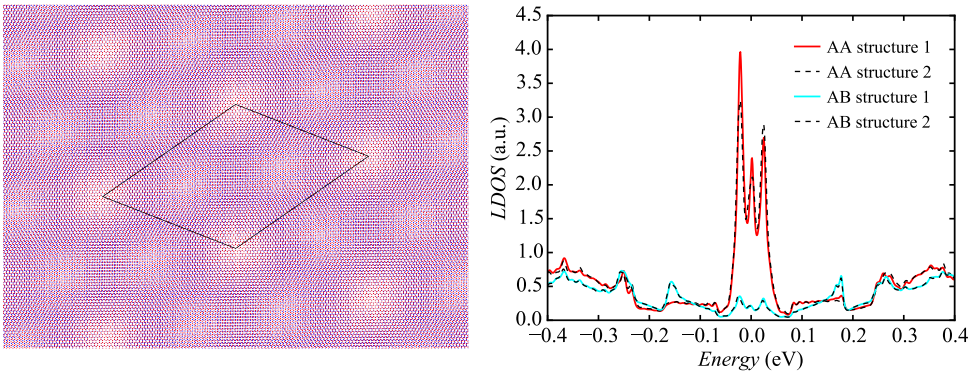

Figure 3.15: Left: Generated atomic positions (structure 2) for the calculations of the band structure (red points: top layer, blue points: bottom layer). The black rhombus represents the periodic moiré cell comprising one beating. **Right:** Local density of states calculated in AA and AB for both structures.

of states in AA and AB regions. The middle panel shows the calculated energy map of the first band above E_F. Lines correspond to the trajectory of the cuts in the band structure presented in the lower panel which shows the dispersion of the valence band and the first ten bands above E_F.

For the unstrained case which is presented in the center column of Fig. 3.16, the conduction band presents six saddle points (S) within the Brillouin zone which are marked by crosses. We note in passing that, contrary to large rotation angles, the saddle points are not located along KK' for such small rotation angle. The result of the calculations with relative strain (using structure 2) is shown in the left column of Fig. 3.16. The middle panel shows that the conduction band is completely reconstructed by relative strain. The threefold symmetry is lost and additional saddle points arise at points marked S_1', S_2', S_1'' and S_2''. In addition, weakly dispersing regions appear around points S_1'' and S_2'' at the corners of the Brillouin zone from which the zero energy resonance in the local density of states originates. The other resonances originate from the saddle points (S'). Cuts in the band structure presented in the left lower panel demonstrate that the entire band structure is modified by the small relative strain when comparing it to the cuts for the unstrained case in the center lower panel. Notably, the linear dispersion is replaced by flat bands when relative strain is applied.

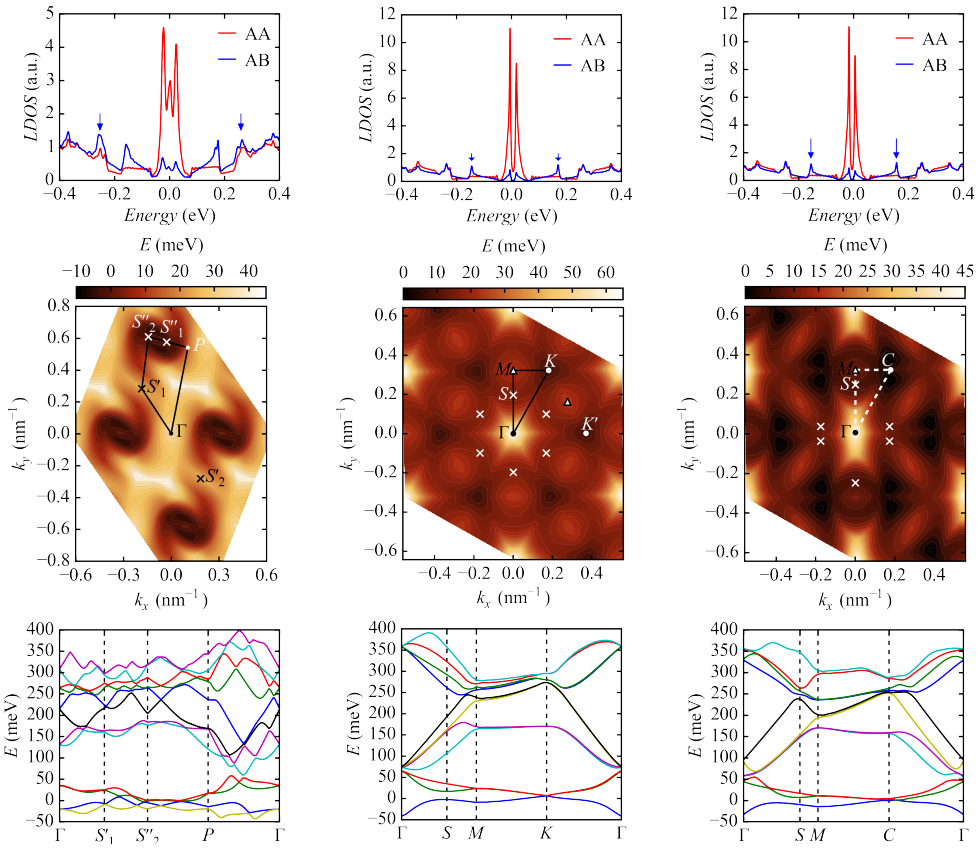

Figure 3.16: Tight binding calculations with and without relative strain. Left: Result for the structure with relative strain of 0.35 % corresponding to the experimental situation (structure 2). **Center:** Result for the unstrained bilayer (26,27). **Right:** Result for the bilayer (26,27) with an absolute strain of 0.35 %. In the lower part of the bottom panel, for simplicity, we have plotted cuts in ΓC and MC since the degeneracy at K and K' points is lifted by absolute strain as pointed in Ref. 65.

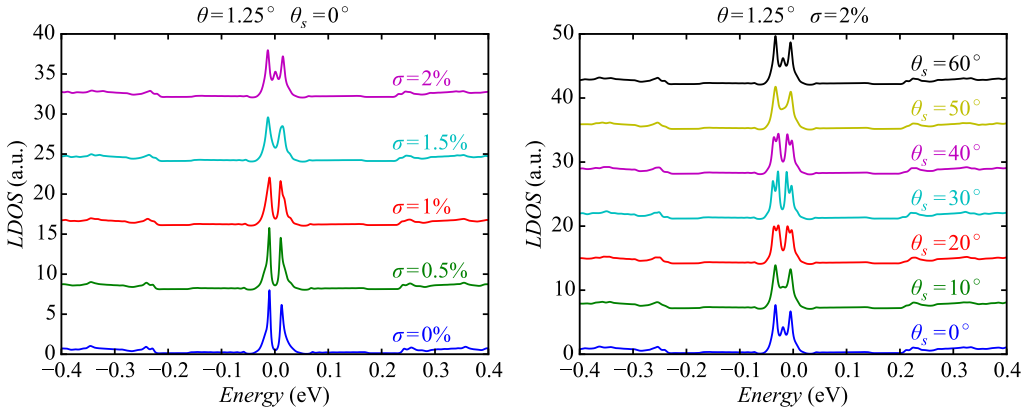

Figure 3.17: Left: Local density of states in AA regions of the bilayer (26,27) ($\theta = 1.25°$) calculated by tight-binding for different absolute uniaxial strain magnitudes along $\theta_s = 0°$. The observed experimental signature is only reproduced for $\sigma = 2\%$ which is six times the observed relative strain. All curves have been shifted vertically for clarity. **Right:** Local density of states in AA regions of the bilayer (26,27) ($\theta = 1.25°$) calculated by tight-binding for $\sigma = 2\%$ along different θ_s.

3.3.4.c Effect of absolute strain

The effect of absolute strain was also investigated as a verification since previous tight-binding calculations [65] have shown that such strain can also alter the band structure of twisted graphene layers with large rotation angles. For consistent comparison between absolute and relative strain, we performed tight-binding calculation with 0.35 % of absolute uniaxial strain (described by the matrix M_{str}) applied in the x direction to the bilayer (26,27). The right panels of Fig. 3.16 show that in this case the local density of states is similar to the unstrained situation and the band structure is only weakly affected. This has to be expected since, as the layers are stretched together, the interlayer relative atomic positions evolve much slower than for relative strain.

Calculations on the same system using larger values of absolute strain, shown in the left part of Fig 3.17, evidence that a magnitude of 2% is required to reproduce the multiple peaks observed in the experimental local density of states. Such strain is much larger than observed in typical Raman measurements of our sample presented in Fig. 3.18. The position of the G peak position is observed at 1587.9 cm^{-1} and the 2D peak at 2711.3 cm^{-1}. In rotated graphene layers, the position of the 2D band is difficult to interpret as the 2D Raman process depends strongly on the electronic dispersion [28].

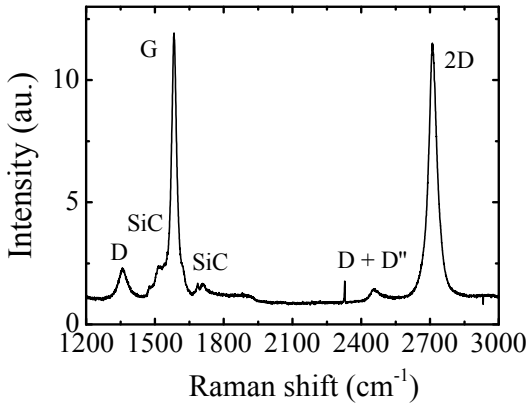

Figure 3.18: Raman spectrum of graphene grown on SiC(000$\bar{1}$) showing the typical G,D and 2D resonances. The shape and position of the G peak indicates a strain value smaller than 0.2%.

The G peak is more straightforward to analyze since it is not affected by the rotation angle [38] but only by doping and strain. The STS spectra in Fig. 3.10 show a n-doping of 25 meV which is too small to have any visible effect on the Raman spectrum [21]. The G peak in our sample is therefore only affected by uniaxial strain which is supposed to split the G peak for strains higher than 0.2%. Since we do not observe such a splitting, the strain in our sample has to be smaller than 0.2%, in agreement with previous measurements [9].

The application of absolute strain through a strain matrix allows to explore the effect of the angle θ_s along which the strain is applied as was done in Ref. 65. Right part of Fig. 3.17 shows the local density of states for $\sigma = 2\%$ for different θ_s. The angles $\theta_s = 0°$ and $\theta_s = 60°$ are equivalent and show the three van Hove singularities already observed. As for $\theta_s = 30°$, the signature of strain is quite different as there are four peaks in the local density of states. At intermediate angles, a continuous transition from three peaks to four peaks occurs showing that the strain angle acts as an additional tuning parameter. While not related to the experimental data, it may be very interesting to explore in detail this angular dependence by calculations of the electronic band structures.

Our experimental system of twisted graphene layers with $\theta = 1.26°$ shows a native relative strain between the layers with almost no absolute strain. The occurrence of this situation seems surprising and calls for a discussion on the origin of the relative strain. This is the aim of the following section where we also discuss the possible effect of a different distribution of the relative strain between the layers.

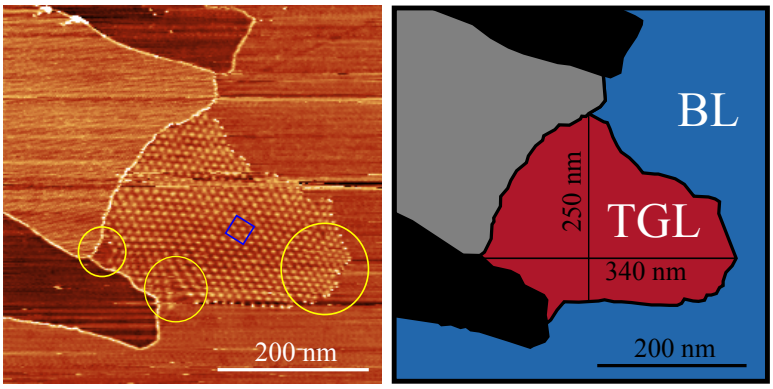

Figure 3.19: Left: STM image of the domain of the probed moiré pattern ($V = -500\,\mathrm{mV}$, $I = 1\,\mathrm{nA}$). Deformation of the moiré is seen at the boundaries (yellow circles) where pinning of the top layer occurs. The STM and STS studies were done in the blue square where the moiré is regular, far from the boundaries. **Right:** Color model showing the bottom layer (BL) in blue and the twisted graphene layers area (TGL) in red. The gray and black regions are other domains separated by grain boundaries.

3.3.5 Discussion on relative strain

3.3.5.a Origin of relative strain

The small native relative strain originates from the pinning of the top layer at its boundaries during the growth as shown in Fig. 3.19. The STS measurements described above were performed in the blue square shown in the left part of Fig. 3.19. This region sits at the center of the graphene grain where the moiré pattern appears (TGL region in the right part of Fig. 3.19). The variation in the moiré pattern near the edges of this grain (yellow circles in the left part of Fig. 3.19) provides evidence that strain is applied at the grain boundary where most probably the top layer is pinned. Indeed, since the moiré results from an interference effect between the layers, any deformation of the atomic lattice is magnified by the moiré pattern. The bottom layer being much more extended (spanning at least the blue and red region in the right part of Fig. 3.19), it is not affected by this local strain or to a much lesser extend. Such a dissymmetry spontaneously induces a relative strain between the two layers. Away from the boundary, the moiré pattern becomes regular indicating that this relative strain is uniform and has reached the measured values.

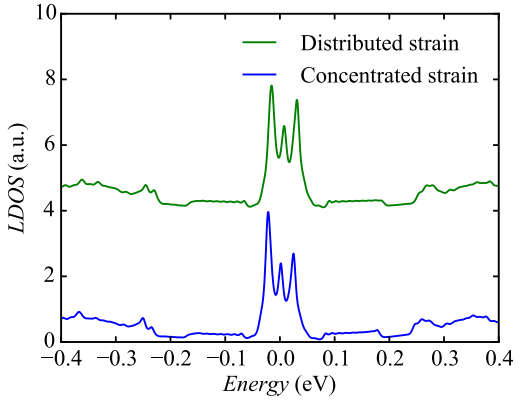

Figure 3.20: Local density of states in AA regions of the top layer calculated by tight-binding for the case where the uniaxial and biaxial strains are concentrated in the top layer and for the case where the relative uniaxial strain was distributed in the two layers. The green curve has been shifted for clarity.

3.3.5.b Effect of the distribution of the relative strain in the two layers

The calculations on relatively strained layers are performed on a structure where the relative strain is confined in a single layer, the other layer being considered strain-free. We have investigated the situation where strain is distributed in the two layers. For this purpose, we applied half of the uniaxial strain to the atomic positions of the bottom layer and determined those of the top layer through the commensurability relations in order to keep the relative strain unchanged. Fig. 3.20 shows the tight-binding calculations of the local density of states in AA regions for both situations, where the relative strain is either confined in one layer or distributed between the two layers. The two results are very similar, with three resonances at the same energies, confirming the robustness of our model to this assumption.

3.4 Conclusion and perspectives

In this chapter, we gave the first experimental evidence of an strain-driven alteration of the band structure of twisted graphene layers. Notably, the Dirac cones turns into flat band under the application of relative strain in the considered system. This considerable change in the electronic band structure can be achieved with relative strain of low magnitude. Much higher amplitudes of absolute strain would be necessary to get the same effects.

The commensurability analysis proves itself an effective tool to evaluate such strains and to couple the experimental details of the atomic positions to tight-binding calculations. This method is very general and can be applied easily to other bilayer systems to get informations on the structure and on the electronic properties.

Nonetheless, we emphasize that the presented effect of relative strain is realized by deformations that are already present in the layers. To go beyond this, our idea would be to apply locally a controlled strain to get desired modifications of the density of states of the bilayer. A first step towards such active manipulations is the focus of the next chapter where we studied the effect on interactions induced by the STM tip on the structural and electronic properties of twisted graphene layers.

CHAPTER 4

TIP-INDUCED INTERACTIONS IN MOIRÉS OF GRAPHENE

4.1 Introduction

In theory, in normal operating mode, STM is an non-invasive technique that allows to probe the sample without acting on it due to the tunneling gap between the tip and the surface of the sample. In practice, extremely short tip-sample distances can lead to interactions between the tip and the sample when imaging the surface. Such interactions are highly dependent on the tunneling conditions: voltage bias (V_b) and current setpoint (I_t).

For example, changing from a high to a low bias across the tunnel junction at a given current setpoint will reduce the number of electronic states available for tunneling. To keep the same tunneling current, one should lower the tunnel barrier and therefore the tip-sample distance favoring short-distance interactions. Similarly, to get a higher current at a given bias value, one should increase the rate of tunneling of the electrons by again lowering the tunnel barrier.

Such considerations about tip-induced deformations are particularly relevant when imaging moiré patterns of graphene on SiC. Firstly, graphene is a material prone to deformations that can sustain elastically above 20% of in-plane strain [49]. Secondly, the graphene layers grown on SiC rest on a 'mattress' of graphene layers allowing elastic out-of-plane deformations. Thirdly, the moiré pattern, resulting from an interference between the atomic lattices, magnifies deformations of the lattices allowing an easier study of strains [62]. Finally, as shown in Chapter 3, native (relative) strain modifies the local

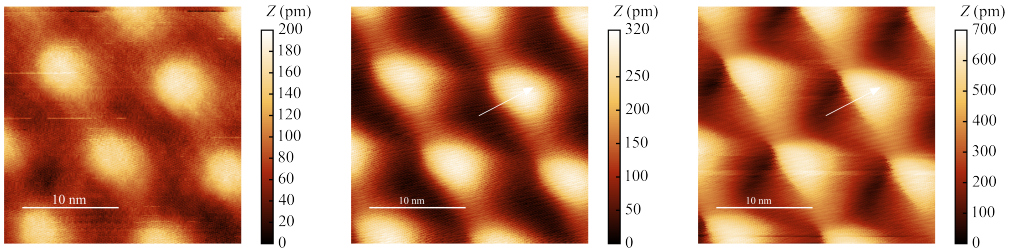

Figure 4.1: (25×25) nm^2 STM images taken at different tunneling conditions. **Left:** $V_b = -800$ mV and $I_t = 300$ pA. **Center:** $V_b = -295$ mV and $I_t = 100$ pA. **Right:** $V_b = -55$ mV and $I_t = 100$ pA.

density of states of the twisted graphene layers system both in the number and position of the van Hove singularities. A mechanical interaction of the tip with the sample could then potentially influence the electronic properties.

The study in Chapter 3 was done by setting high V_b and low I_t leading to high tip-sample distances and therefore corresponding to a non-interacting regime. In this chapter, we reduced the tip-sample distance to study the effect of the tunneling conditions on the STM imaging and STS spectra of the moiré pattern studied in Chapter 3. This led to the emergence of two interacting regimes. For moderate tip-sample distances, the regime is called **elastic** as both the forces exerted by the tip and the substrate on the topmost layer can be modeled using simple springs. For very small tip-samples distances, an **non-elastic** regime appears where the elastic spring model breaks down and the density of states of the twisted graphene layers needs to be taken into account to explain the observations.

4.2 Elastic regime

4.2.1 Effect of the bias value on STM imaging of moiré patterns

To evidence the presence of an eventual interaction between the tip and the surface, we realized successive atomically-resolved STM images of the same moiré pattern with different tunneling biases while keeping the same tunneling current ($I_t = 100$ pA). The resulting images (Fig. 4.1) show a deformation of the moiré pattern that is enhanced with the reduction of the bias voltage. We interpret this deformation as a tip-sample interaction that is stronger when the bias is reduced as the tip-sample distance is decreased. The increase of the anisotropy of the deformation probably reflects the tip

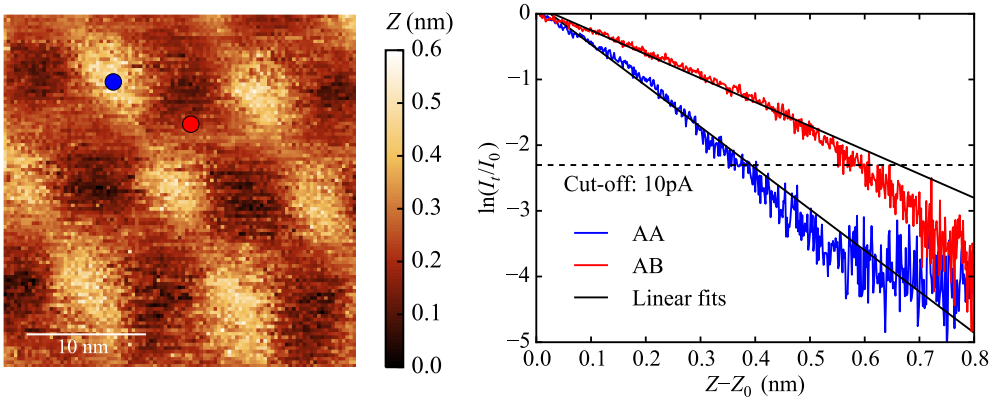

Figure 4.2: Left: STM image of the moiré pattern recorded during the *I(Z)* measurements ($V_b = -200$ mV, $I_t = 100$ pA). **Right:** $\ln(I_t/I_0)$ ($I_0 = 100$ pA) curves as function of the relative tip altitude recorded at AA and AB regions (colored rectangles location). The black solid lines are linear fits and the dashed line represents the cut-off value for the fit.

shape that is brought closer and closer. An anisotropic tip shape can indeed lead to modifications of STM images of the atomic lattice of graphite that are strikingly similar to the deformations of the moiré observed here [63].

4.2.2 *I(Z)* measurements

To have more insight on this interaction, we performed *I(Z)* measurements on the moiré pattern. The STM image recorded at $V_b = -200$ mV and $I_t = 100$ pA is presented in the left part of Fig. 4.2. On every pixel on this image, a *I(Z)* measurement was performed under the same conditions. The right part of Fig 4.2 shows the natural logarithm[1] of the current I_t divided by the current setpoint $I_0 = 100$ pA with respect to the relative altitude of the tip for AA and AB regions, Z_0 being the tip altitude at the beginning of the measurement.

The logarithm of the current for both regions is well fitted by a linear function (black solid lines) except for large Z as the measured current value reaches the noise level. This shows that the dependence of the current is exponential with respect to the tip altitude Z. Assuming the graphene layer fixed (Z_g constant), the variation of the tip altitude Z is the same as the variation of the tip sample distance $d = Z - Z_g$ so that the exponential

[1] In the following, logarithm will always design the natural logarithm of base e (ln).

dependence is given by the tunnel equation Eq. (2.1):

$$I_t = Ae^{-2\kappa d}. \tag{4.1}$$

We can therefore extract κ and the experimental barrier height ϕ from the linear fits, Eq. (2.2) giving

$$\phi = \frac{\hbar^2\kappa^2}{2m}\,. \tag{4.2}$$

For the curves on Fig. 4.2, we get different values for the AA and AB regions:

$$\kappa_{AA} = 3.14 \text{ nm}^{-1} \rightarrow \phi_{AA} = 0.36 \text{ eV} \tag{4.3}$$
$$\kappa_{AB} = 1.82 \text{ nm}^{-1} \rightarrow \phi_{AB} = 0.12 \text{ eV} \tag{4.4}$$

which are both extremely low compared to the expected value for the graphene/Pt-Ir system $\phi \approx 5$ eV.

4.2.3 Apparent barrier height model

Tip-induced interactions were reported numerous times in early STM studies of graphite [58, 87, 103] and more recently, in STM studies of graphene on various substrates [4, 35, 57, 107]. The resulting deformations of the layers were used to explain the enhanced atomic contrast in STM images of graphite [84], the contrast inversions in STM images of carbon nanostructures [71] and the extremely low barrier heights measured by *I(Z)* measurements [20, 56]. Such low barrier height values were dubbed **apparent barrier heights**. They are explained by the presence of a force applied by the tip that pulls the graphene layer as the tip is retracted. The distance between the tip and the sample d, which is the real tunneling distance, decreases more slowly than the tip altitude Z which makes the barrier height appears lower in *I(Z)* measurements. This means that our previous hypothesis that the graphene layer at Z_g does not move should be revised.

It is possible to build a model of the interaction to get more quantitative results by evaluating Z_g as a function of Z. Mamin *et al.*[56] argued that the deformation of the surface by the tip is mediated by a contaminating (insulating) layer between the tip and the topmost graphene layer which is represented by a spring of constant k_t. The graphene layer is also maintained in place by the underlying graphene layers which act also as a spring of constant k_g. We get then the model schemed in Fig. 4.3 where the two springs act on the probed graphene layer.

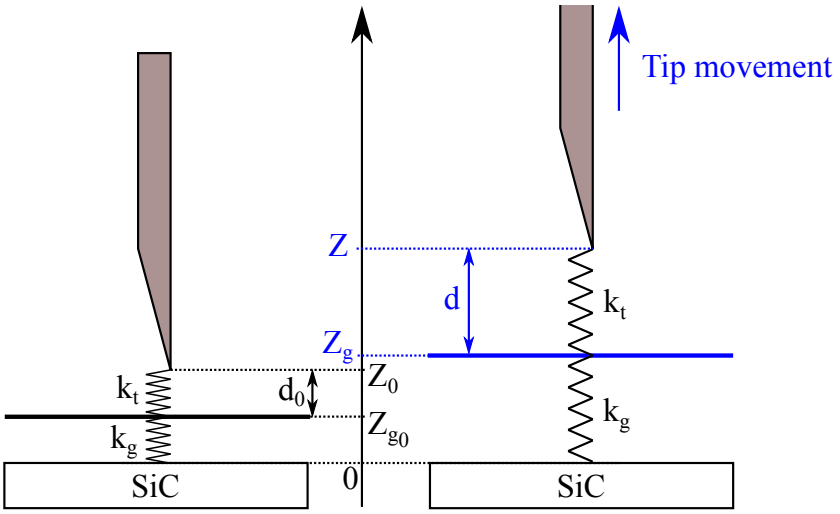

Figure 4.3: Spring model of the tip-sample interaction. The left part is the situation at the beginning of the *I(Z)* measurement. The right part is the situation during the *I(Z)* measurement.

We see that the tip-sample distance d is varying not only as Z changes but Z_g as well. The aim is therefore to deduce $d = Z - Z_g$ from the model. Assuming a mechanical quasi-equilibrium of the graphene layer when retracting the tip, the forces of the springs are equal which gives

$$k_g(Z_g - l_{0,g}) = k_t(Z - Z_g - l_{0,t}). \tag{4.5}$$

where l_0 are the lengths of the unstrained springs. We derive then Z_g:

$$Z_g = \frac{k_t}{k_t + k_g}Z - \frac{k_t}{k_t + k_g}l_{0,t} + \frac{k_g}{k_t + k_g}l_{0,g} = \frac{k_t}{k_t + k_g}Z + C_0 \tag{4.6}$$

gathering the constants in C_0. From this equation, we get d as a function of Z:

$$d = Z - Z_g = Z - \frac{k_t}{k_t + k_g}Z - C_0 = \frac{1}{1 + k_t/k_g}Z - C_0. \tag{4.7}$$

We can replace the obtained expression of d in the logarithm of Eq. (4.1) to get $\ln(I_t/I_0)$ as a function of Z:

$$\ln(I_t/I_0) = \ln(A/I_0) - 2\frac{\sqrt{2m\phi}}{\hbar}d \tag{4.8}$$

$$= \ln(A/I_0) + 2\frac{\sqrt{2m\phi}}{\hbar}C_0 - 2\frac{\sqrt{2m\phi}}{\hbar(1 + k_t/k_g)}Z \tag{4.9}$$

$$= \ln(A/I_0) + 2\frac{\sqrt{2m\phi}}{\hbar}C_0 - 2\frac{\sqrt{2m\phi_{app}}}{\hbar}Z \tag{4.10}$$

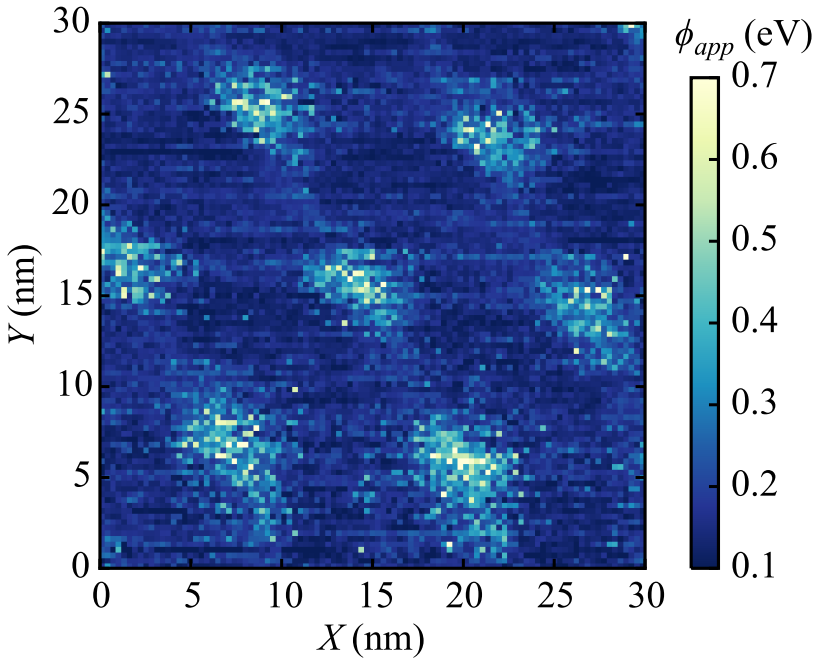

Figure 4.4: Map of the apparent barrier height ϕ_{app} deduced from the linear fits of the *I(Z)* measurements.

with $\phi_{app} = \frac{\phi}{(1 + k_t/k_g)^2}$, the apparent barrier height. Eq. (4.10) shows that the dependence of the current with respect to the tip altitude Z is still exponential but with an apparent barrier height ϕ_{app} which is smaller than ϕ whatever k_t and k_g. This explains the reduction of the measured barrier height by a factor 10 in our experiment which is in agreement with the early reports on graphite [20].

4.2.4 Difference in barrier height between AA and AB regions

Within this formalism, we can study the dependence of the apparent barrier height ϕ_{app} with respect to the position on the moiré pattern. Figure 4.4 shows a map of ϕ_{app} deduced from the linear fits of the *I(Z)* measurements on every pixel. It clearly appears that the AA regions show higher values of ϕ_{app} compared to the other moiré regions. A similar spatial modulation of the apparent barrier height ϕ_{app} was also measured for a moiré formed by a single graphene layer on Pt(111) [104] which prompted two interpretations.

The first one is that the different apparent barrier height ϕ_{app} are ex-

plained by a spatial modulation of the spring constant value k_g if we assume that the barrier height ϕ and the tip interaction k_t are the same on every point of the moiré. Combined STM and AFM measurements on epitaxial graphene on the Si-face of SiC [61] and on STM studies of graphene on hBN [107] both evidenced a deformation of the layer modulated by the moiré formed by the underlying layer. In this case, our results imply that the substrate is stiffer in the AA regions as we have:

$$\phi_{app,AA} > \phi_{app,AB} \rightarrow k_{g,AA} > k_{g,AB} \,. \tag{4.11}$$

However, theoretical predictions of the out-of-plane elastic constant C_{33}, which can be considered as the spring constant k_g per surface unit, are not in direct agreement with this. Density Functional Theory (DFT) calculations with van der Waals correction give a higher elastic constant for AB stacking ($C_{33,AB} = 42$ GPa) than for AA stacking ($C_{33,AA} = 30$ GPa) [81]. The discrepancy with the experimental result of Eq. (4.11) could be related to the fact that the graphene layer is in fact pulled over an area larger than a AA or AB region so that the evidenced interaction cannot be attributed to a single local spring.

The other interpretation relies on the hypothesis that the real microscopic work function of the surface ϕ_s changes as a function of the location on the moiré while k_t and k_g are constant. For graphene on Pt(111) [104], the different surface work functions are explained by a change of the electronic coupling between carbon atoms and the underlying Pt atoms for the bright and dim regions of the moiré. This argument makes sense in the case of the moiré of graphene studied here. The strong interlayer coupling induced by the small angle between the layers induces a difference of the electronic properties between AA and AB regions as shown in Chapter 3. For the measured moiré, we would then have:

$$\phi_{app,AA} > \phi_{app,AB} \rightarrow \phi_{AA} > \phi_{AB} \,. \tag{4.12}$$

However, such a modulation of the work function was never reported nor studied theoretically for twisted graphene layers. The validation of this hypothesis would then need theoretical investigations of the local work function in moirés of graphene.

4.3 Non-elastic regime

The previous measurements were discussed in terms of a simple spring model without taking into account any effect linked to the density of states

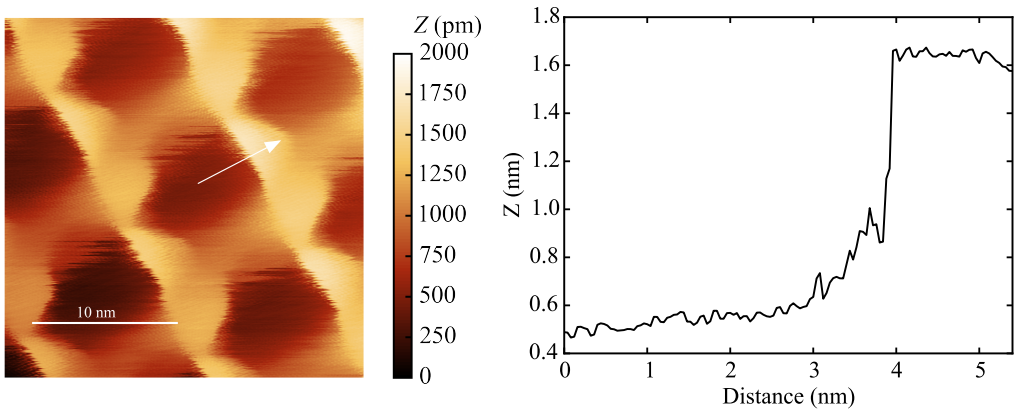

Figure 4.5: Left: (25×25) nm^2 STM image of the moiré pattern imaged in Fig. 4.1 at low bias ($V_b = -15$ mV, $I_t = 100$ pA). **Right:** Tip height profile taken along the white arrow.

of the sample. We will show in the present section that when the bias approaches the energy of the van Hove singularities, additional phenomena appear that cannot be explained by the spring model.

4.3.1 STM imaging at very low bias

The left part of Fig. 4.5 shows a constant-current STM image taken at very low bias ($V_b = -15$ mV) of the moiré pattern imaged in Fig. 4.1. The moiré pattern is strongly deformed but the image also shows abrupt changes in the tip altitude which will be called 'jumps' in the following. This is evidenced by the profile taken along the white arrow (right part of Fig. 4.5) that shows a jump in the tip altitude of almost 1 nm. The jumps were reproducible and located at the same place when scanning in the reverse direction.

4.3.2 *I(Z)* measurements

I(Z) measurements were again performed to investigate this new type of interaction at very low bias. The left part of Fig. 4.6 shows a STM image where *I(Z)* measurements were done in every pixel of the image. The right panel of Fig. 4.6 shows typical measurements performed at the locations indicated by colored squares in the left panel. The *I(Z)* measurements performed in AA and AB regions show the behavior observed in the previous section with an exponential dependence and an apparent barrier height. We note that the measured apparent barrier heights are even lower than before

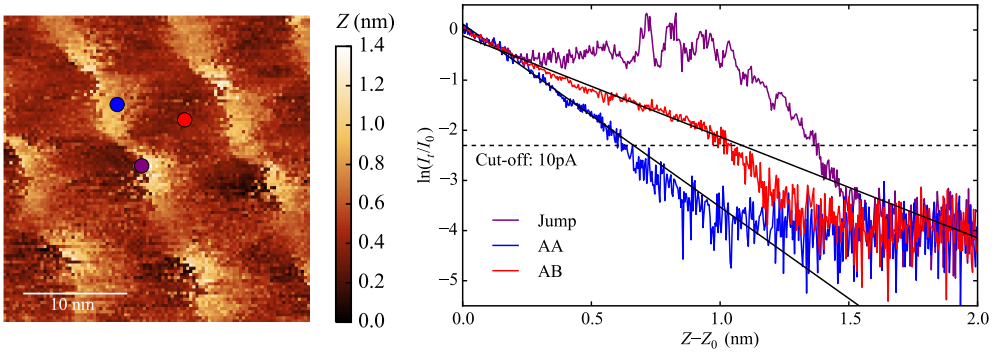

Figure 4.6: Left: (30×30) nm^2 STM image recorded when performing *I(Z)* measurements at very low bias ($V_b = -25$ mV, $I_t = 100$ pA). **Right:** $\ln(I_t/I_0)$ ($I_0 = 100$ pA) curves as function of the relative tip altitude recorded at the colored locations. The black solid lines are linear fits and the dashed line represents the cut-off value for the fit.

($\phi_{app,AA} = 0.11 \pm 0.02$ eV and $\phi_{app,AB} = 0.05 \pm 0.02$ eV) indicating an enhancement of the interaction. The most unexpected feature occurs however in the *I(Z)* recorded at the jump location (purple): the current starts to decrease but then increases when retracting the tip. This is very surprising because according to the tunneling theory, the current is always supposed to decrease with the tip retraction. This increase of the current when doing *I(Z)* measurements occurs at the place of the moiré pattern where the jumps in the tip height are observed when scanning. This evidences the presence of an instability in the tip-sample distance that cannot be explained by the simple spring model.

We showed in Chapter 3 that the density of states of moirés of graphene is affected by the local strain. A deformation of the graphene layers could therefore provoke changes in the density of states at the energies involved in the tunneling processes. These could potentially trigger a sudden increase in tunnel current as observed in the *I(Z)* measurements. In the scanning mode, this sudden increase of the current would result in an abrupt correction of the tip altitude by the feedback loop to keep a constant current, *i.e.* a jump. In order to verify this hypothesis, we realized bias-dependent dI/dV measurements to probe the density of states of the twisted graphene layers at different tip-sample distances.

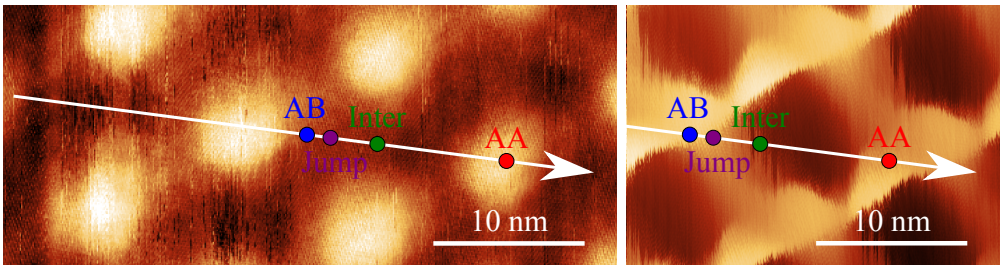

Figure 4.7: Left: (40×17) nm^2 STM image ($V_b = -800$ mV, $I_t = 300$ pA) recorded before performing STS with different initial biases along the white line. The individual spectra shown in Fig. 4.8 were recorded at the colored locations. **Right:** Location of the STS measurements with respect to the STM image of Fig. 4.5.

4.3.3 dI/dV measurements for different bias setpoints

To probe the effect of the bias setpoint on the density of states of the different stacking regions, the dI/dV measurements were performed along the line shown in the left part of Fig. 4.7 crossing AA, AB and intermediate stacking regions. The right part of Fig. 4.7 shows that the jump appearing at very low bias in Fig. 4.5 is located between the AB and intermediate regions at the point named *Jump*. The dI/dV measurements were performed along this line with different bias setpoints and the same tunneling current ($I_t = 300$ pA). As explained in Chapter 2, the value of the bias setpoint sets the functioning point (I_t,V_b) and therefore the tip altitude at the start of the measurement. The tip height is then kept fixed while the chosen bias window is swept during the dI/dV measurement (from -0.2 V to 0.2 V in this case).

Figure 4.8 shows the result for several bias setpoints ($V_b = -800$ mV, -200 mV, -125 mV and -50 mV): the left figures show the recorded dI/dV color map as a function of the position along the line and the bias V_b. Individual spectra are picked at the colored locations that show different stackings (AB, intermediate and AA) or a jump at low bias (Jump). The recorded spectra are plotted on the right of the figure with the corresponding colors. For $V_b = -800$ mV (top figure), given the high bias value, we expect no tip effect and a probing of the intrinsic density of states of the sample. In fact, the local density of states in AA regions are in agreement with the study of Chapter 3 with multiple resonances near the Dirac energy in AA regions due to native relative strain. These dI/dV curves will therefore serve as references when studying the tip-induced effects on the density of states. The STM topography recorded along the line shown in Fig. 4.9 offers supporting information as it shows a weak moiré corrugation, defined as the difference

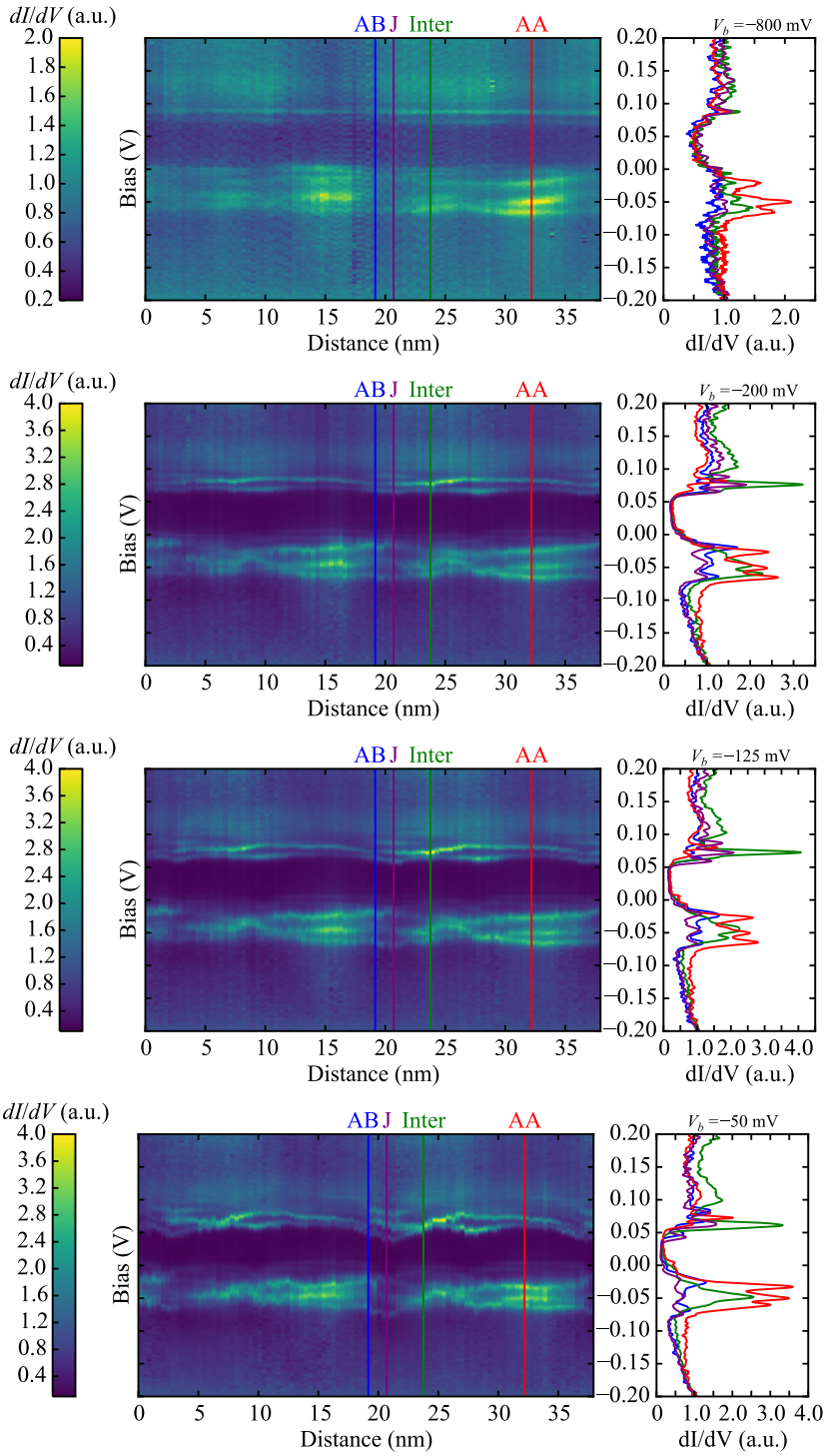

Figure 4.8: Left: Map of the dI/dV measurements along the line at I_t = 300 pA for different V_b. From top to bottom: $V_b = -800$ mV, $V_b = -200$ mV, $V_b = -125$ mV and $V_b = -50$ mV. **Right:** dI/dV measurements performed at the colored locations.

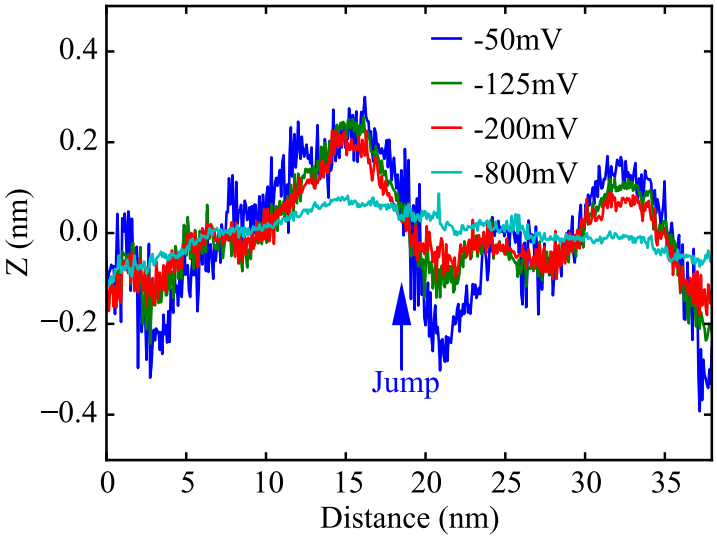

Figure 4.9: Tip height (or topography) recorded during the dI/dV measurements along the line for the different biases.

between the tip height in bright regions and the height in dark regions, with no jump in the tip height for this bias.

For a moderate bias $V_b = -200$ mV, the recorded topography (Fig. 4.9) shows that the corrugation of the moiré increases. But the most striking feature in the local density of states recorded for this bias (Fig. 4.8) is that the energy positions of the van Hove singularities seem to change along the line. This is particularly visible if we compare the spectrum of the intermediate region (in green) and the spectrum of the AA region (in red): the three low-energy resonances are clearly shifted in energy. These changes in energy position are not monotonous as the energy difference between the van Hove singularities decreases and increases along the probed line. Also, it appears that the van Hove singularities intensities diminish in the jump region as seen in the corresponding spectrum (in purple).

The same behavior is also observed for a smaller bias $V_b = -125$ mV shown Fig. 4.8. These effects even appear to be enhanced at this lower bias with a higher moiré corrugation and larger changes in energy of the van Hove singularities. Notably, the spectrum in the intermediate region appear to show only two resonances instead of the three in the AA region. Compared to the previous case $V_b = -200$ mV, the resonances in the intermediate regions are even more shifted in energy with respect to the resonances in the AA region. We also again observe a diminution in intensities of these resonances in the jump region.

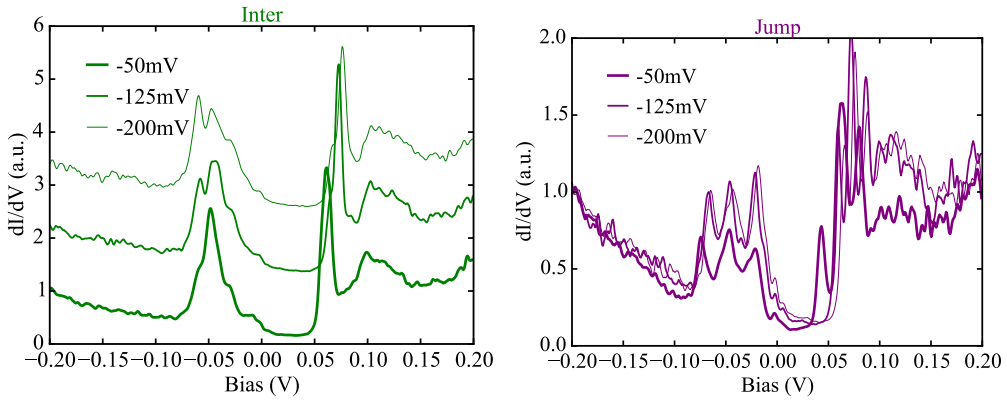

Figure 4.10: Left: dI/dV measurements performed at the intermediate location for the different bias setpoints in Fig. 4.8. The curves were vertically shifted for clarity. **Right:** dI/dV measurements performed at the jump location for the different bias setpoints in Fig. 4.8. The curves are not shifted here.

Still, Figure 4.9 does not reveal a jump in the tip height for $|V_b| \geq 125$ mV linked to a possible instability at these low biases. These jumps are only observed for the topography recorded for $V_b = -50$ mV which is pointed out by an arrow. The changes in energy of the van Hove singularities are here very important as shown in the bottom graph of Fig 4.8 confirming the previous observed trend. The spectrum in the intermediate region shows for example a single peak as it appears that the van Hove singularities completely merge at this point. More importantly, the vanishing of the van Hove singularities in the jump region is here very clear. The observation of these phenomena allows the design of a phenomenological interpretation.

In Chapter 3, the density of states of twisted graphene layers was modified by native strain. The changes in energy of the van Hove singularities, observed at low bias, show that this modification can be triggered by the application of external strain. At small tip-sample distance, the tip can indeed induce a local strain in the graphene layers that changes the separation in energy of the van Hove singularities. It is however difficult to estimate the amount of strain applied as the tip probably induces a non-trivial combination of biaxial, uniaxial strain and rotation in the layers which influences the density of states differently.

The vanishing of the van Hove singularities observed at the jump region may also be due to a tip interaction effect. If the tip can also induce local relative rotation of the layers, the angle between the layers could be locally equal to a magic angle leading to electronic states localized only in

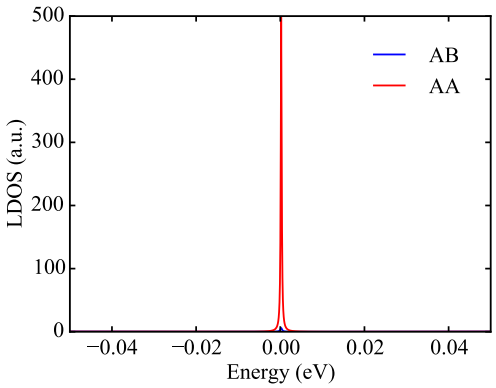

Figure 4.11: LDOS calculated by tight-binding for the first magic angle $\theta = 0.88°$.

the AA regions, the first magic angle 0.88° being indeed very close to the studied angle 1.26°. The left part of Fig. 4.10 shows that the LDOS in the intermediate region becomes a single peak when the bias is very low. This single peak is very similar to the calculation of the LDOS for the magic angle shown Fig 4.11. In addition, the calculation shows very few electronic states at low energy in the AB regions. This is in agreement with the right part of Fig. 4.10 that shows that the intensities of the van Hove singularities diminish in the jump region as the bias setpoint is reduced (and thus the interaction augmented). The fact that traces of the features of respectively the AA and AB regions are observed in the intermediate and jump regions is linked to the fact that the tip probably deforms an area of dimensions larger than the moiré periodicity. This means that the tip interaction acts on all the regions (AA,AB and intermediate) even if the measurement is realized in a single region. In consequence, the local stacking may change in presence of tip-induced interactions with respect to what was observed in the unstrained case.

Our interpretation of the tip-interaction effects at low biases is described schematically in Fig. 4.12. The observed instability is in fact linked to the vanishing of the van Hove singularities induced by the tip interaction which has a strong effect when measuring at low bias. When scanning at high bias, even if the tip interaction could lead to such a vanishing, the integration of the local density of states to yield the tunneling current is done on a large range of energies so that it is unnoticed. However, when scanning at low bias, most of the electronic states that contribute to the tunneling are affected by this disappearance of electronic states. Therefore, when the tip interaction leads to the reappearance of electronic states, the tunneling current increases

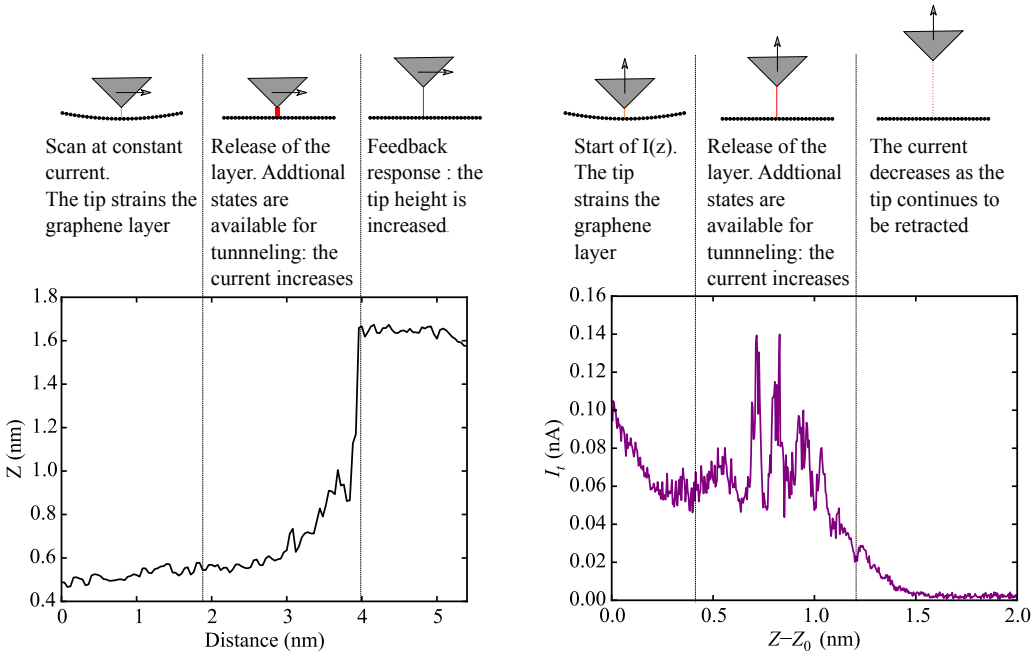

Figure 4.12: Phenomenological interpretation of the observed jumps in tip height when scanning and increase of current when retracting the tip in *I(Z)* measurements at very low biases.

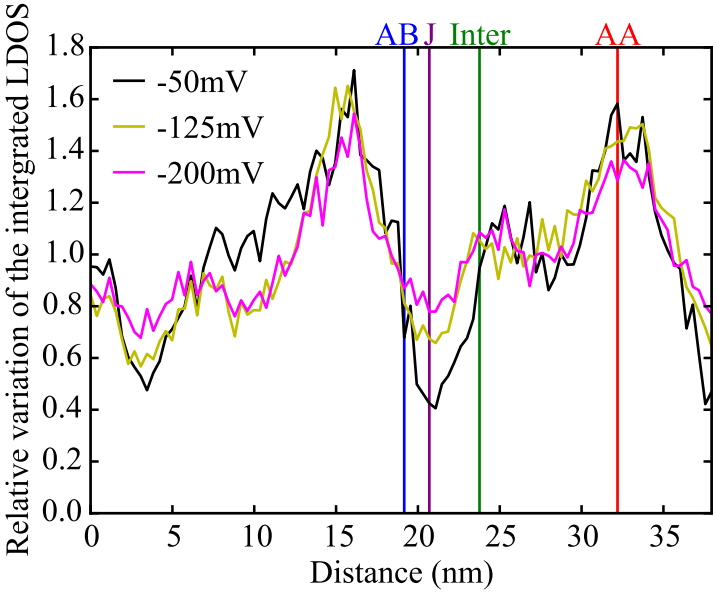

Figure 4.13: Result of the integration of the dI/dV spectrum on the bias window along the line for the different bias setpoints.

abruptly which triggers through the feedback loop a jump in the tip height as observed in Fig. 4.12. The inverse phenomena happens when scanning in the other direction: the sudden vanishing of the electronic states triggers a drop in the tip height to keep the tunneling current constant. This is the situation in the topography of Fig. 4.9 for $V_b = -50$ mV.

This scenario, explaining why the instability is observed only for very low biases, is strengthened by the results of Fig. 4.13. For each bias setpoint, the measured dI/dV spectrum, normalized at high energy (−0.2 eV), was numerically integrated on the bias window $[V_b, 0]$ at each point of the line. The relative variation with respect to the mean LDOS is then plotted in Fig. 4.13. Variations along the line are observed for each bias. However, for $V_b = -50$ mV, there is an abrupt and strong diminution of the LDOS in the jump regions. To keep the same tunneling current in these regions, the tip height must therefore abruptly diminish to lower the tunnel barrier as is experimentally observed.

The anomalous *I(Z)* measurements in the jump region described in the Section 4.3.2 can be explained within the same mechanism. As the tip is retracted at the location where the singularities vanished, the interaction between the tip and the graphene layers is reduced. The increase of the current is then also explained by the appearance of many electronic states in the integrated bias window. The fact that both phenomena, the tip height

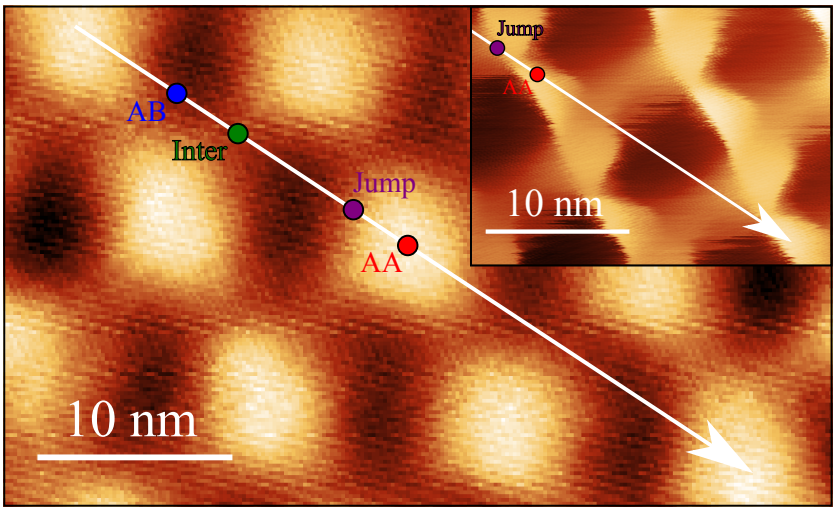

Figure 4.14: STM image ($V_b = -400$ mV, $I_t = 50$ pA) recorded before performing STS with different tunneling currents along the white line. The individual spectra shown Fig. 4.15 were recorded at the colored locations. Inset: Location of the STS measurements with respect to the STM image of Fig. 4.5

jump in Fig. 4.5 and the current increase in Fig. 4.6, are observed at the same place in the moiré is therefore consistent.

4.4 Effect of the tunneling current value

The presented interpretation is highly focused on the effect of the applied bias that both sets the energy window of probed electronic states and the tip-sample distance. However, the tip-induced interaction appears when decreasing the tip-sample distance which can be achieved also by increasing the tunneling current. If the interpretation shown Fig. 4.12 is correct, we should not observe instabilities at any tunneling current value if the bias value is above the energy of the van Hove singularities. To check this, dI/dV measurements were performed along a line (Fig. 4.14) at different tunneling currents while keeping the initial bias at a value far above the energy of the van Hove singularities ($V_b = -400$ mV).

Figure 4.15 shows the result for the different I_t presented in the same format of the previous section: dI/dV map at the left and individual spectra at the right. For a low tunneling current of 400 pA (top part), there is no observable tip-induced effect as we recover the three peaks in AA regions due to native strain as discussed in Chapter 3 and for the highest bias in Fig. 4.8.

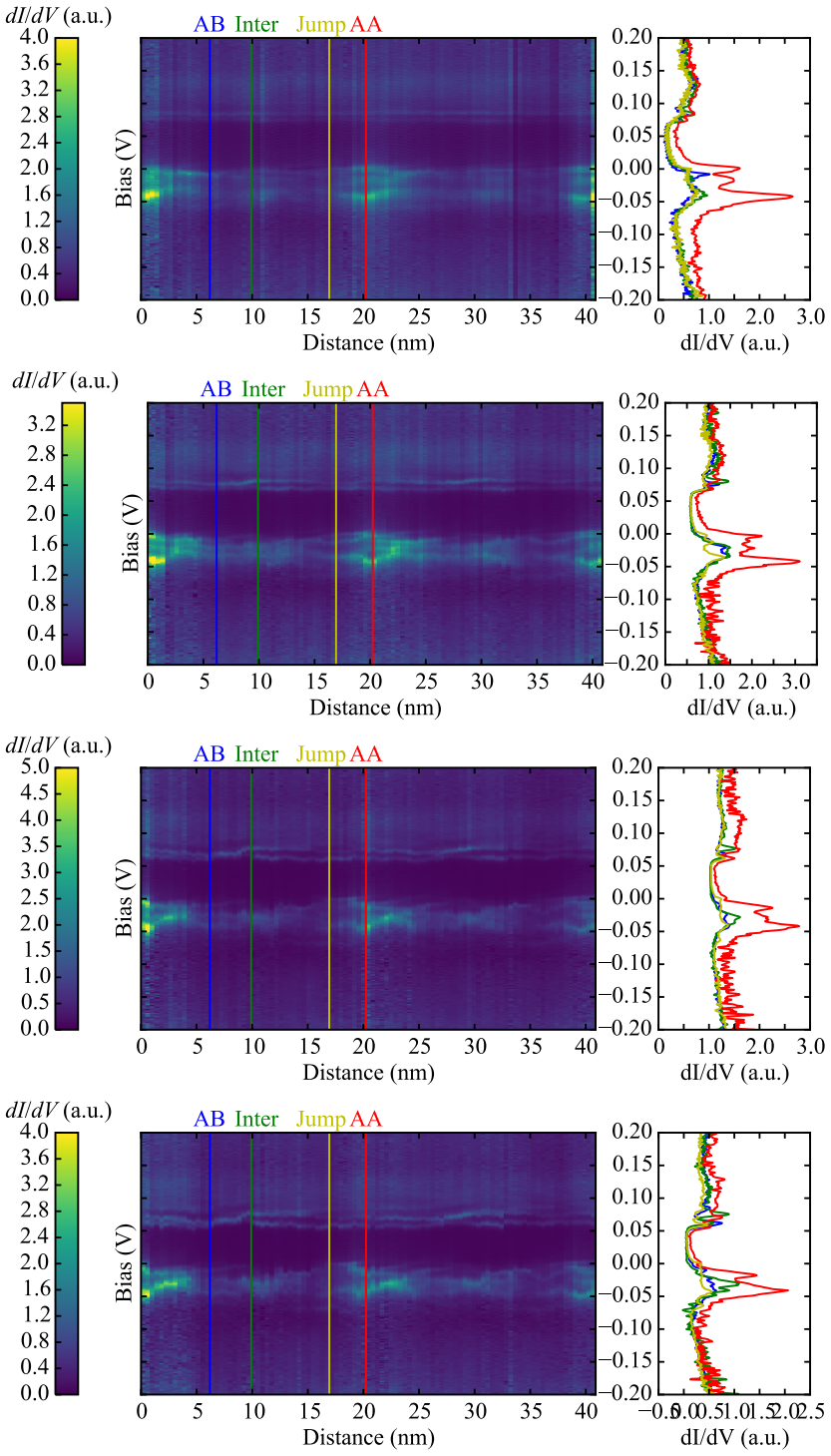

Figure 4.15: Left: Map of the dI/dV measurements along the line at $V_b = -400$ mV for different I_t. From top to bottom: $I_t = 400$ pA, $I_t = 1.4$ nA, $I_t = 3$ nA and $I_t = 4$ nA. **Right:** dI/dV measurements performed at the colored locations.

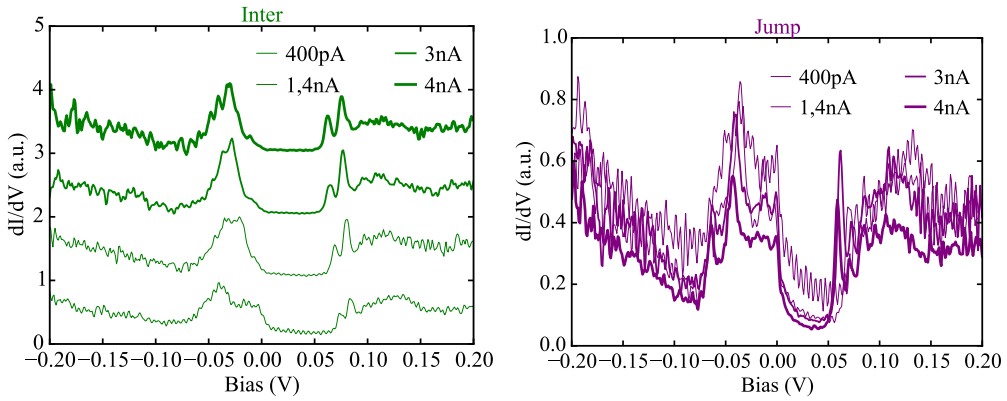

Figure 4.16: Left: dI/dV measurements performed at the intermediate location in Fig. 4.15 for the different tunneling currents. The curves are vertically shifted for clarity. **Right:** dI/dV measurements performed at the jump location in Fig. 4.15 for the different tunneling currents. The curves are not shifted here.

For $I_t = 1.4$ nA, we start to see changes in the energy of the van Hove singularities in the dI/dV map similarly to the bias case of Fig. 4.8. The results for $I_t = 3$ nA, presented just below, show an enhancement of these effects with a visible vanishing of the van Hove singularities in the so-called jump region. The tip-induced interaction can therefore also be modulated by the tunneling current value as it acts on the same parameter as the applied bias value: the tip-sample distance, which is the relevant parameter to consider. The results for highest tunneling current value used ($I_t = 4$ nA) are shown at the bottom of Fig. 4.15. Again, we see in the dI/dV map that there is an even larger modulation of the energy position of the van Hove singularities along the line. The spectrum in the intermediate region (in green) shows again that at this location the singularities are almost merged. Also, the vanishing of the density of states is observed in the jump region.

This set of measurements shows that the same effects on the local density of states are observed when increasing the tunneling current and decreasing the bias, even if they are more difficult to distinguish in the case of the increasing current. The left part of Fig. 4.16 shows that the spectra in the intermediate region vary from a broad bump at low tunneling current to almost a single peak at high tunneling current in agreement with the left part of Fig. 4.10. The intensities of the van Hove singularities in the jump region (right part of Fig. 4.16) are also diminished similarly to Fig. 4.10 for small tip-sample distances. However, the effect of changing the current setpoint on the observed moiré corrugation is extremely weak as shown in

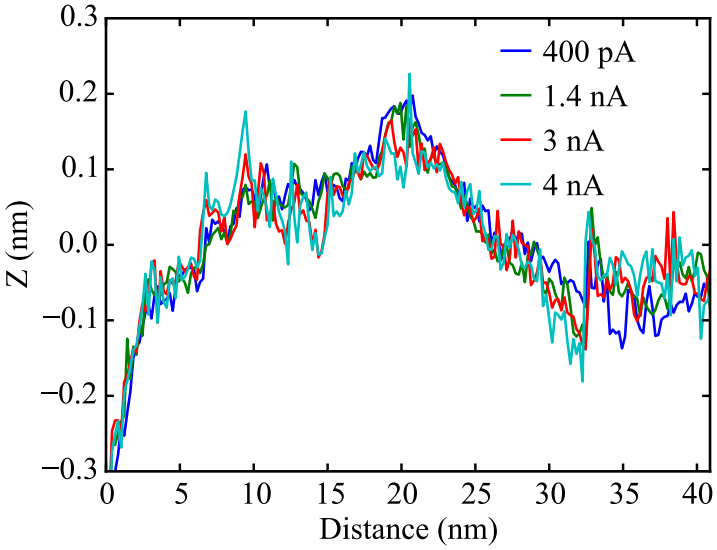

Figure 4.17: Tip height (or topography) recorded during the dI/dV measurements along the line shown in Fig. 4.14 for the different currents.

topography recorded during the measurements (Fig. 4.17). In particular, no jump in tip height are observed (the dip at the beginning of the measurement being unreliable due to the fact that the tip was not stable yet) although the lowest tunnel resistance $R_t = V_b/I_t$ is almost twice smaller than for the lowest bias probed in Fig. 4.8 where the jumps are observed (here, $R_t = 100$ MΩ $< R_t = 166$ MΩ for $V_b = -50$ mV). This is consistent with our instability model presented Fig. 4.12. Even if the intensities of the van Hove singularities are modified when increasing the tunneling current, the bias value is large enough so there are always enough available tunneling states preventing any tip height jump. In this case, we always are in the so-called elastic regime.

4.5 Effect of bias on the moiré corrugation

The measurements in Fig. 4.8 showed a visible effect of the bias on the moiré corrugation, that is the difference in tip height between bright (AA) regions and dark (AB) regions. To discuss it, we use the STM images at different biases shown in Fig. 4.1 where profiles were taken along the white arrow from a dark spot to a bright spot. These profiles shown in the left panel of Fig. 4.18 evidence an increase of the corrugation of the moiré pattern when the bias decreases. We realized such profiles and determined the corrugation for the full dataset. The results, shown in the right panel of

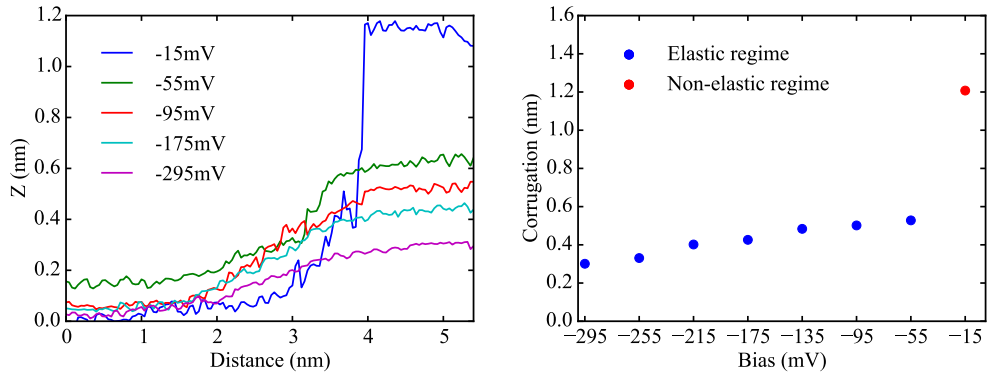

Figure 4.18: Left: Profiles of the tip height taken along the white arrows in Fig. 4.1 for different biases. **Right:** Corrugations determined from the profiles for different biases.

Fig. 4.18, demonstrate that the increase of the corrugation follows a linear behavior with respect to the bias when remaining in the elastic regime. The non-elastic regime shows an abrupt increase in the corrugation reaching more than 1 nm due to the modification of the density of states by the tip as discussed above.

The maximal value of Z is obtained for AA regions whereas the minimum is for AB regions. The observed corrugation can be first be interpreted as a difference of interplanar distances for the two stackings. DFT computations showed that the interlayer spacing in a moiré pattern changes locally between AA and AB regions [92]. This study also shows that the difference in interlayer spacing increases when the twist angle θ is reduced. For θ approaching 0°, the maximal moiré corrugation is then $d_{AA} - d_{AB}$ with the computed interlayer distances $d_{AB} = 3.34$ Å for a AB stacked bilayer and $d_{AA} = 3.61$ Å for a AA stacked bilayer. This means that, at most, the moiré corrugation would be 0.27 Å which is one order of magnitude smaller than our lowest observed value of 0.3 nm for $V_b = -295$ mV. We therefore exclude a difference of interlayer spacing as the sole origin of our observations.

Rong and Kuiper [79] observed the increase of the moiré corrugation for twisted graphene layers from 0.1 nm to 0.25 nm when decreasing the bias from 535 mV to 75 mV. They explain their observations by the presence of a tip-induced interaction that is enhanced when reducing the bias. Such effects are known to increase artificially the atomic corrugation of graphite [39, 84]. This interpretation is highly relevant as our previous experiments proved the presence of such an interaction in our case and that our moiré corrugation values for the elastic regime are in agreement with their study. However, these considerations are only correct for the elastic regime and our

study reveals again that the non-elastic regime must be treated apart by taking into account the local density of states. To do this, a Tersoff-Hamann calculation of the STM topography using the density of states of a strained structure may be useful in simulating the resulting STM image [86].

4.6 Conclusion

The results of Chapter 3 were the starting point of the work discussed in this Chapter as we tried to go a step further by actively modifying the van Hove singularities by applying local strain with the tip.

The *I(Z)* measurements at different biases firstly gave the evidence of a tip-induced deformation of the graphene layers and of different interaction regimes. The apparent barrier height model, designed from a spring model, allowed to nicely fit the results at high and moderate biases and to interpret the differences between the different stacking regions without considering the local density of states. This is the elastic regime.

The appearance of a non-elastic regime with jumps in the STM topography while scanning and in the tunneling current while performing *I(Z)* measurements triggered the investigation by doing dI/dV measurements with different tunneling currents. This allowed to demonstrate the active modification of the van Hove singularities via tip-induced strain by changes in the tunneling conditions for small tip-sample distance. This was a requirement to explain the observed jumps that appear when the bias approaches the energy window of the van Hove singularities.

However, further careful investigations are needed to go beyond the qualitative considerations given here. It is difficult to link our measurements to the actual mechanical properties of the system since too many parameters are unknown: tip characteristics (radius, shape, spring constant), number of involved graphene layers, etc. STM studies at constant height and additional data at constant current would be very useful to have more insight on the observed effects.

CHAPTER 5

GRAPHENE ON TANTALUM CARBIDE

5.1 Introduction

We discussed in the preceding chapters that the substrate can act on the properties of graphene through its elastic response. More generally, without any strain involved, the substrate can have direct effects on the behavior of electrons in graphene. A well-known example is silicon dioxide, a very common substrate for graphene, where trapped charges limit the electronic mobility of graphene [25].

In particular, growing graphene on a superconducting substrate allows to add superconductivity to the long list of interesting properties of graphene thanks to the proximity effect. Notably, it allows to study the combination of superconductivity with the ballistic transport in graphene. The geometry resulting from the growth of graphene on a superconducting substrate is very desirable for Scanning Tunneling Microscopy (STM) studies as the clean graphene layer, which protects the substrate from contamination, can directly be probed with atomic resolution. A low-temperature STM allows then to study locally the superconducting proximity effect in the graphene layer.

This strategy was adopted by Tonnoir *et al.* [89] for graphene on rhenium. Rhenium is a superconducting metal with a critical temperature of $T_c = 1.7\,\mathrm{K}$ that was used as substrate for the growth of graphene by Chemical Vapor Deposition (CVD). The low temperature spectroscopic study of the density of states of the graphene layer reveals a superconducting gap that closes with temperature following closely the Bardeen-Cooper-Schrieffer (BCS) theory. Unfortunately, the coupling between the graphene and the rhenium is so strong that the characteristic electronic properties of the graphene grown in

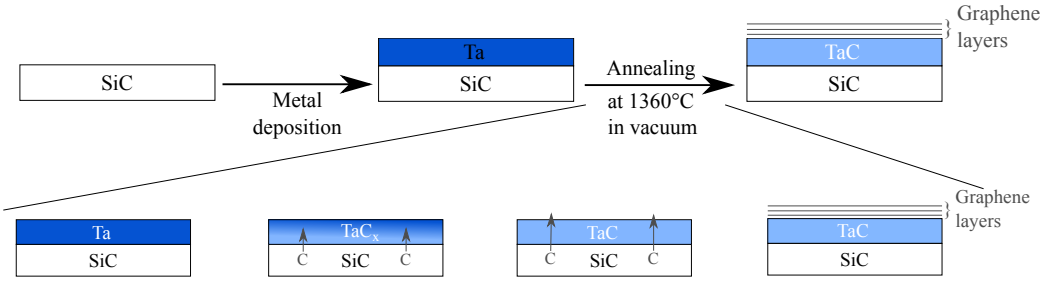

Figure 5.1: Top: Process steps to obtain graphene on tantalum carbide (TaC). **Bottom:** Model of the annealing process: the carbon atoms first saturate the tantalum layer to form TaC and then go through the TaC layer to form graphene layers

this fashion are lost.

We propose to study a similar system of graphene on a superconductor but with a different substrate to avoid the extremely strong coupling regime observed in graphene on rhenium. To do this, we realized the growth of graphene on transition metal carbides: niobium carbide (NbC) and tantalum carbide (TaC) both superconducting below 10 K. Our first investigations resulted in a publication that focused mostly on the characterization of the electrical contact between graphene and NbC and showed that it was possible to couple graphene to a high-quality superconducting carbide [48]. The last chapter of this thesis aims to complement this study by local STM studies of graphene on TaC. The first section will describe the growth process used to realize graphene on TaC. Section 5.3 is a detailed study of the electrical contact of graphene with TaC along the lines of the published work in Ref. 48. Finally, Section 5.4 is dedicated to STM/STS studies of graphene on TaC at low temperature investigating structural effects and the induced superconductivity in the grown graphene layers.

5.2 Growth process

Silicon carbide is not the only carbide on which graphene can be grown. For example, Foster, Long and Stumpf showed that graphite films can be grown on aluminum carbide by annealing [31]. However, the usual techniques to grow superconducting carbides such as NbC and TaC yield rarely high-quality samples leading to reduced superconducting temperatures [36]. We avoided this by realizing simultaneously the growth of graphene and of the carbide using the process shown in Fig. 5.1 that consists in two steps.

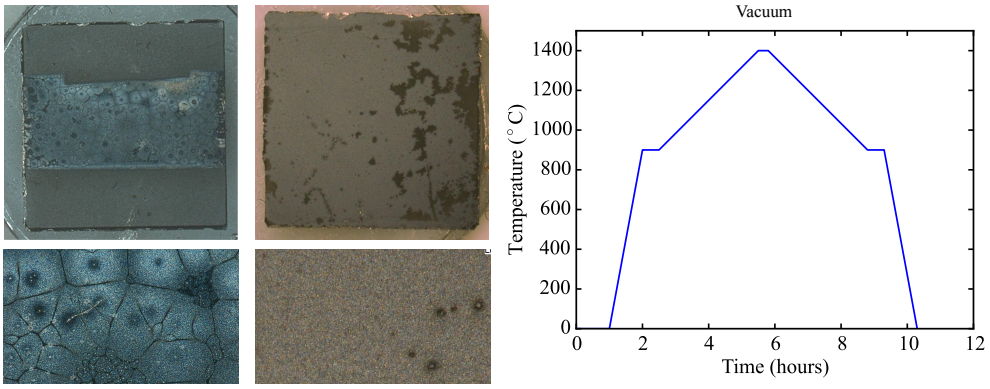

Figure 5.2: Left: SiC substrate with Nb annealed under Ar and Ar/H_2. The bottom is a zoom of the inhomogeneous metallic layer. **Center:** SiC substrate with Nb annealed under vacuum. The bottom is a zoom of the metallic layer that shows a gray and homogeneous aspect. **Right:** Temperature profile used for the annealing under vacuum

Metal deposition The first step is the deposition of a tantalum (Ta) film by electron-beam evaporation on a silicon carbide (SiC) substrate. The thicknesses usually used were between 20 nm and 40 nm with a deposition rate of 0.1 nm/s.

Annealing After the deposition step, the substrate with the evaporated metal film was annealed in the induction oven used for the graphene growth. At first, we used the same annealing protocol as for the graphene growth on SiC, presented in Chapter 2, that consists in the substrate-etching step under Ar/H_2 and a graphene growth step under argon. But our previous experiments on NbC have shown that this led to a contamination of the metallic layer (Left of Fig. 5.2) which results in poor electrical properties. The substrate-etching step was therefore removed, being irrelevant when all the SiC is covered by tantalum, and the annealing was done under vacuum to avoid any contamination from the gases. The resulting growth program is presented in the right part of Fig. 5.2 and consists of an annealing step at 900°C for 30 min to clean the sample followed by a graphitization step at 1360°C for 20 min using slow temperature ramps. The bottom of Fig. 5.1 provides a sketch of the probable growth scenario [48]. Tantalum has a high melting temperature ($T_{melting} \sim 3000$°C) which allows it to withstand the annealing temperature. The SiC however starts to dissociate by silicon sublimation leaving excess carbon atoms. These carbon atoms diffuse in the tantalum layer, carbonizing it partly to form TaC_x, x being the carbon to

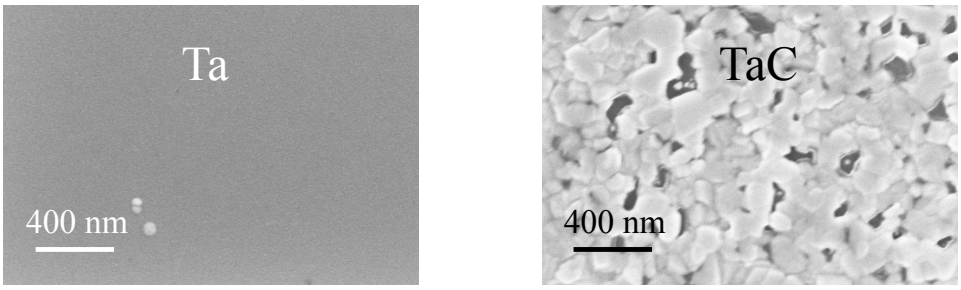

Figure 5.3: Left: Scanning Electron Microscopy (SEM) image of the tantalum film before annealing. **Right:** SEM image of the same film after annealing showing the granularity of TaC.

tantalum ratio. As the annealing continues, the Ta layer becomes saturated by carbon atoms becoming stoichiometric TaC ($x = 1$). Carbon atoms originating from a further decomposition of SiC migrate to the surface of the carbide and combine into graphene layers. This solid-state reaction allowed to carbonize the tantalum film to get stoichiometric TaC and *in fine* graphene layers on the top of the TaC film.

Figure 5.3 compares the aspect of the tantalum film before and after annealing. It shows that, starting from a uniform tantalum layer, we get granular TaC which is an evidence of the solid-state reaction during the annealing.

5.3 Transport measurements

Before taking interest in the graphene layer grown on the top of TaC, the quality of the TaC resulting from the growth process was investigated. This was done by transport measurements determining the superconducting critical temperature and critical field.

5.3.1 Critical temperature and critical field of TaC

The TaC crystal structure is of the rock-salt (NaCl) type with tantalum atoms arranged in a face centered cubic lattice and carbon atoms in the octahedral sites so that the carbon to tantalum ratio is 1. If not all the sites are occupied (carbon vacancies), the carbon to metal ratio x is inferior to 1 and the chemical formula is noted TaC_x. The presence of carbon vacancies reduces the superconducting critical temperature of TaC_x [36]. For a compound of high stoichiometry (x close to 1), the critical temperature can reach 10.35 K. On the other hand, TaC_x is no longer superconducting for

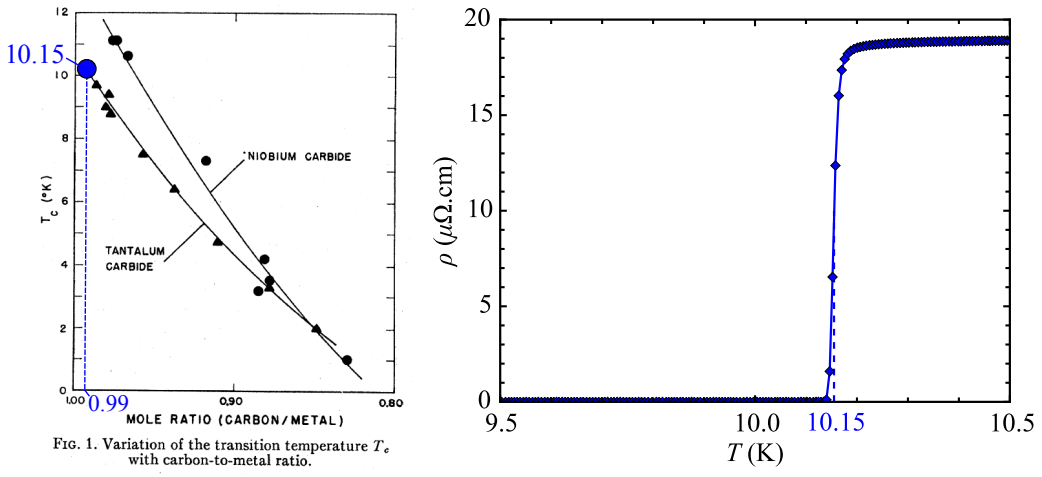

Figure 5.4: Left: Critical temperature T_c of TaC_x and NbC_x with respect to the carbon to metal ratio x. Data for the measured sample in blue. Adapted from Ref. 36. **Right:** Resistivity of the produced TaC film with respect to temperature showing a superconducting transition at $T_c = 10.15$ K.

low stoichiometries ($x < 0.8$). The critical temperature is therefore a strong indicator of the quality of the TaC film.

The low-temperature resistivity was measured using a 4-probes van der Pauw geometry to remove the resistive contributions from the contacts [96]. The resulting resistivity curve at low temperature is shown on the right part of Fig. 5.4 with a clear superconducting transition occurring at 10.15 K. This temperature is far above the critical temperature of tantalum (4.45 K) and quite close to the critical temperature of fully stoichiometric TaC (10.35 K). Reporting this value of the critical temperature (in blue) in the left part of Fig. 5.4, we deduce that the carbon to metal ratio x is superior to 0.99 which proves that the annealing process yields high-quality TaC.

The critical field H_{c2} of the same film was also studied with respect to the temperature. Left part of Fig. 5.4 shows the resistivity with respect to the magnetic field at several temperatures. As expected, the superconducting transition occurs at lower magnetic fields when increasing the temperature. We note some unexpected features such as sharper transitions accompanied by an overshoot of the resistivity for high temperatures. This overshoot is frequently observed for type-II superconductors and known as the peak-effect. The origin of this anomaly is however unclear. It was shown to occur when measuring an inhomogeneous sample with 4-points geometry leading to an inhomogeneous current redistribution at the superconducting transition [94]. Another proposed explanation is the breaking of the vortex lattice

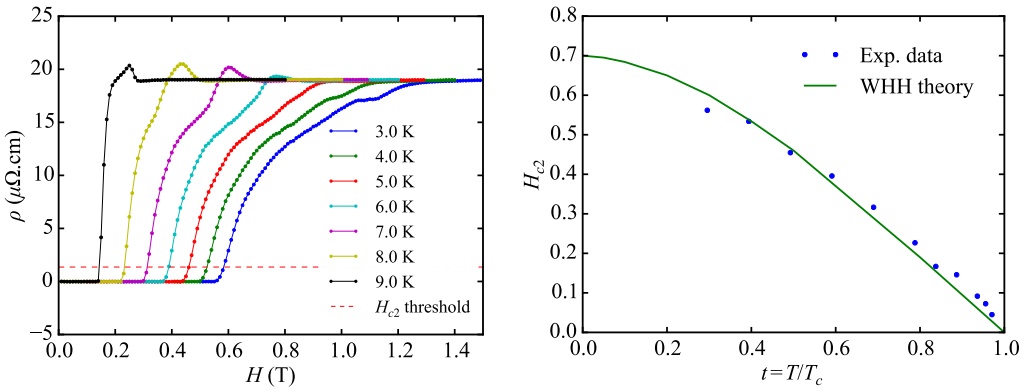

Figure 5.5: Left: Resistivity of the TaC film with respect to magnetic field for different temperatures. The dashed line is the threshold of detection of the normal state to determine $H_{c2}(T)$. **Right:** Extracted critical field H_{c2} with respect to the reduced temperature $t = T/T_c$ (blue dots) with the fit from the Werthamer-Helfand-Hohenberg theory (solid line).

with disorder-order transitions due to vortex pinning [53]. In any case, the presence of this effect evidences inhomogeneity in the TaC layer which can be expected in view of the granularity of the film in the SEM images in Fig. 5.3.

All transitions show an inflexion point at higher fields that could also have the same origin as the peak effect or comes from a second superconducting transition at higher field. To avoid the influence of these deviations in the $\rho(H)$ transition, the critical field H_{c2} was taken at the onset of the transition when the resistivity exceeds 7% of the resistivity in the normal state (dashed red line). The $H_{c2}(T)$ data determined by this method are shown in the right part of Fig.5.5 with respect to the reduced temperature $t = T/T_c$. The Werthamer-Helfand-Hohenberg (WHH) theory for orbital pair-breaking in an applied magnetic field [100] (solid green line) is then fitted to the experimental data to get the critical field at T=0 K: $H_{c2}(0) = 0.7$ T. A previous study on a TaC sample of similar quality [29] reported a slightly lower value of $H_{c2} = 0.5$ T. The discrepancy between the experimental data and the WHH theory can be solved by taking into account other pair-breaking mechanisms like spin-orbit scattering that lower the $H_{c2}(0)$ deduced from the WHH theory.

5.3.2 Transmission Line Measurements

The presented graphene growth process leads to a highly-transparent electrical contact between the metallic carbide and the graphene layers [48]. The

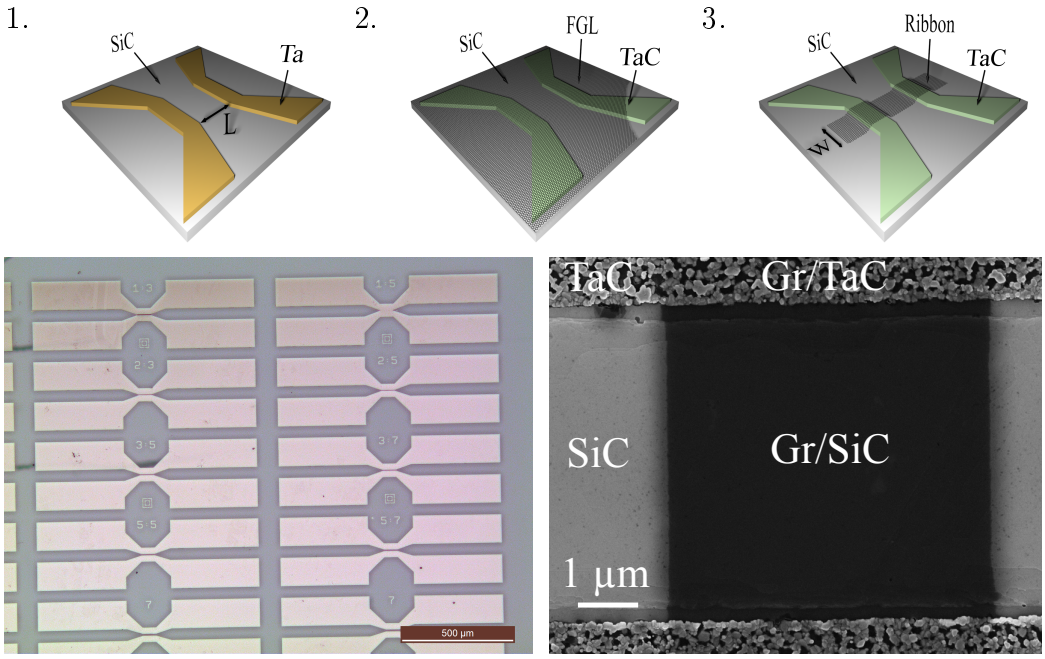

Figure 5.6: Top: Procedure to realize Transmission Line Measurements devices composed of Few Layers of Graphene (FLG) and tantalum carbide contacts. Adapted from Ref. 48. **Bottom left:** Optical microscope picture of the differently spaced tantalum contacts before growth (Step 1). **Bottom right:** SEM picture of an etched graphene ribbon contacted by TaC after the full processing (Step 3).

good quality of the contact is thought to come from a charge transfer between the graphene and the carbide and from the formation of edge contacts during the growth. These two phenomena were separately shown to reduce the contact resistance [73, 99] and are here realized simultaneously in a single step.

Transmission Line Measurements (also known as Transfer Length Measurements or TLM) were used to probe the quality of the electrical contact. This method consists in measuring graphene ribbons of different widths and lengths to have different spacings between the carbide contacts. The resistance of such a device can be decomposed into two contributions: the resistance of the graphene in the ribbon and the contact resistance, which are in series. Assuming a homogeneous specific contact resistance R_c to the graphene ribbon and a uniform sheet resistance R_s of the graphene, the resistance R of a ribbon of width W and length L is given by

$$R \times W = 2R_c + R_s \times L\,. \tag{5.1}$$

This means that the product $R \times W$ at zero-length gives directly twice the specific contact resistance $2R_c$.

In practice, we measure the resistance of ribbons of different lengths to find the linear dependence and extrapolate the zero-length value. The samples for TLM were realized by the following process steps shown in the upper part of Fig. 5.6:

1. Definition of tantalum contact geometry using standard optical lithography techniques

2. Simultaneous growth of TaC and graphene, realizing the electrical contact between the two

3. Definition of graphene ribbons of different widths by oxygen plasma etching

The used lithography mask allows to have in principle up to 32 measurable devices per sample with widths ranging from 3 to 10 μm and lengths from 1 to 20 μm. In practice, there are around 20 exploitable devices per sample due to usual lithography problems such as external contaminations.

The results for the three measured samples are displayed in Fig. 5.7. The standard deviation of the product $R \times W$, depending only on the length according to Eq. (5.1), was derived from the variation of the resistance of devices of different widths with the same length.

The first sample had no exploitable devices for lengths below 5 μm but shows a small standard deviation of the product $R \times W$ for the larger lengths.

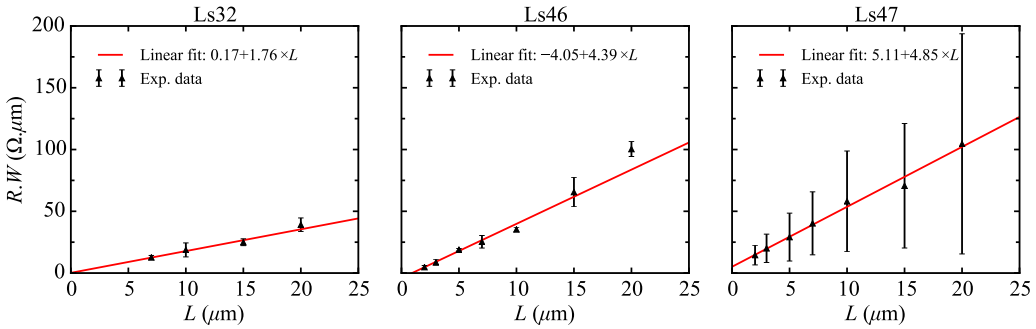

Figure 5.7: Resistance times width ($R \times W$) with respect to length for three samples (black triangles). The solid red line is the linear fit of the experimental data.

The linear fit allowed to extract a specific contact resistance of $R_c = 80 \pm 2360$ $\Omega.\mu$m which is extremely low but with a large error margin. The small-length devices of the second sample were exploitable and allowed to have more experimental data points. We get in this case a negative contact resistance of $R_c = -2.0 \pm 2.5$ k$\Omega.\mu$m which is surprising but still within a large error margin. Finally, the third sample showed huge standard deviations in $R \times W$ compared to the previous ones. Nevertheless, the linear fit gives a more realistic value of $R_c = 2.55 \pm 0.36$ k$\Omega.\mu$m.

The best contact resistances values reported for graphene are of the order of $150 - 200$ $\Omega.\mu$m [41, 99] but are technologically challenging to achieve. Typical values of R_c are usually of the order of $2 - 3$k$\Omega.\mu$m [75] which is what we observe while realizing the contact in a single growth step. Our previous experiments on NbC resulted in even lower contact resistances [48] which indicates that the measured values could probably be improved.

The results for the investigated samples tend to show that the TLM model is in fact not very adapted to describe the measurements. The hypotheses of the model, the homogeneity of the contacts and the uniformity of the material between the two, are probably not respected in our case. The SEM image (bottom right of Fig. 5.6) shows indeed an interface of large granularity with even holes in the TaC layer. This indicates that the current injection in the case of the TaC contacts is probably very inhomogeneous.

5.3.3 Josephson junctions

To check the transparency of the contact between the graphene layer and the carbide, Josephson junctions of TaC-graphene-TaC have been investigated. The Josephson effect is the flow of a supercurrent in a non-

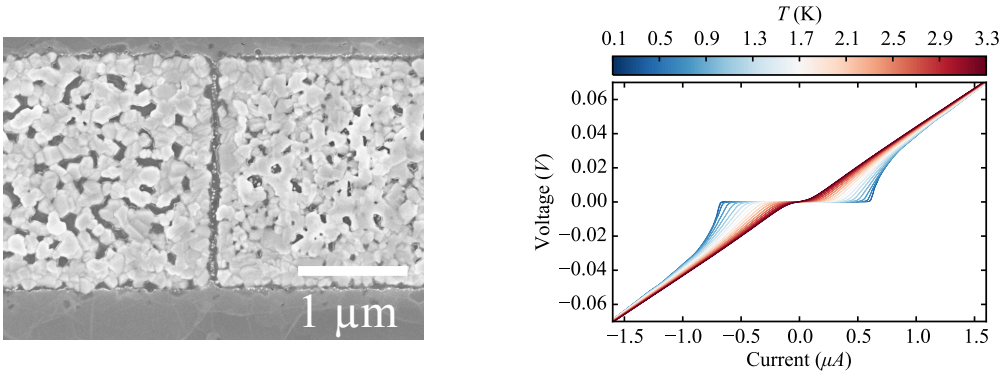

Figure 5.8: Left: SEM picture of the junction with TaC contacts **Right:** Temperature dependence of the current-voltage characteristic of the TaC junction (from $T = 100$ mK to 3.3 K in steps of 200 mK).

superconducting (insulator or normal metal) junction between two superconducting contacts [42]. This supercurrent arises from the coherent transport of Cooper pairs through the normal part from one contact to the other. The efficiency of this process depend highly on the transparency of the interfaces between the superconducting parts and the normal part. The presence of a Josephson effect is therefore an indicator of transparent interfaces between the carbide and the graphene.

TaC-graphene-TaC junctions were realized as shown Fig. 5.8 following the fabrication steps 1 and 2 described above but omitting the etching step 3 for simplicity. Despite the granularity of the contacts, the interface seems better defined compared to the TLM devices. The voltage-current characteristic was recorded at different temperatures by biasing the junction with a DC current, shown in the right part of Fig. 5.8. At 100 mK (bluest curve), the junction sustains a current up to 0.6 mA in the junction without any voltage drop: this is a clear signature of the Josephson effect.

When the temperature is raised, there is a weakening of the supercurrent due to the appearance of thermal fluctuations governed by the thermal energy $k_B T$ that overcomes the Josephson energy $\hbar I_c/2e$ for $T = 3.3$ K (reddest curve) where the supercurrent disappears. At this temperature, the TaC contacts are still superconducting but the superconducting pair correlations are no longer transmitted coherently between them. The establishment of the supercurrent is then limited by the decoherence of the interfering quasiparticle excitations due to the diffusion across the graphene in the so-called long junction regime.

We also studied the critical current I_c of the junction with respect to the out-of-plane magnetic field B. In an ideal Josephson junction, the critical

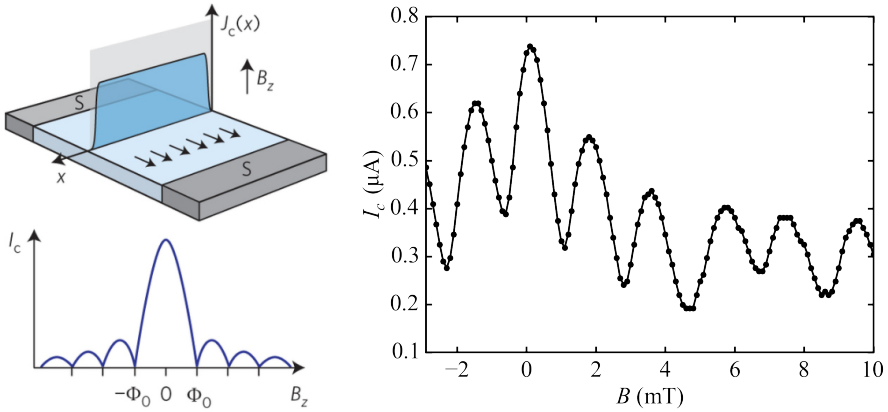

Figure 5.9: Left: Critical current density distribution and Fraunhofer pattern of the critical current for an ideal Josephson junction [78]. **Right:** Critical current for the TaC-graphene-TaC junction with respect to magnetic field.

current density $J_c(x)$ is uniform along the interface. To have the critical current of the junction at zero-field, the integration over the width W is then straightforward:

$$I_c(B=0) = |\int_0^W J_c(x)dx| = J_c W\,. \tag{5.2}$$

When applying a out-of-plane magnetic field, it can be shown [88] that, due to quantum interference effects, the critical current density is sinusoidally modulated along the width of the junction:

$$J_c(x,B) = J_c(x)\sin\left(\frac{2\pi}{\Phi_0}t_b B x\right) \tag{5.3}$$

where $\Phi_0 = h/2e$ is the quantum of magnetic flux and t_b is the length on which the magnetic field penetrates the junction. $t_b = L + 2\lambda_L$ is taken as the sum of the length L of the normal part and of the London penetrating depth λ_L of the magnetic field in the superconducting contacts, with $\lambda_L = 100$ nm as a typical value. The critical current is given by

$$I_c(B) = \left|\int_0^W J_c(x)\sin\left(\frac{2\pi}{\Phi_0}t_b B x\right)dx\right| \tag{5.4}$$

which is nothing else than the modulus of the Fourier transform of $J_c(x)$. In the case of a uniform J_c, the critical current with respect to magnetic field is

then

$$I_c(B) = \left| I_c \frac{\sin\left(\frac{\pi}{\Phi_0} t_b W B\right)}{\frac{\pi}{\Phi_0} t_b W B} \right| \tag{5.5}$$

which is a cardinal sine function similarly to the diffraction by a gate function. The critical current therefore shows a Fraunhofer pattern as shown in the left panel of Fig. 5.9 with the zeros corresponding to the situation when flux through the junction area $\Phi = t_b W B$ equals to an integer number times the flux quantum Φ_0.

For a situation where J_c is non-zero at only two positions (Superconducting QUantum Interference Device or SQUID-like geometry), the situation is very similar to the Young slits experiment and I_c shows sinusoidal oscillations instead:

$$I_c(B) = \left| I_c \cos\left(\frac{\pi\phi}{\Phi_0}\right) \right| . \tag{5.6}$$

The critical current with respect to magnetic field for the probed junction is shown in the right panel of Fig. 5.9 and shows oscillations. But these oscillations deviate from the cardinal sine and resembles more to a sinus: they all have the same width and do not appear to decay as strongly as for a cardinal sine. This is probably due to variations in the junction length along the width of the junction, due to the granularity of TaC. This creates preferential current paths leading to a current distribution that is between a SQUID-like and a homogeneous distribution. Moreover, these current paths are not symmetric with respect to middle of the width of the junction as evidenced by the non-complete vanishing of the critical current when sweeping magnetic field.

The periodicity of the measured oscillations was used to extract the area of the junction $A_B = t_B W = 0.114\ \mu\text{m}^2$. This value is much smaller than the area of the normal region estimated from the SEM image $A^L_{SEM} = (L_{SEM} + 2\lambda_L) \times W_{SEM} = 0.66\ \mu\text{m}^2$, even when neglecting the London penetrating depths $A_{SEM} = (L_{SEM}) \times W_{SEM} = 0.24\ \mu\text{m}^2$. This means that the supercurrent does not flow in the full width of the junction. A possible explanation is the presence of grains, visible in the SEM image, between the contacts that probably reduce the overall junction area.

5.4 Low-temperature STM measurements

The transport measurements revealed many effects due to the inhomogeneity of the superconducting TaC layer prompting us to investigate it at the

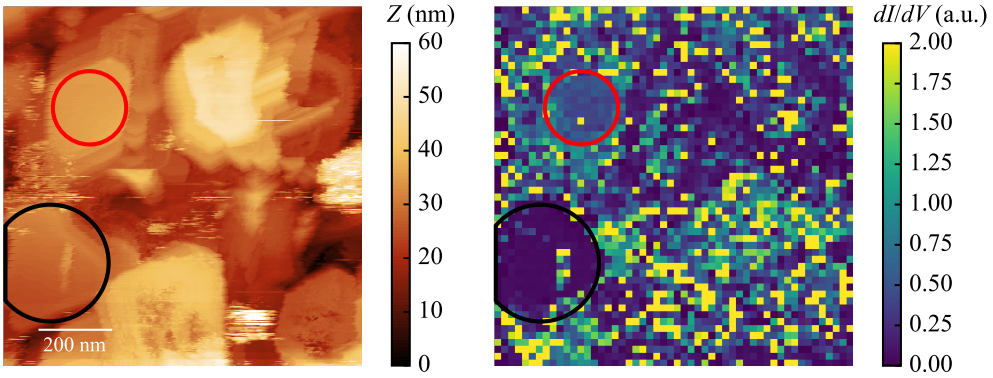

Figure 5.10: Left: 1×1 μm^2 STM image ($V_b = -5$ mV, $I_t = 1$ nA) of the tantalum carbide grains covered by graphene. **Right:** Differential conductance map at $V_b = 0$ mV at the same location. The colored circles enclose regions where the conductance is uniform and approaches 0.

local scale. Using the described process, a granular tantalum carbide layer with graphene layers on the top was grown which offers a clean and oxide-free surface to perform low-temperature STM studies. This system also allows to have more insight on the local properties of the graphene grown on TaC.

5.4.1 Granular structure characterization

Left part of Fig. 5.10 shows a large scale (1×1) μm^2 STM image of the sample showing the granularity of the underlying TaC. The grains have dimensions of about 200 nm^2 in agreement with the grains observed on the SEM image presented in Fig. 5.3. While doing the STM image, the local differential conductance dI/dV was recorded by STS for every 10 pixels. As the measurement was done at 4.2 K, the TaC should be superconducting and a drop of the differential conductance at zero bias (Fermi level) should be observed due to the presence of a superconducting gap in the local density of states of the TaC.

The resulting map of the local differential conductance for $V_b = 0$ mV is shown in the right part of Fig. 5.10. The surface may not be extremely clean as most of the recorded spectra are noisy and show abrupt changes in the dI/dV. This led to an inhomogeneous map but with several regions that show a uniform and very low differential conductance indicated by the colored circles. Reporting the circles on the STM image, we see that these regions correspond to clean flat grains. Typical normalized $dI/dV(V)$ spectra recorded in these regions are given in Fig. 5.11 (left for the black region

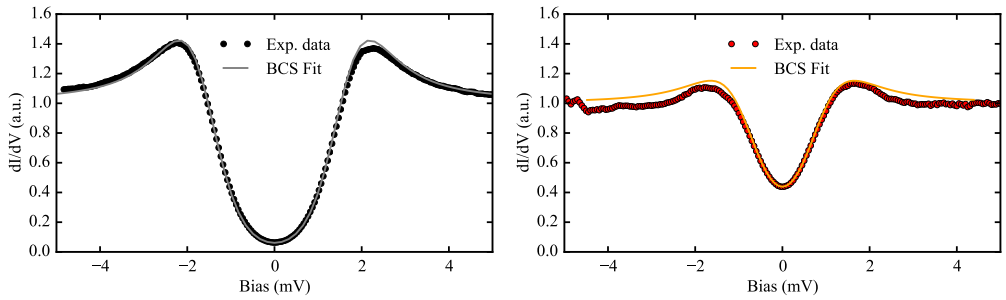

Parameters	Black	Red
Δ (meV)	1.6 ± 0.1	0.8 ± 0.1

Figure 5.11: Left: dI/dV spectrum (black dots) taken at 4.2 K in the black region of Fig. 5.10 with the BCS fit (gray solid line). **Right:** dI/dV spectrum (red dots) taken at 4.2 K in the red region of Fig. 5.10 with the BCS fit (orange solid line). **Bottom:** Parameters extracted from the BCS fit.

and right for the red region). Two different behaviors are observed as the density of states reaches almost zero in the black circled region whereas it is only reduced by half in the red circled region. To give more quantitative results, the spectra have been fitted by the BCS density of states of the superconductor with taking account for the sample temperature.

Derivation of the BCS fit function The electronic density of states in a superconductor for a given energy E is given by the BCS theory [88]:

$$N_s(E) = N_n \frac{E}{\sqrt{E^2 - \Delta^2}} \qquad \text{for } E > \Delta \tag{5.7}$$

$$N_s(E) = 0 \qquad \text{for } E < \Delta \tag{5.8}$$

where N_n is the density of states in the normal state and Δ the superconducting gap. To take into account additional pair-breaking events, an imaginary part is added to the energy so that E becomes $E + i\Gamma$. Γ, called the Dynes parameter [26], introduces in the model the finite lifetime of the quasiparticle excitations.

Recalling Eq. (2.4) without neglecting the effect of temperature, the tunnel current (shorted to I) with respect to the bias (shorted to V) is given by

$$I(V) \propto \int_{-\infty}^{\infty} N_s(E + eV) N_t(E) [f(E + eV) - f(E)] dE \,. \tag{5.9}$$

A change of variable in the integral $\epsilon = E + eV$ yields

$$I(V) \propto \int_{-\infty}^{\infty} N_s(\epsilon) N_t(\epsilon - eV)[f(\epsilon) - f(\epsilon - eV)]d\epsilon\,. \tag{5.10}$$

The derivation with respect to V to obtain the differential conductance dI/dV gives

$$dI/dV \propto \int_{-\infty}^{\infty} -eN_s(\epsilon)N_t'(\epsilon - eV)[f(\epsilon) - f(\epsilon - eV)] \\ - eN_s(\epsilon)N_t(\epsilon - eV)f'(\epsilon - eV)d\epsilon\,. \tag{5.11}$$

Under the common assumption that the tip is metallic with a constant density of states ($N_t(E) = N_t$), the differential conductance is

$$dI/dV \propto \int_{-\infty}^{\infty} -eN_s(\epsilon)N_t f'(\epsilon - eV)d\epsilon \tag{5.12}$$

and depends only on the density of states of the superconducting sample N_s given above and the derivative of the Fermi-Dirac distribution:

$$f'(\epsilon) = \frac{-1}{4k_B T \mathrm{ch}^2(\frac{\epsilon}{2k_B T})} \tag{5.13}$$

where T is the electronic temperature of the tip and k_B the Boltzmann constant. The differential conductance can therefore be computed with three fitting parameters: the electronic temperature T, the Dynes parameter Γ and finally the superconducting gap Δ.

The results of the fits are given in the table in Fig. 5.11. In both cases, the electronic temperature was set at 4.2 K, equal to the temperature at which the spectra were recorded, and the Dynes parameter to 0, as it was unnecessary to fit the spectra. The only fitting parameter is therefore the superconducting gap Δ whose results are shown in the table 5.11. The corresponding critical temperature can be deduced using the universal BCS formula [88]

$$T_c = \frac{\Delta}{1.764 k_B}\,. \tag{5.14}$$

For this black region, the deduced critical temperature $T_c^B = \Delta^B/1.764k_B = 10.5 \pm 0.5$ K corresponds to the expected critical temperature of stoichiometric TaC. As for the red region, the superconducting gap is two times smaller so that $T_c^R = \Delta^R/1.764k_B = 5.2 \pm 0.5$ K.

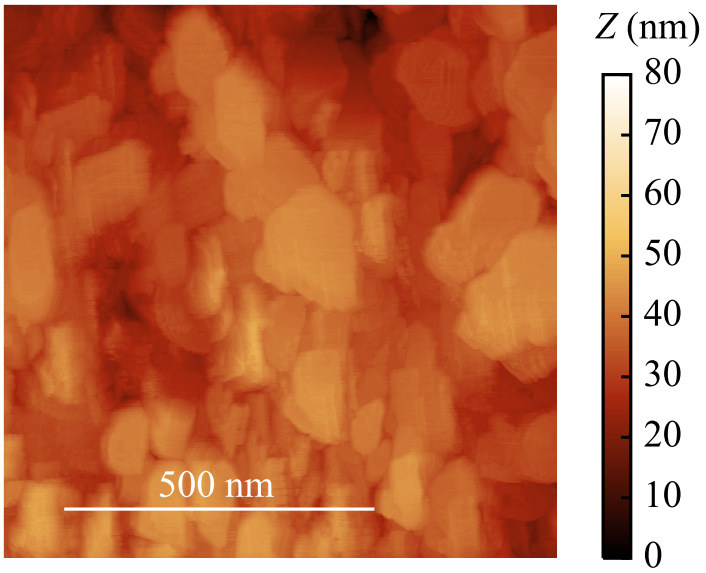

Figure 5.12: 900×900 nm^2 STM image ($V_b = -1$ V, $I_t = 600$ pA) of the TaC grains on which the temperature dependence was performed.

We can interpret the difference in critical temperature as a different composition (carbon to metal ratio) of the red grain. In Ref. 83, the authors argue that, during annealing, the carbon atoms diffuse in the tantalum by grain boundaries so that the composition of grains can be different depending on their surface-to-volume ratio. However, the growth process used in their case was different so that additional investigations are needed in our case to confirm this scenario.

Another interpretation of this superconducting gap variation from grain to grain is linked to the presence of a potential proximity effect as there are a few graphene layers that cover the TaC grains. A higher number of graphene layers on the top of the red grain would then explain the observed weakening of the superconductivity.

5.4.2 Temperature dependence of the superconducting gap

We studied the temperature dependence of the superconducting gap appearing in the STS spectra on a different location of the sample compared to the experiment described in the previous section. The STM image of this location (Fig. 5.12) showed again a granular structure. We recorded STS

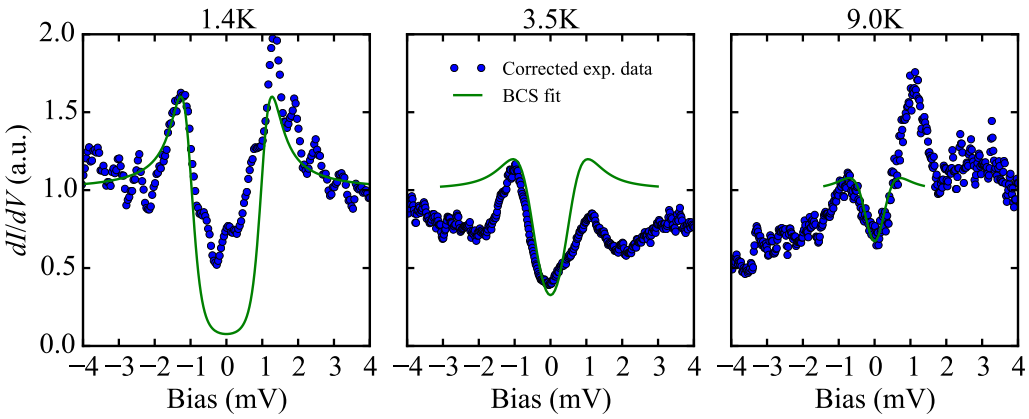

Parameters	1.4 K	3.5 K	9.0 K
Δ (meV)	1.1 ± 0.1	0.6 ± 0.1	0.3 ± 0.1
T (K)	1.4 ± 0.1	2.8 ± 0.1	2.3 ± 0.1

Figure 5.13: Top: Experimental STS spectra (blue dots) for different sample temperatures with BCS fit (green line). **Bottom:** Parameters extracted from the presented fits (Γ set to 0).

spectra at different temperatures regulated with the heater placed on the sample holder. The temperature of the sample was monitored by the thermometer also placed on the sample holder. We then were able to record spectra from 1.4 K (helium bath pumped below the lambda point) to around 10 K.

Figure 5.13 shows the experimental differential conductance for three temperatures in blue data points. The recorded spectra were not as clean as the ones of the previous section so that the BCS fits (solid line) are far from ideal for any temperature. Still, the fits allow to extract an estimate of the superconducting gap Δ as a function of the sample temperature T. This is shown in Fig. 5.14 for all the probed temperatures. The variation of the superconducting parameter Δ with temperature can be derived using the BCS theory [88]. The resulting prediction $\Delta_{BCS}(T)$ is shown in Fig. 5.14 for the expected critical temperature $T_c = 10.15$ K in solid black line. A slighty better matching is achieved by taking $T_c = 6.5$ K (black dashed line). At temperatures between 1.4 K and 5 K, there is a decrease in the experimental gap amplitude which is very roughly fitted by the BCS theory. However, the presence of a gap of around 0.5 meV at higher temperatures (around 9 K) is at odds with the abrupt decrease predicted by theory.

A possible explanation is that the data are too poor to get any meaningful results. Notably, it is very surprising to get a temperature difference of 7 K

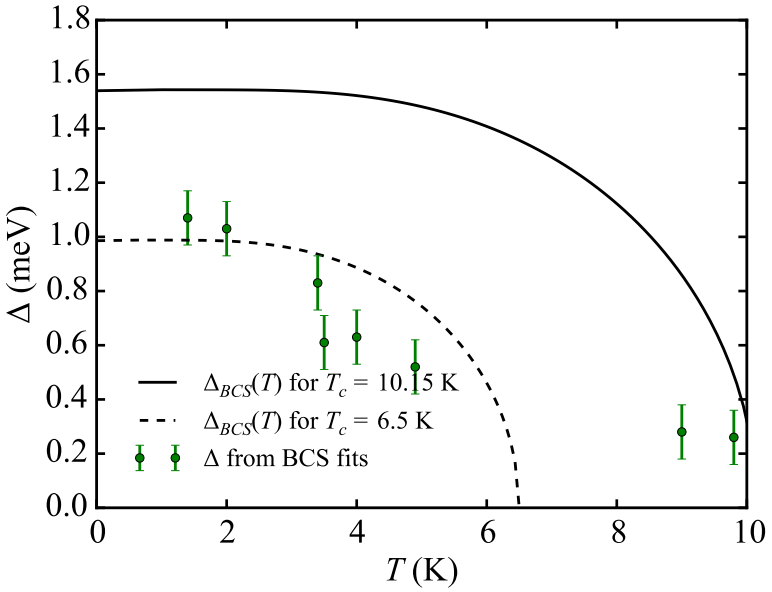

Figure 5.14: Values of the superconducting parameter Δ extracted from the BCS fits (green dots) and the prediction by BCS theory of $\Delta_{BCS}(T)$ for $T_c = 10$ K (black solid line) and $T_c = 6.5$ K (black dashed line)

between the tip and the sample for the BCS fit at 9.0 K (Fig 5.13). This casts doubt on the validity of the BCS fits at high temperatures. Another explanation is that the gap observed is induced by the superconducting proximity effect of TaC in the graphene layers. This proximity gap is not expected to follow the BCS theory and the temperature dependence should be studied in the framework of the Usadel equations which is beyond the scope of this work.

5.4.3 Moiré patterns on TaC

After having characterized the grains at the micron scale, we tried to have insight on the local structure of the graphene layers grown on TaC by doing measurements at a smaller scale.

5.4.3.a Superconducting gap

Left part of Fig. 5.15 shows a zoomed-in STM image recorded on the red grain in Fig. 5.10. The flat grain shows boundaries similarly to what was observed on graphene on silicon carbide (Fig. 3.19). More interestingly, the top part of the STM image of the grain shows moiré spots, that stop at the

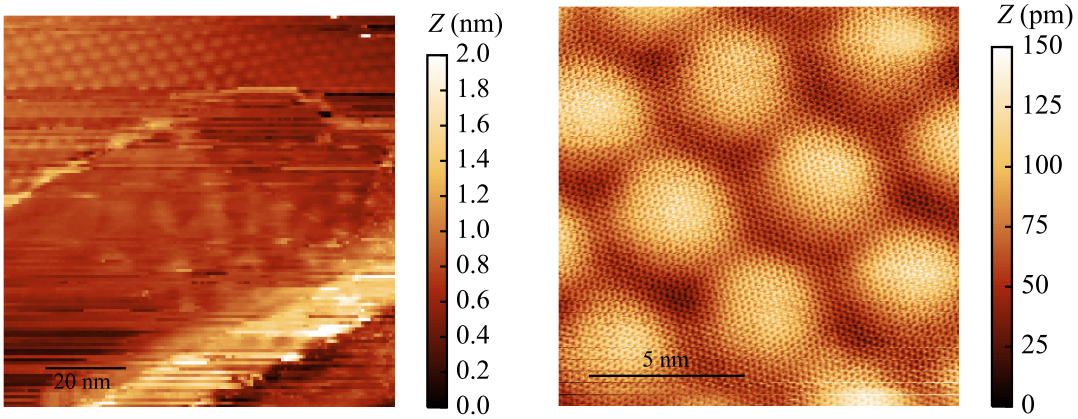

Figure 5.15: Left: 100×100 nm^2 STM image ($V_b = -50$ mV, $I_t = 1$ nA) recorded on the red grain in Fig. 5.10 showing layer boundaries and the appearance of moiré spots in the middle and upper part. **Right:** 13×13 nm^2 STM image ($V_b = -4$ mV, $I_t = 1$ nA) of the moiré pattern of the upper part.

topmost boundary, due to a misorientated stacking of two graphene layers on TaC. Similar moirés were repeatedly observed in other places on the TaC samples covered with graphene indicating that the graphene layers grow in a turbostratic fashion on TaC like on the C-face of SiC. The appearance of this stacking is an unexpected boon as it is not the most energetically favorable one and allows to decouple the graphene layers preserving their Dirac-like dispersion for large twist angles.

The right part of Fig. 5.15 shows a close-up STM image of the moiré pattern with the graphene atomic lattice. As presented previously, we can get the graphene lattice parameter a_{gr}, the twist angle θ and the moiré parameter D_m by doing a commensurability analysis. The values averaged over all directions are given below:

$$\begin{aligned} a_{gr} &= 2.464 \pm 0.004 \\ D_m &= 5.27 \pm 0.26 \text{ nm} \\ \theta &= 2.69 \pm 0.01^\circ . \end{aligned}$$

θ is above 2° so that the top graphene layer can be considered as mostly electronically decoupled from the bottom layer with van Hove singularities in the local density of states at several hundreds of millivolts above the Dirac energy. As superconductivity involves excitations on an energy scale of the superconducting gap around the Fermi energy, we do therefore not expect to have any variation of the superconducting gap at the moiré scale. Figure 5.16

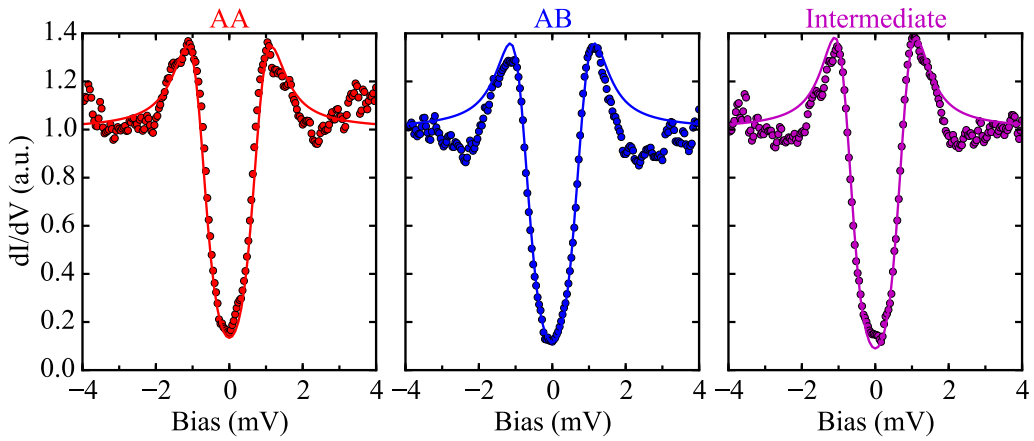

Parameters	AA	AB	Intermediate
Δ (meV)	0.82 ± 0.05	0.83 ± 0.05	0.81 ± 0.05
Γ (meV)	0.041 ± 0.008	0.025 ± 0.008	0.008 ± 0.008

Figure 5.16: Top: Experimental dI/dV spectra recorded at 2.2 K ($V_b = -4$ mV, $I_t = 1$ nA) in different regions of the moiré (dots) with their corresponding BCS fit (solid line). **Bottom:** Parameters extracted from the BCS fit for the different regions.

shows that it is the case as dI/dV spectra recorded on different places of the moiré (AA, AB and intermediate regions) do not deviate strongly from each other. The BCS fit gives superconducting gaps Δ of around 0.8 meV as observed in the large-scale characterization of the grain. These spectra were recorded with the helium-4 bath cooled to the lambda point ($T = 2.2$ K) which was set as the electronic temperature for the BCS fitting functions. The Γ values obtained are still rather small compared to the superconducting gap.

5.4.3.b Van Hove singularities

As for now, we made the hypothesis that the moiré was occuring due to a twist angle between the two top graphene layers. The atomic resolution shows that the top layer is indeed graphene but moirés can be also observed by STM when a single graphene layer lies on a mismatched substrate (metal, hBN...). To be able to make the distinction, we searched for low-energy van Hove singularities that would only appear in the LDOS when the moiré is composed of twisted graphene layers.

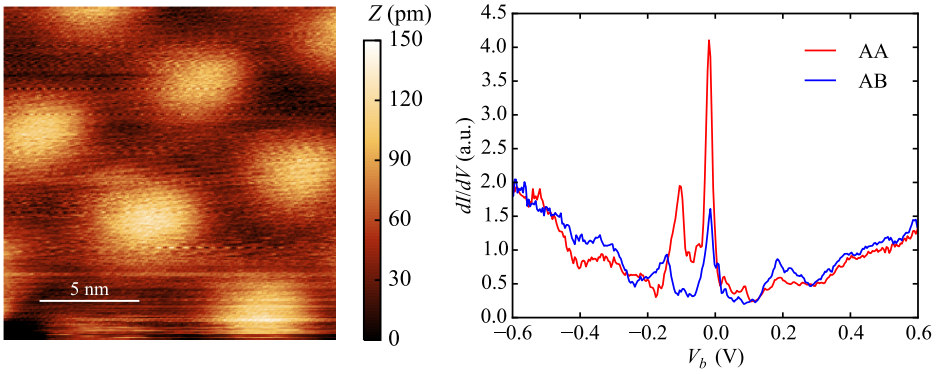

Figure 5.17: Left: 16×16 nm^2 STM image ($V_b = -1$ V, $I_t = 1$ nA) of a moiré found on a TaC grain. The angle between the layers is estimated to be $\theta = 2.0°$. **Right:** dI/dV spectra recorded in the AA region (red) and AB region (blue) of the moiré

Moiré 2° To check the presence of van Hove singularities, the LDOS of a moiré system needs to be probed at much higher energies than the superconducting gap. This was done on the moiré shown in the left part of Fig. 5.17 found on the top of another TaC grain. The commensurability analysis of the moiré gives a slight biaxial deformation ($\varepsilon_b = -0.12\%$) with no uniaxial deformation. The graphene lattice parameter a_{gr} and the moiré parameter D_m are therefore uniform and given by

$$\begin{aligned} a_{gr} &= 2.458 \pm 0.004 \\ D_m &= 7.03 \pm 0.46 \text{ nm} \\ \theta &= 2.00 \pm 0.01° . \end{aligned}$$

The STS spectra recorded in the AA and AB regions on this moiré are shown in the right part of Fig. 5.17. Both show two well-defined peaks separated by $\Delta E = 123 \pm 10$ meV. This is very close from the expected separation $\Delta E_{vHs} = 159 \pm 1$ meV given by tight-binding calculations on the unstrained bilayer (16,17) ($\theta_{16,17} = 2.00°$). Moreover, the peaks are more intense in AA regions than in AB regions as expected for moirés of small angle (2° and lower) where the van Hove singularities localize in AA regions. This proves that the observed moiré is composed of two twisted graphene layers.

Moiré 7.25° The conclusion that the moiré is composed of twisted graphene layers is supported by the study of another moiré found on another TaC grain shown in the left part of Fig. 5.18. The relative strain levels are again deduced by a commensurability analysis of the moiré which gives a very small

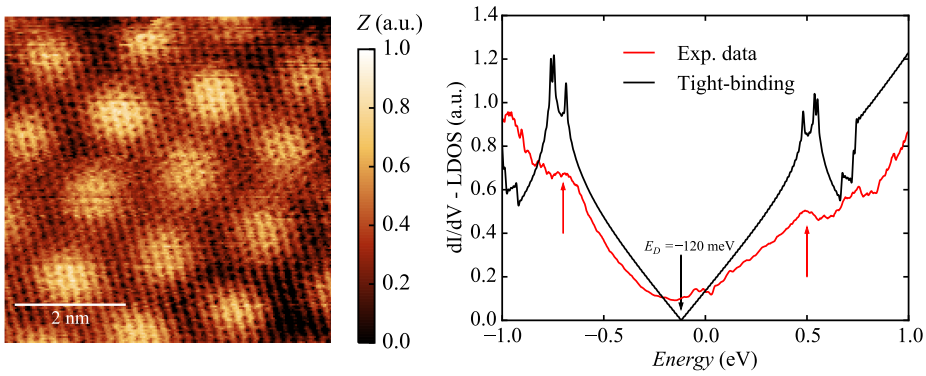

Figure 5.18: Left: 6×6 nm^2 STM image ($V_b = -1$ V, $I_t = 500$ pA) of a moiré found on a TaC grain. The angle between the layers is estimated to $\theta = 7.25°$. Z is in arbitrary units due to a corrupted calibration file. **Right:** dI/dV spectra recorded in the moiré (red) showing broad van Hove singularities (red arrows) and tight-binding calculations performed on the strained commensurate structure (black).

biaxial compression ($\varepsilon_b = -0.04\%$) but a non-negligible uniaxial deformation of $\varepsilon_u = 0.62\%$. The averaged structural parameters are then

$$\begin{aligned} a_{gr} &= 2.468 \pm 0.008 \\ D_m &= 1.95 \pm 0.46 \text{ nm} \\ \theta &= 7.25 \pm 0.01° \,. \end{aligned}$$

No localization effect are expected for this angle so that the LDOS is the same in any point of the moiré. The dI/dV spectrum recorded on the moiré is shown in red in the right panel of Fig. 5.18. The dI/dV shows broad peaks that are underlined by red arrows.

We then compare this data with the tight-binding calculations on the commensurate structure (black curve). As uniaxial strain is taken into account, multiple van Hove singularities appear in the calculation as shown in Chapter 3. Although there are no direct observation of these multiple singularities in the experimental data, the mean separation between them is well reproduced by the broadening of the experimental peaks hinting that the experimental data is not resolved enough to observe this multiplicity. The energy of the experimental peaks is also in excellent agreement with the calculation assuming a n-doping of $E_D = -120$ meV which strongly supports that these are van Hove singularities of twisted graphene layers. The origin of this doping is unclear and would need detailed investigations of the charge transfer at the TaC/graphene interface.

5.5 Conclusion

It was demonstrated that the graphene on superconducting TaC is a promising system to study induced superconductivity in graphene layers. The original growth process notably yields a high-quality superconducting TaC layer with a high critical temperature and a good electrical coupling to graphene. Achieving fine control of the growth would be helpful for further studies of the superconducting proximity effect by realizing different types of TaC/graphene interfaces for example. It could also give insight on the observed turbostratic stacking of graphene on the TaC and the nature of the graphene-TaC interface.

CONCLUSION AND PERSPECTIVES

The strong link between the structural parameters and the electronic properties of twisted graphene layers was explored in this manuscript. The introductory Chapter 1 showed that the link is quite important in monolayer graphene, the crystallographic structure leading to the apparition of another electronic degree of freedom. This is even more relevant in twisted graphene layers where the apparition of the moiré pattern leads to a strong dependence of the electronic properties with respect to the twist angle between the layers. This calls for a tool to accurately study experimental moiré patterns under the form of the presented commensurability analysis.

The commensurability analysis is notably the only way to evidence relative strain in the layers. The relative strain modifies strongly the electronic properties of twisted graphene layers as shown in Chapter 3. It is expected that this method could be useful in the studies of other stackings of 2D materials to take into account previously unaccessible structural details. More generally, relative strain could be used to tune efficiently the properties of such heterostructures.

A first step towards this was presented in Chapter 4 which showed possibilities of an active modification of the electronic and mechanical properties of moirés of graphene by local interactions between the tip and the graphene surface. Several regimes of interaction were shown to occur with an elastic regime, well-described by a simple spring model, and a non-elastic regime that depends on the electronic properties of the graphene system. A fine manipulation of the observed periodic instability would be very interesting to design a self-assembled superlattice of mechanical switches whose periodicity could be tuned by the twist angle between the layers. Such control is difficult to achieve in our setup as the interaction is probably mediated by a contaminating layer. It would be interesting to reproduce the experiment

in a Ultra-High-Vacuum setup to avoid contamination and see if the same effects can be observed. The interpretation of the measurement was also made difficult by the complex spectroscopic signature of the studied moiré system. Reproducing the experiment on an other moiré, of higher twist angle for example, could give more insight on the phenomena at work.

The change of the electronic properties of graphene by the underlying substrate is also a promising route. This was shown in Chapter 5 where a superconducting proximity effect in moirés of graphene induced by the underlying tantalum carbide was observed. While the geometry led to a efficient coupling between the tantalum carbide and the graphene, it prevents a complete study of the superconducting proximity effect. It would be ideal to observe to weakening of the proximity effect by increasing the distance between the probed graphene and the superconducting interface. For this purpose, some samples were designed to show a planar interface between tantalum carbide and graphene. It was however difficult to locate the interface by STM and the measurements did not yield significant results for now. Continuing such experiments would help in the interpretation of the presented results. It would also be another step towards the realization of Andreev billards, normal metal islands surrounded by a superconductor, to study the interplay of superconductivity and ballistic transport.

CONCLUSION ET PERSPECTIVES

Le lien fort existant entre la structure et les propriétés électroniques des couches tournées de graphène a été étudié dans ce manuscrit. Le chapitre 1 introductif a montré que ce lien est déjà très fort dans le graphène monocouche avec l'apparition d'un nouveau dégré de liberté électronique due à la structure cristallographique. L'étude de ce lien est encore plus pertinente dans le cas des couches tournées de graphène où l'apparition d'un moiré donne lieu à une forte dépendence des propriétés électroniques avec l'angle entre les couches. Cette étude requiert un outil pour étudier très précisément les moirés expérimentaux qui est l'analyse de commensurabilité présentée dans ce même chapitre.

L'analyse de commensurabilité est notablement la seule manière de mettre en évidence une déformation relative dans les couches. Le chapitre 3 montre que la présence d'une déformation relative modifie très fortement les propriétés électroniques des couches tournées de graphène. Notons que cette méthode pourrait être utile dans l'étude d'autres empilements de matériaux 2D pour prendre en compte des détails de leur structure autrement inaccessibles. D'une manière plus générale, la déformation relative pourrait être utilisée pour changer de manière efficace et contrôlée les propriétés de telles hétérostructures.

Une première étape d'une telle utilisation contrôlée de la déformation a été présentée dans le chapitre 4. Ce chapitre décrit la possibilité de modifier activement les propriétés mécaniques et électroniques des moirés de graphène grâce aux interactions locales entre la pointe et le graphène en surface. Plusieurs régimes d'interactions apparaissent : un régime élastique, pouvant être simplement modélisé avec des ressorts, et un régime non-élastrique qui fait intervenir les propriétés électroniques du système. Une manipulation adroite de l'instabilité périodique observée serait très intéressante pour con-

cevoir un réseau d'interrupteurs mécaniques auto-assemblés dont la périodicité pourrait être réglée par l'angle entre les couches. Un tel contrôle est difficile dans notre système expérimental car l'interaction est probablement transmise par une couche de contaminants. Il serait intéressant de reproduire ces expériences dans une installation Ultra-Haut-Vide pour éviter toute contamination and voir si les mêmes effets peuvent être observés. L'interprétation des mesures a été de plus rendue difficile par la signature spectroscopique complexe du moiré étudié. Reproduire l'expérience avec un autre moiré, avec un angle entre les couches plus important, pourrait donner plus d'informations sur les phénomènes mis en jeu.

La modification des propriétés électroniques du graphène par le substrat est également une voie prometteuse. Ceci fut décrit dans le chapitre 5 où un effet de proximité supraconducteur induit par un substrat de carbure de tantale a été observé dans des moirés de graphène. Bien que la géometrie mène à un couplage efficace entre le carbure de tantale et le graphène, elle empêche une étude complète de l'effet de proximité supraconducteur. Il serait en effet idéal d'observer l'affaiblissement de l'effet de proximité en fonction de la distance entre le graphène sondé et l'interface supraconductrice. Pour cela, plusieurs échantillons ont été conçus de manière à avoir une interface plane entre le carbure de tantale et le graphène. Il a été cependant difficile de localiser l'interface par STM and les mesures n'ont pas donné de résultats significatifs pour le moment. Continuer ces expériences pourrait aider dans l'interprétation des résultats présentés. Ce serait également un nouvelle étape vers la réalisation de billards d'Andreev, des ilôts de métal normal entourés par un supraconducteur, pour étudier l'interaction entre la supraconductivité et le transport ballistique.

APPENDIX A

COMMENSURABILITY ANALYSES OF THE MOIRÉS IN CHAPTER 5

In the following, we present the commensurability analyses of the three moiré structures discussed in Chapter 5 that make use of the general formulas introduced in Chapter 1.

A.1 Moiré shown Fig. 5.15: $\theta = 2.69°$

The commensurability analysis of the moiré shown in Fig. 5.15 gives the following decomposition in the basis of beating reciprocal vectors:

$$\mathbf{k_{t_1}} = 24\mathbf{k_{beat_1}} - 11\mathbf{k_{beat_2}} \tag{A.1}$$
$$\mathbf{k_{t_2}} = 13\mathbf{k_{beat_1}} + 13\mathbf{k_{beat_2}} \tag{A.2}$$
$$\mathbf{k_{b_1}} = 24\mathbf{k_{beat_1}} - 12\mathbf{k_{beat_2}} \tag{A.3}$$
$$\mathbf{k_{b_2}} = 14\mathbf{k_{beat_1}} + 12\mathbf{k_{beat_2}}\,. \tag{A.4}$$

As we get integer coordinates in the basis of the beating reciprocal vectors, the beating coincides with the full moiré periodicity. The moiré vectors are then the beating vectors. Using the decomposition of Eq. (1.27), the commensurability indices are therefore directly read:

i=24	k=-11	m=24	q=-12
j=13	l=13	n=14	r=12

Using Eq. (1.29), the structural relation between the top and the bottom

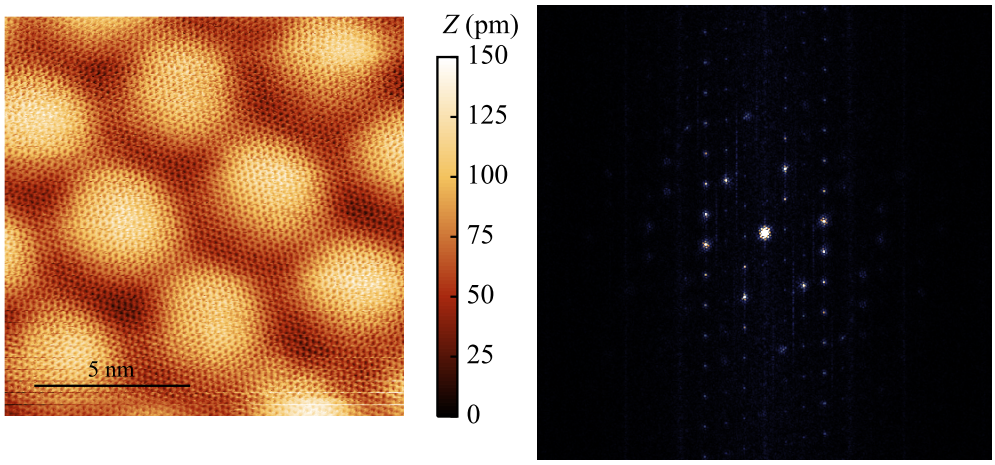

Figure A.1: STM image and its Fourier transform used for the commensurability analysis of moiré shown Fig. 5.15

layer, given by the Park-Madden matrix, is

$$\begin{pmatrix} \mathbf{a_{t_1}} \\ \mathbf{a_{t_2}} \end{pmatrix} = \frac{1}{455} \begin{pmatrix} 468 & 26 \\ -24 & 442 \end{pmatrix} \begin{pmatrix} \mathbf{a_{b_1}} \\ \mathbf{a_{b_2}} \end{pmatrix} \tag{A.5}$$

which gives, in terms of the extended Wood's notation (Eq. 1.34)

$$(P_1 R\theta_1 \times P_2 R\theta_2) = (1.00122R2.833 \times 0.99885R2.621)\,. \tag{A.6}$$

The mean angle between the layers falls directly from this relation:

$$\theta = 2.69° \tag{A.7}$$

To find the moiré parameter D_m, the commensurability indices are plugged in Eq. 1.25 to deduce $\mathbf{a_{m_1}}$ and $\mathbf{a_{m_2}}$. For the case considered here, The mean moiré parameter is then

$$D_m = 5.27 \text{ nm}\,. \tag{A.8}$$

The relative strain between the layers is then given by Eqs. 1.36 and 1.36:

$$\varepsilon_{uni} = 0.51\% \tag{A.9}$$
$$\varepsilon_{bi} = -0.14\%. \tag{A.10}$$

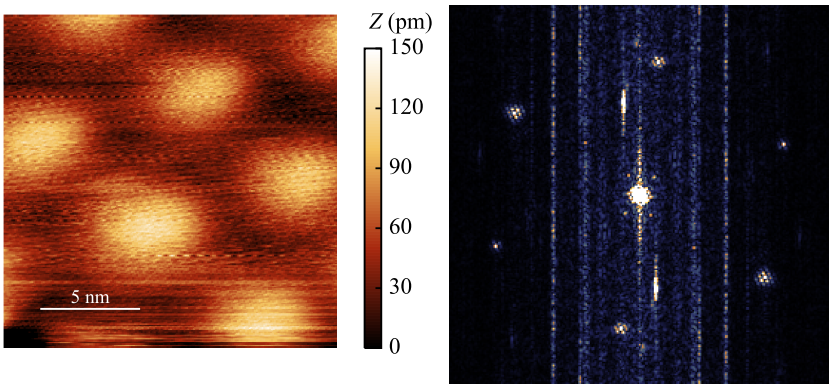

Figure A.2: STM image and its Fourier transform used for the commensurability analysis of moiré shown in Fig. 5.17

A.2 Moiré shown in Fig. 5.17: $\theta = 2.00°$

The commensurability analysis of the moiré shown in Fig. 5.17 gives the following decomposition in the basis of the beating reciprocal vectors:

$$\mathbf{k_{t_1}} = 15\mathbf{k_{beat_1}} + 18\mathbf{k_{beat_2}} \tag{A.11}$$
$$\mathbf{k_{t_2}} = -18\mathbf{k_{beat_1}} + 33\mathbf{k_{beat_2}} \tag{A.12}$$
$$\mathbf{k_{b_1}} = 16\mathbf{k_{beat_1}} + 17\mathbf{k_{beat_2}} \tag{A.13}$$
$$\mathbf{k_{b_2}} = -17\mathbf{k_{beat_1}} + 33\mathbf{k_{beat_2}}\,. \tag{A.14}$$

As we get integer coordinates in the basis of the beating reciprocal vectors, the beating coincides with the full moiré periodicity. The moiré vectors are then the beating vectors. The commensurability indices are therefore

i=15	k=18	m=16	q=17
j=-18	l=33	n=-17	r=33

The structural relation between the top and the bottom layer, given by the Park-Madden matrix, is

$$\begin{pmatrix} \mathbf{a_{t_1}} \\ \mathbf{a_{t_2}} \end{pmatrix} = \frac{1}{819} \begin{pmatrix} 834 & 33 \\ -33 & 801 \end{pmatrix} \begin{pmatrix} \mathbf{a_{b_1}} \\ \mathbf{a_{b_2}} \end{pmatrix} \tag{A.15}$$

which gives, in terms of the extended Wood's notation

$$(P_1 R\theta_1 \times P_2 R\theta_2) = (0.99878R2.002 \times 0.99878R2.002)\,. \tag{A.16}$$

Here, the moiré is fully isotropic so that the angle between the layers and the moiré parameter are

$$\theta = 2.002° \tag{A.17}$$
$$D_m = 7.03 \text{ nm}\,. \tag{A.18}$$

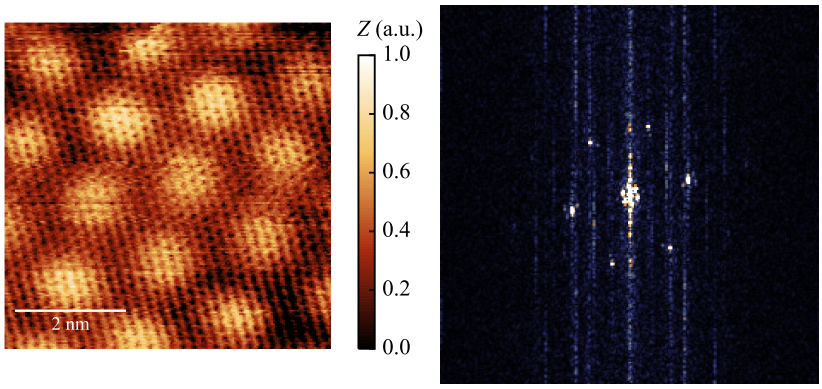

Figure A.3: STM image and its Fourier transform used for the commensurability analysis of moiré shown in Fig. 5.18

The relative strain between the layer is given by

$$\varepsilon_{uni} = 0.\% \tag{A.19}$$
$$\varepsilon_{bi} = -0.012\% \tag{A.20}$$

A.3 Moiré shown in Fig. 5.18: $\theta = 7.25°$

The commensurability analysis of the moiré shown in Fig. 5.18 gives the following decomposition in the basis of the beating reciprocal vectors:

$$\mathbf{k_{t_1}} = 9\mathbf{k_{m_1}} - (3 + \frac{2}{3})\mathbf{k_{m_2}} \tag{A.21}$$
$$\mathbf{k_{t_2}} = 4\mathbf{k_{m_1}} + (5 + \frac{1}{3})\mathbf{k_{m_2}} \tag{A.22}$$
$$\mathbf{k_{b_1}} = 9\mathbf{k_{m_1}} - (4 + \frac{2}{3})\mathbf{k_{m_2}} \tag{A.23}$$
$$\mathbf{k_{b_2}} = 5\mathbf{k_{m_1}} + (4 + \frac{1}{3})\mathbf{k_{m_2}}\,. \tag{A.24}$$

As we have fractional coordinates in the basis of the beating reciprocal vectors, the beating does not coincide with the full periodicity of the moiré. The moiré reciprocal vectors are then given by $k_{beat_1} = 3k_{m_1}$ and $k_{beat_1} = 3k_{m_2}$ to have the following integer decomposition in the basis of the moiré reciprocal

vectors:

$$\mathbf{k_{t_1}} = 27\mathbf{k_{m_1}} - 11\mathbf{k_{m_2}} \tag{A.25}$$
$$\mathbf{k_{t_2}} = 12\mathbf{k_{m_1}} + 16\mathbf{k_{m_2}} \tag{A.26}$$
$$\mathbf{k_{b_1}} = 27\mathbf{k_{m_1}} - 14\mathbf{k_{m_2}} \tag{A.27}$$
$$\mathbf{k_{b_2}} = 15\mathbf{k_{m_1}} + 13\mathbf{k_{m_2}}\,. \tag{A.28}$$

In direct space, it means that the moiré cell spans 3 beatings in the first direction $a_{m_1} = 3a_{beat_1}$ and 3 beatings and the second direction $a_{m_2} = 3a_{beat_2}$. The commensurability indices are then

i=27	k=-11	m=27	q=-14
j=12	l=16	n=-14	r=13

The structural relation between the top and the bottom layer, given by the Park-Madden matrix, is

$$\begin{pmatrix} \mathbf{a_{t_1}} \\ \mathbf{a_{t_2}} \end{pmatrix} = \frac{1}{561} \begin{pmatrix} 516 & -84 \\ 81 & 600 \end{pmatrix} \begin{pmatrix} \mathbf{a_{b_1}} \\ \mathbf{a_{b_2}} \end{pmatrix} \tag{A.29}$$

which gives, in terms of the extended Wood's notation

$$(P_1 R\theta_1 \times P_2 R\theta_2) = (1.00307R52.572 \times 1.00513R52.854)\,. \tag{A.30}$$

The mean angle between the layers and the mean moiré parameter are

$$\theta = 7.25^\circ \tag{A.31}$$
$$D_m = 1.95 \text{ nm}\,. \tag{A.32}$$

The relative strain between the layer is given by

$$\varepsilon_{uni} = 0.62\% \tag{A.33}$$
$$\varepsilon_{bi} = -0.04\% \tag{A.34}$$

BIBLIOGRAPHY

[1] Draw Freely | Inkscape. http://inkscape.org/en/.

[2] PT10 - Bruker AFM Probes. http://www.brukerafmprobes.com/p-3439-pt10.aspx.

[3] T. R. Albrecht, H. A. Mizes, J. Nogami, Sang-il Park, and C. F. Quate. Observation of tilt boundaries in graphite by scanning tunneling microscopy and associated multiple tip effects. Appl. Phys. Lett., 52(5):362, 1988.

[4] S J Altenburg and R Berndt. Local work function and STM tip-induced distortion of graphene on Ir(111). New J. Phys., 16(5):053036, May 2014.

[5] B. Amorim, A. Cortijo, F. de Juan, A.G. Grushin, F. Guinea, A. Gutiérrez-Rubio, H. Ochoa, V. Parente, R. Roldán, P. San-Jose, J. Schiefele, M. Sturla, and M.A.H. Vozmediano. Novel effects of strains in graphene and other two dimensional materials. Phys. Rep., 617:1–54, March 2016.

[6] A. Artaud, L. Magaud, T. Le Quang, V. Guisset, P. David, C. Chapelier, and J. Coraux. Universal classification of twisted, strained and sheared graphene moiré superlattices. Sci. Rep., 6:25670, May 2016.

[7] Alexandre Artaud. Quasi-Ordre à Longue Distance et Défauts Topologiques Dans Le Graphène Sur Rhénium Étudié Par Microscopie à Effet Tunnel. PhD thesis, Université Grenoble Alpes, 2017.

[8] D. V. Badami. X-Ray studies of graphite formed by decomposing silicon carbide. Carbon, 3(1):53–57, July 1965.

[9] Thomas E. Beechem, Taisuke Ohta, Bogdan Diaconescu, and Jeremy T. Robinson. Rotational Disorder in Twisted Bilayer Graphene. ACS Nano, 8(2):1655–1663, February 2014.

[10] J. D. Bernal. The Structure of Graphite. Proc. R. Soc. Lond. Ser. Contain. Pap. Math. Phys. Character, 106(740):749–773, 1924.

[11] H. Beyer, M. Müller, and Th Schimmel. Monolayers of graphite rotated by a defined angle: Hexagonal superstructures by STM. Appl. Phys. Mater. Sci. Process., 68(2):163–166, 1999.

[12] G. Binnig. Tunneling through a controllable vacuum gap. Appl. Phys. Lett., 40(2):178, 1982.

[13] Rafi Bistritzer and Allan H. MacDonald. Moiré bands in twisted double-layer graphene. Proc. Natl. Acad. Sci., 108(30):12233–12237, 2011.

[14] O. L. Blakslee, D. G. Proctor, E. J. Seldin, G. B. Spence, and T. Weng. Elastic Constants of Compression-Annealed Pyrolytic Graphite. J. Appl. Phys., 41(8):3373–3382, July 1970.

[15] I. Brihuega, P. Mallet, H. González-Herrero, G. Trambly de Laissardière, M. M. Ugeda, L. Magaud, J. M. Gómez-Rodríguez, F. Ynduráin, and J.-Y. Veuillen. Unraveling the Intrinsic and Robust Nature of van Hove Singularities in Twisted Bilayer Graphene by Scanning Tunneling Microscopy and Theoretical Analysis. Phys. Rev. Lett., 109(19), November 2012.

[16] J. M. Campanera, G. Savini, I. Suarez-Martinez, and M. I. Heggie. Density functional calculations on the intricacies of Moiré patterns on graphite. Phys. Rev. B, 75(23), June 2007.

[17] Jérôme Cayssol. Introduction to Dirac materials and topological insulators. Comptes Rendus Phys., 14(9–10):760–778, November 2013.

[18] Jae-Young Choi. Graphene transfer: A stamp for all substrates. Nat. Nanotechnol., 8(5):311–312, May 2013.

[19] Zhao-Dong Chu, Wen-Yu He, and Lin He. Coexistence of van Hove singularities and superlattice Dirac points in a slightly twisted graphene bilayer. Phys. Rev. B, 87(15), April 2013.

[20] J.H. Coombs and J.B. Pethica. Properties of vacuum tunneling currents: Anomalous barrier heights. IBM J. Res. Dev., 30(5):455–459, September 1986.

[21] A. Das, S. Pisana, B. Chakraborty, S. Piscanec, S. K. Saha, U. V. Waghmare, K. S. Novoselov, H. R. Krishnamurthy, A. K. Geim, A. C. Ferrari, and A. K. Sood. Monitoring dopants by Raman scattering in an electrochemically top-gated graphene transistor. Nat. Nanotechnol., 3(4):210–215, April 2008.

[22] Walt A de Heer, Claire Berger, Xiaosong Wu, Mike Sprinkle, Yike Hu, Ming Ruan, Joseph A Stroscio, Phillip N First, Robert Haddon, Benjamin Piot, Clément Faugeras, Marek Potemski, and Jeong-Sun Moon. Epitaxial graphene electronic structure and transport. J. Phys. Appl. Phys., 43(37):374007, September 2010.

[23] Fernando de Juan, Mauricio Sturla, and María A. H. Vozmediano. Space Dependent Fermi Velocity in Strained Graphene. Phys. Rev. Lett., 108(22):227205, May 2012.

[24] C. R. Dean, A. F. Young, I. Meric, C. Lee, L. Wang, S. Sorgenfrei, K. Watanabe, T. Taniguchi, P. Kim, K. L. Shepard, and J. Hone. Boron nitride substrates for high-quality graphene electronics. Nat. Nanotechnol., 5(10):722–726, October 2010.

[25] Vincent E. Dorgan, Myung-Ho Bae, and Eric Pop. Mobility and saturation velocity in graphene on SiO2. Appl. Phys. Lett., 97(8):082112, August 2010.

[26] R. C. Dynes, V. Narayanamurti, and J. P. Garno. Direct Measurement of Quasiparticle-Lifetime Broadening in a Strong-Coupled Superconductor. Phys. Rev. Lett., 41(21):1509–1512, November 1978.

[27] C. Faugeras, M. Amado, P. Kossacki, M. Orlita, M. Kühne, A. A. L. Nicolet, Yu. I. Latyshev, and M. Potemski. Magneto-Raman Scattering of Graphene on Graphite: Electronic and Phonon Excitations. Phys. Rev. Lett., 107(3):036807, July 2011.

[28] Andrea C. Ferrari and Denis M. Basko. Raman spectroscopy as a versatile tool for studying the properties of graphene. Nat. Nanotechnol., 8(4):235–246, April 2013.

[29] H. J. Fink, A. C. Thorsen, Earl Parker, Victor F. Zackay, and Lou Toth. High-Field Superconductivity of Carbides. Phys. Rev., 138(4A):A1170–A1173, May 1965.

[30] Øystein Fischer, Martin Kugler, Ivan Maggio-Aprile, Christophe Berthod, and Christoph Renner. Scanning tunneling spectroscopy of high-temperature superconductors. Rev. Mod. Phys., 79(1):353–419, March 2007.

[31] L. M. Foster, G. Long, and H. C. Stumpf. Production of graphite single crystals by the thermal decomposition of aluminum carbide. Am Miner., 43:285–296, 1958.

[32] Yang Gan, Wuyang Chu, and Lijie Qiao. STM investigation on interaction between superstructure and grain boundary in graphite. Surf. Sci., 539(1-3):120–128, August 2003.

[33] J. Garbarz, E. Lacaze, G. Faivre, S. Gauthier, and M. Schott. Dislocation networks in graphite: A scanning tunnelling microscopy study. Philos. Mag. A, 65(4):853–861, April 1992.

[34] A. K. Geim and I. V. Grigorieva. Van der Waals heterostructures. Nature, 499(7459):419–425, July 2013.

[35] Alexander Georgi, Peter Nemes-Incze, Ramon Carrillo-Bastos, Daiara Faria, Silvia Viola Kusminskiy, Dawei Zhai, Martin Schneider, Dinesh Subramaniam, Torge Mashoff, Nils M. Freitag, Marcus Liebmann, Marco Pratzer, Ludger Wirtz, Colin R. Woods, Roman V. Gorbachev, Yang Cao, Kostya S. Novoselov, Nancy Sandler, and Markus Morgenstern. Tuning the Pseudospin Polarization of Graphene by a Pseudomagnetic Field. Nano Lett., February 2017.

[36] A. L. Giorgi, E. G. Szklarz, E. K. Storms, Allen L. Bowman, and B. T. Matthias. Effect of Composition on the Superconducting Transition Temperature of Tantalum Carbide and Niobium Carbide. Phys. Rev., 125(3):837–838, February 1962.

[37] J. González. Magnetic and Kohn-Luttinger instabilities near a Van Hove singularity: Monolayer versus twisted bilayer graphene. Phys. Rev. B, 88(12):125434, September 2013.

[38] Robin W. Havener, Houlong Zhuang, Lola Brown, Richard G. Hennig, and Jiwoong Park. Angle-Resolved Raman Imaging of Interlayer

Rotations and Interactions in Twisted Bilayer Graphene. Nano Lett., 12(6):3162–3167, June 2012.

[39] W.A. Hofer, A. Garcia-Lekue, and H. Brune. The role of surface elasticity in giant corrugations observed by scanning tunneling microscopes. Chem. Phys. Lett., 397(4-6):354–359, October 2004.

[40] J. D. Hunter. Matplotlib: A 2D Graphics Environment. Comput. Sci. Eng., 9(3):90–95, May 2007.

[41] Kazuyuki Ito, Takamasa Ogata, Tadashi Sakai, and Yuji Awano. Ultralow contact resistivity in annealed titanium edge contacts for multilayered graphene. Appl. Phys. Express, 8(2):025101, January 2015.

[42] B. D. Josephson. Possible new effects in superconductive tunnelling. Phys. Lett., 1(7):251–253, July 1962.

[43] Kyounghwan Kim, Ashley DaSilva, Shengqiang Huang, Babak Fallahazad, Stefano Larentis, Takashi Taniguchi, Kenji Watanabe, Brian J. LeRoy, Allan H. MacDonald, and Emanuel Tutuc. Tunable Moir\'e Bands and Strong Correlations in Small-Twist-Angle Bilayer Graphene. arXiv:1703.00888 [cond-mat], March 2017.

[44] Kyounghwan Kim, Ashley DaSilva, Shengqiang Huang, Babak Fallahazad, Stefano Larentis, Takashi Taniguchi, Kenji Watanabe, Brian J. LeRoy, Allan H. MacDonald, and Emanuel Tutuc. Tunable moiré bands and strong correlations in small-twist-angle bilayer graphene. Proc. Natl. Acad. Sci., 114(13):3364–3369, March 2017.

[45] B. Kumar, M. Baraket, M. Paillet, J.-R. Huntzinger, A. Tiberj, A.G.M. Jansen, L. Vila, M. Cubuku, C. Vergnaud, M. Jamet, G. Lapertot, D. Rouchon, A.-A. Zahab, J.-L. Sauvajol, L. Dubois, F. Lefloch, and F. Duclairoir. Growth protocols and characterization of epitaxial graphene on SiC elaborated in a graphite enclosure. Phys. E Low-Dimens. Syst. Nanostructures, 75:7–14, January 2016.

[46] Michiko Kusunoki, Wataru Norimatsu, Jianfeng Bao, Koichi Morita, and Ulrich Starke. Growth and Features of Epitaxial Graphene on SiC. J. Phys. Soc. Jpn., 84(12):121014, October 2015.

[47] M. Kuwabara, D. R. Clarke, and D. A. Smith. Anomalous superperiodicity in scanning tunneling microscope images of graphite. Appl. Phys. Lett., 56(24):2396, 1990.

[48] T. Le Quang, L. Huder, F. Lipp Bregolin, A. Artaud, H. Okuno, N. Mollard, S. Pouget, G. Lapertot, A.G.M. Jansen, F. Lefloch, E.F.C. Driessen, C. Chapelier, and V.T. Renard. Epitaxial electrical contact to graphene on SiC. Carbon, 121:48–55, September 2017.

[49] C. Lee, X. Wei, J. W. Kysar, and J. Hone. Measurement of the Elastic Properties and Intrinsic Strength of Monolayer Graphene. Science, 321(5887):385–388, July 2008.

[50] Guohong Li, A. Luican, J. M. B. Lopes dos Santos, A. H. Castro Neto, A. Reina, J. Kong, and E. Y. Andrei. Observation of Van Hove singularities in twisted graphene layers. Nat. Phys., 6(2):109–113, November 2009.

[51] Guohong Li, Adina Luican, and Eva Y. Andrei. Scanning Tunneling Spectroscopy of Graphene on Graphite. Phys. Rev. Lett., 102(17), April 2009.

[52] Xuelei Liang, Brent A. Sperling, Irene Calizo, Guangjun Cheng, Christina Ann Hacker, Qin Zhang, Yaw Obeng, Kai Yan, Hailin Peng, Qiliang Li, Xiaoxiao Zhu, Hui Yuan, Angela R. Hight Walker, Zhongfan Liu, Lian-mao Peng, and Curt A. Richter. Toward Clean and Crackless Transfer of Graphene. ACS Nano, 5(11):9144–9153, November 2011.

[53] X. S. Ling, J. E. Berger, and D. E. Prober. Nature of vortex lattice disordering at the onset of the peak effect. Phys. Rev. B, 57(6):R3249–R3252, February 1998.

[54] J. M. B. Lopes dos Santos, N. M. R. Peres, and A. H. Castro Neto. Graphene Bilayer with a Twist: Electronic Structure. Phys. Rev. Lett., 99(25), December 2007.

[55] J. M. B. Lopes dos Santos, N. M. R. Peres, and A. H. Castro Neto. Continuum model of the twisted graphene bilayer. Phys. Rev. B, 86(15), October 2012.

[56] H. Jonathon Mamin, Eric Ganz, David W. Abraham, Ruth Ellen Thomson, and John Clarke. Contamination-mediated deformation of graphite by the scanning tunneling microscope. Phys. Rev. B, 34(12):9015, 1986.

[57] T. Mashoff, M. Pratzer, V. Geringer, T. J. Echtermeyer, M. C. Lemme, M. Liebmann, and M. Morgenstern. Bistability and Oscillatory Motion

of Natural Nanomembranes Appearing within Monolayer Graphene on Silicon Dioxide. Nano Lett., 10(2):461–465, February 2010.

[58] C. Mathew Mate, Ragnar Erlandsson, Gary M. McClelland, and Shirley Chiang. Direct measurement of forces during scanning tunneling microscope imaging of graphite. Surf. Sci., 208(3):473–486, 1989.

[59] Alexander S. Mayorov, Daniel C. Elias, Ivan S. Mukhin, Sergey V. Morozov, Leonid A. Ponomarenko, Kostya S. Novoselov, A. K. Geim, and Roman V. Gorbachev. How Close Can One Approach the Dirac Point in Graphene Experimentally? Nano Lett., 12(9):4629–4634, September 2012.

[60] E. J. Mele. Commensuration and interlayer coherence in twisted bilayer graphene. Phys. Rev. B, 81(16), April 2010.

[61] José Antonio Morán Meza, Christophe Lubin, François Thoyer, and Jacques Cousty. Tip induced mechanical deformation of epitaxial graphene grown on reconstructed 6H–SiC(0001) surface during scanning tunneling and atomic force microscopy studies. Nanotechnology, 26(25):255704, June 2015.

[62] David L. Miller, Kevin D. Kubista, Gregory M. Rutter, Ming Ruan, Walt A. de Heer, Phillip N. First, and Joseph A. Stroscio. Structural analysis of multilayer graphene via atomic moiré interferometry. Phys. Rev. B, 81(12), March 2010.

[63] H. A. Mizes, Sang-il Park, and W. A. Harrison. Multiple-tip interpretation of anomalous scanning-tunneling-microscopy images of layered materials. Phys. Rev. B, 36(8):4491, 1987.

[64] David Nečas and Petr Klapetek. Gwyddion: An open-source software for SPM data analysis. Cent. Eur. J. Phys., 10(1):181–188, February 2012.

[65] V Hung Nguyen and P Dollfus. Strain-induced modulation of Dirac cones and van Hove singularities in a twisted graphene bilayer. 2D Mater., 2(3):035005, July 2015.

[66] Wataru Norimatsu and Michiko Kusunoki. Epitaxial graphene on SiC{0001}: Advances and perspectives. Phys. Chem. Chem. Phys., 16(8):3501, 2014.

[67] K. S. Novoselov. Electric Field Effect in Atomically Thin Carbon Films. Science, 306(5696):666–669, October 2004.

[68] K. S. Novoselov, D. Jiang, F. Schedin, T. J. Booth, V. V. Khotkevich, S. V. Morozov, and A. K. Geim. Two-dimensional atomic crystals. Proc. Natl. Acad. Sci. U. S. A., 102(30):10451–10453, July 2005.

[69] K. S. Novoselov, A. Mishchenko, A. Carvalho, and A. H. Castro Neto. 2D materials and van der Waals heterostructures. Science, 353(6298):aac9439, July 2016.

[70] Taisuke Ohta, Jeremy T. Robinson, Peter J. Feibelman, Aaron Bostwick, Eli Rotenberg, and Thomas E. Beechem. Evidence for Interlayer Coupling and Moiré Periodic Potentials in Twisted Bilayer Graphene. Phys. Rev. Lett., 109(18), November 2012.

[71] Martin Ondráček, Pablo Pou, Vít Rozsíval, Cesar González, Pavel Jelínek, and Rubén Pérez. Forces and Currents in Carbon Nanostructures: Are We Imaging Atoms? Phys. Rev. Lett., 106(17), April 2011.

[72] Cheol-Hwan Park, Li Yang, Young-Woo Son, Marvin L. Cohen, and Steven G. Louie. Anisotropic behaviours of massless Dirac fermions in graphene under periodic potentials. Nat. Phys., 4(3):213–217, March 2008.

[73] Hyung-Youl Park, Woo-Shik Jung, Dong-Ho Kang, Jaeho Jeon, Gwangwe Yoo, Yongkook Park, Jinhee Lee, Yun Hee Jang, Jaeho Lee, Seongjun Park, Hyun-Yong Yu, Byungha Shin, Sungjoo Lee, and Jin-Hong Park. Extremely Low Contact Resistance on Graphene through n-Type Doping and Edge Contact Design. Adv. Mater., 28(5):864–870, February 2016.

[74] Robert L. Park and Hannibal H. Madden. Annealing changes on the (100) surface of palladium and their effect on CO adsorption. Surf. Sci., 11(2):188–202, July 1968.

[75] Maria Politou, Inge Asselberghs, Iuliana Radu, Thierry Conard, Olivier Richard, Chang Seung Lee, Koen Martens, Safak Sayan, Cedric Huyghebaert, Zsolt Tokei, Stefan De Gendt, and Marc Heyns. Transition metal contacts to graphene. Appl. Phys. Lett., 107(15):153104, October 2015.

[76] Wing-Tat Pong and Colm Durkan. A review and outlook for an anomaly of scanning tunnelling microscopy (STM): Superlattices on graphite. J. Phys. Appl. Phys., 38(21):R329–R355, November 2005.

[77] L. A. Ponomarenko, R. V. Gorbachev, G. L. Yu, D. C. Elias, R. Jalil, A. A. Patel, A. Mishchenko, A. S. Mayorov, C. R. Woods, J. R. Wallbank, M. Mucha-Kruczynski, B. A. Piot, M. Potemski, I. V. Grigorieva, K. S. Novoselov, F. Guinea, V. I. Fal'ko, and A. K. Geim. Cloning of Dirac fermions in graphene superlattices. Nature, 497(7451):594–597, May 2013.

[78] Vlad S. Pribiag, Arjan J. A. Beukman, Fanming Qu, Maja C. Cassidy, Christophe Charpentier, Werner Wegscheider, and Leo P. Kouwenhoven. Edge-mode superconductivity in a two-dimensional topological insulator. Nat. Nanotechnol., 10(7):593–597, July 2015.

[79] Zhao Y. Rong and Pieter Kuiper. Electronic effects in scanning tunneling microscopy: Moiré pattern on a graphite surface. Phys. Rev. B, 48(23):17427, 1993.

[80] A. V. Rozhkov, A. O. Sboychakov, A. L. Rakhmanov, and Franco Nori. Electronic properties of graphene-based bilayer systems. Phys. Rep., 648:1–104, August 2016.

[81] G. Savini, Y.J. Dappe, S. Öberg, J.-C. Charlier, M.I. Katsnelson, and A. Fasolino. Bending modes, elastic constants and mechanical stability of graphitic systems. Carbon, 49(1):62–69, January 2011.

[82] S. Shallcross, S. Sharma, and O. Pankratov. Emergent momentum scale, localization, and van Hove singularities in the graphene twist bilayer. Phys. Rev. B, 87(24), June 2013.

[83] Christopher E. Shuck, Khachatur V. Manukyan, Sergei Rouvimov, Alexander S. Rogachev, and Alexander S. Mukasyan. Solid-flame: Experimental validation. Combust. Flame, 163:487–493, January 2016.

[84] J.M. Soler, A.M. Baro, N. Garcia, and H. Rohrer. Interatomic forces in scanning tunneling microscopy: Giant corrugations fo the graphite surface. Phys. Rev. Lett., 57(4), 1986.

[85] Dong Sun, Charles Divin, Claire Berger, Walt A. de Heer, Phillip N. First, and Theodore B. Norris. Spectroscopic Measurement of Interlayer Screening in Multilayer Epitaxial Graphene. Phys. Rev. Lett., 104(13), April 2010.

[86] J. Tersoff and D. R. Hamann. Theory of the scanning tunneling microscope. Phys. Rev. B, 31(2), 1985.

[87] J. Tersoff and N. D. Lang. Tip-dependent corrugation of graphite in scanning tunneling microscopy. Phys. Rev. Lett., 65(9):1132, 1990.

[88] Michael Tinkham. Introduction to Superconductivity. Dover books on physics. Dover Publ, Mineola, NY, 2. ed edition, 2004. OCLC: 728146785.

[89] C. Tonnoir, A. Kimouche, J. Coraux, L. Magaud, B. Delsol, B. Gilles, and C. Chapelier. Induced Superconductivity in Graphene Grown on Rhenium. Phys. Rev. Lett., 111(24), December 2013.

[90] G. Trambly de Laissardière, D. Mayou, and L. Magaud. Localization of Dirac Electrons in Rotated Graphene Bilayers. Nano Lett., 10(3):804–808, March 2010.

[91] G. Trambly de Laissardière, D. Mayou, and L. Magaud. Numerical studies of confined states in rotated bilayers of graphene. Phys. Rev. B, 86(12), September 2012.

[92] Kazuyuki Uchida, Shinnosuke Furuya, Jun-Ichi Iwata, and Atsushi Oshiyama. Atomic corrugation and electron localization due to Moiré patterns in twisted bilayer graphenes. Phys. Rev. B, 90(15), October 2014.

[93] Miguel M. Ugeda, Iván Brihuega, Fanny Hiebel, Pierre Mallet, Jean-Yves Veuillen, José M. Gómez-Rodríguez, and Félix Ynduráin. Electronic and structural characterization of divacancies in irradiated graphene. Phys. Rev. B, 85(12), March 2012.

[94] R. Vaglio, C. Attanasio, L. Maritato, and A. Ruosi. Explanation of the resistance-peak anomaly in nonhomogeneous superconductors. Phys. Rev. B, 47(22):15302–15303, June 1993.

[95] A. J. Van Bommel, J. E. Crombeen, and A. Van Tooren. LEED and Auger electron observations of the SiC(0001) surface. Surf. Sci., 48(2):463–472, March 1975.

[96] L. J. van der Pauw. A method of measuring the resistivity and Hall coefficient on lamellae of arbitrary shape. Philips Tech. Rev., 20:220–224, 1958.

[97] Léon Van Hove. The Occurrence of Singularities in the Elastic Frequency Distribution of a Crystal. Phys. Rev., 89(6):1189–1193, March 1953.

[98] P. R. Wallace. The Band Theory of Graphite. Phys. Rev., 71(9):622–634, May 1947.

[99] L. Wang, I. Meric, P. Y. Huang, Q. Gao, Y. Gao, H. Tran, T. Taniguchi, K. Watanabe, L. M. Campos, D. A. Muller, J. Guo, P. Kim, J. Hone, K. L. Shepard, and C. R. Dean. One-Dimensional Electrical Contact to a Two-Dimensional Material. Science, 342(6158):614–617, November 2013.

[100] N. R. Werthamer, E. Helfand, and P. C. Hohenberg. Temperature and Purity Dependence of the Superconducting Critical Field, ${H}_{c2}$. III. Electron Spin and Spin-Orbit Effects. Phys. Rev., 147(1):295–302, July 1966.

[101] Dillon Wong, Yang Wang, Jeil Jung, Sergio Pezzini, Ashley M. DaSilva, Hsin-Zon Tsai, Han Sae Jung, Ramin Khajeh, Youngkyou Kim, Juwon Lee, Salman Kahn, Sajjad Tollabimazraehno, Haider Rasool, Kenji Watanabe, Takashi Taniguchi, Alex Zettl, Shaffique Adam, Allan H. MacDonald, and Michael F. Crommie. Local spectroscopy of moiré-induced electronic structure in gate-tunable twisted bilayer graphene. Phys. Rev. B, 92(15), October 2015.

[102] J. Xhie, K. Satter, M. Ge, and N. Venkateswaran. Giant and supergiant lattices on graphite. Phys. Rev. B, 47(23), 1993.

[103] H. Yamada. Experimental study of forces between a tunnel tip and the graphite surface. J. Vac. Sci. Technol. Vac. Surf. Films, 6(2):293, March 1988.

[104] Yoichi Yamada, Asawin Sinsarp, Masahiro Sasaki, and Shigehiko Yamamoto. Moiré-like distribution of local tunneling barrier height of the monolayer graphite adsorbed on Pt (111) surface. Jpn. J. Appl. Phys., 41(12R):7501, 2002.

[105] Wei Yan, Wen-Yu He, Zhao-Dong Chu, Mengxi Liu, Lan Meng, Rui-Fen Dou, Yanfeng Zhang, Zhongfan Liu, Jia-Cai Nie, and Lin He. Strain and curvature induced evolution of electronic band structures in twisted graphene bilayer. Nat. Commun., 4, July 2013.

[106] Wei Yan, Lan Meng, Mengxi Liu, Jia-Bin Qiao, Zhao-Dong Chu, Rui-Fen Dou, Zhongfan Liu, Jia-Cai Nie, Donald G. Naugle, and Lin He. Angle-dependent van Hove singularities and their breakdown in twisted graphene bilayers. Phys. Rev. B, 90(11), September 2014.

[107] Matthew Yankowitz, K. Watanabe, T. Taniguchi, Pablo San-Jose, and Brian J. LeRoy. Pressure-induced commensurate stacking of graphene on boron nitride. Nat. Commun., 7:13168, October 2016.